ANALYZING SLAB HOLES IN SUBDUCTION ZONES AND THEIR IMPACTS THROUGH NUMERICAL SIMULATIONS

Taylor M. Arrowood
University of Kentucky, taylorarrowood1@gmail.com
Author ORCID Identifier:
https://orcid.org/0000-0003-2115-0203
Digital Object Identifier: https://doi.org/10.13023/etd.2021.236

Right click to open a feedback form in a new tab to let us know how this document benefits you.

STUDENT AGREEMENT:

I represent that my thesis or dissertation and abstract are my original work. Proper attribution has been given to all outside sources. I understand that I am solely responsible for obtaining any needed copyright permissions. I have obtained needed written permission statement(s) from the owner(s) of each third-party copyrighted matter to be included in my work, allowing electronic distribution (if such use is not permitted by the fair use doctrine) which will be submitted to UKnowledge as Additional File.

I hereby grant to The University of Kentucky and its agents the irrevocable, non-exclusive, and royalty-free license to archive and make accessible my work in whole or in part in all forms of media, now or hereafter known. I agree that the document mentioned above may be made available immediately for worldwide access unless an embargo applies.

I retain all other ownership rights to the copyright of my work. I also retain the right to use in future works (such as articles or books) all or part of my work. I understand that I am free to register the copyright to my work.

REVIEW, APPROVAL AND ACCEPTANCE

The document mentioned above has been reviewed and accepted by the student's advisor, on behalf of the advisory committee, and by the Director of Graduate Studies (DGS), on behalf of the program; we verify that this is the final, approved version of the student's thesis including all changes required by the advisory committee. The undersigned agree to abide by the statements above.

<div align="right">

Taylor M. Arrowood, Student

Dr. Keely Anne O'Farrell, Major Professor

Dr. Michael M. McGlue, Director of Graduate Studies

</div>

ANALYZING SLAB HOLES IN SUBDUCTION ZONES AND THEIR IMPACTS
THROUGH NUMERICAL SIMULATIONS

_____

THESIS
_____

A thesis submitted in partial fulfillment of the
requirements for the degree of Master of Science in the
College of Arts and Sciences
at the University of Kentucky

By

Taylor Murphy Arrowood

Lexington, Kentucky

Director: Dr. Keely Anne O'Farrell, Professor of Geophysics and Geodynamics

Lexington, Kentucky

2021

ABSTRACT OF THESIS

ANALYZING SLAB HOLES IN SUBDUCTION ZONES AND THEIR IMPACTS
THROUGH NUMERICAL SIMULATIONS

Subduction zones form as higher density oceanic lithosphere is forced beneath an over-riding, lower density, continental or oceanic plate; a process driven by contrasts in buoyancy throughout this system. We seek to explore subduction zones in which the subducting lithosphere is discontinuous after passing through the trench, forming a slab gap. The main research objective is to determine the effect of slab gaps on surface topography in a subduction-related orogen and asthenospheric flow into the mantle wedge using two and three-dimensional numerical mechanical models. We obtain results from 24+ models that suggest a connection between slab gaps/holes and the magnitude and trend of topography produced during the first several million years of subduction. Two-dimensional models suggest there may be flow into slab gaps and tears, affecting mantle flow around the slab and producing less topography in the orogen. Three-dimensional models suggest the opposite is true, with larger slab gaps/holes producing less surface topography above the gap. The three-dimensional models also suggest that subduction-related orogens may have associated curvature above regions where slab gaps are present. This work shows new ways to test for the potential slab gaps/holes in subduction zones by looking at flow fields, surface topography, and orogenic/slab curvature.

KEYWORDS: Subduction, geodynamics, Underworld, modeling, topography

Taylor Murphy Arrowood
(Name of Student)

06/21/2021
Date

ANALYZING SLAB HOLES IN SUBDUCTION ZONES AND THEIR IMPACTS
THROUGH NUMERICAL SIMULATIONS

By

Taylor Murphy Arrowood

Dr. Keely Anne O'Farrell
Director of Thesis

Dr. Michael McGlue
Director of Graduate Studies

06/21/2021
Date

DEDICATION

To all my friends and family: thank you for your persistent support, encouragement, and investment in me and my future.

ACKNOWLEDGMENTS

TABLE OF CONTENTS

LIST OF TABLES

LIST OF FIGURES

CHAPTER 1. INTRODUCTION

Our understanding of subduction dynamics continues to grow/change given that the theory of plate tectonics was not well developed or accepted until the second half of the twentieth century (Wilson, 1965). The exact mechanisms at play in subduction zones are dynamic, yet crucial to plate tectonics, and therefore these regions need to be understood in more detail (Billen, 2008). Lithospheric scale systems such as subduction and the associated phenomena are imaged and characterized primarily using seismic tomography data because this is a method that is capable of deep-Earth visualization (Amaru, 2007). From the seismic arrays we acquire tomograms that show subsurface seismic velocities across a transect, and these transects have been used to create several global tomography models displaying subsurface seismic wave velocity changes on a lithospheric scale (Amaru, 2007; Trampert, 1998).

There are many different anomalies visualized in seismic tomography in subduction zones, but those present at certain depths where slabs are expected to be continuous are interpreted as slab gaps, holes, or tears (Hu and Liu, 2016) (Figure 1.1). According to varying interpretations of seismic tomography data, tearing of subducting lithosphere may occur in a variety of ways, but originate from a zone of weakness and subsequently propagate along neighboring weak regions in the slab (Nolet, 2009). The anomalies are characterized by a dipping fast velocity structure identified as the subducting slab, where the dipping velocity structure becomes discontinuous, and as a result large slow velocity anomalies are present in the area of discontinuity (Stern, 2002). These anomalies vary in size for any given subduction zone where tomography data has been gathered, where smaller gaps may appear as a slightly faster velocity anomaly,
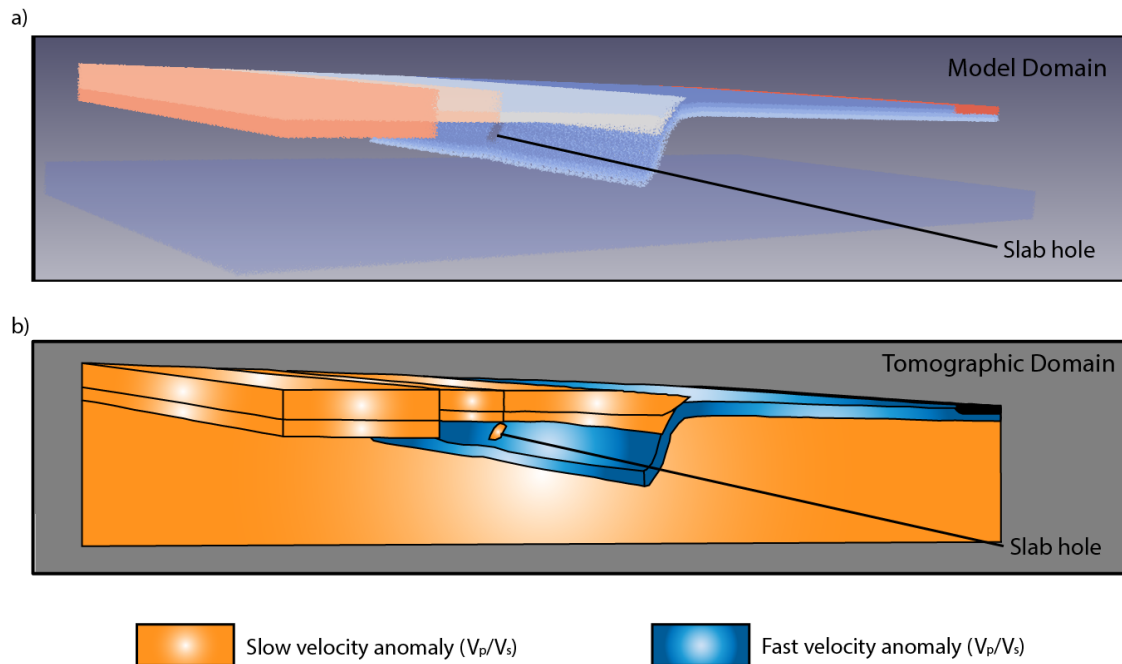
Figure 1.1 A schematic figure that displays a) what a three-dimensional subduction model looks like in *Paraview* software generated from *Underworld* 2 code that has opacity turned on to visualize the internal model geometry and b) what the anticipated seismic tomography image would show in a nearly homogenous mantle, continent, and block of oceanic lithosphere. The black portion in the back of the tomographic domain represents buoyant material not investigated in the model runs. Orange color represents an area that would typically show up as a slow velocity anomaly (P-wave or S-wave) in seismic tomography data. Blue color represents an area that would typically show up as a fast velocity anomaly in seismic tomography data.

larger gaps and holes suggest that the material with a higher seismic velocity beneath the slab is intruding such gaps (Hu and Liu, 2016) (Figure 1.2).

Some studies suggest that asthenospheric material can flow through these slab gaps, whether simply just mantle material or a broad mixture of chemically distinct melts (Pearce et al., 1990; Portner et al., 2017). It is suggested, for instance in South America, that if there is a nearby plume source, the material may be entrained along the base of the subducting plate until it reaches a slab gap, where this compositionally unique material can intrude through the slab gap and into the mantle wedge (Portner et al., 2017).

When discussing lithospheric tearing, it is also important to note the influence the lithospheric tear or gap could have near the surface, an idea that is explored in more detail in Section 2 which addresses individual case studies. Many slab holes discussed globally are both different in the unique volcanism they can produce, but also in their individual geometries (Thorkelson, 1996). Because of this, surface geology can be heavily influenced in small regions near locations directly or almost directly above slab holes (Gutscher et al., 2000). Anytime there is an influence on surface geology, this means that there is generally a resulting effect on geologic hazards. When subduction is occurring without a slab gap, geologically frequent large magnitude earthquakes occur along the subducting slab. This is apt to change with the introduction of a slab hole because of the lack of brittle deformation that can occur in the intruding asthenosphere (Hu and Liu, 2016). Analyses of focal mechanisms of individual earthquakes in a region allow viewing of the compressional (P-axes) and tensional (T-axes). When earthquakes do occur in regions where a slab gap is proposed, it is typically along the boundaries of the holes, and the orientation of the T-axis in these cases differ from the orientations of

3
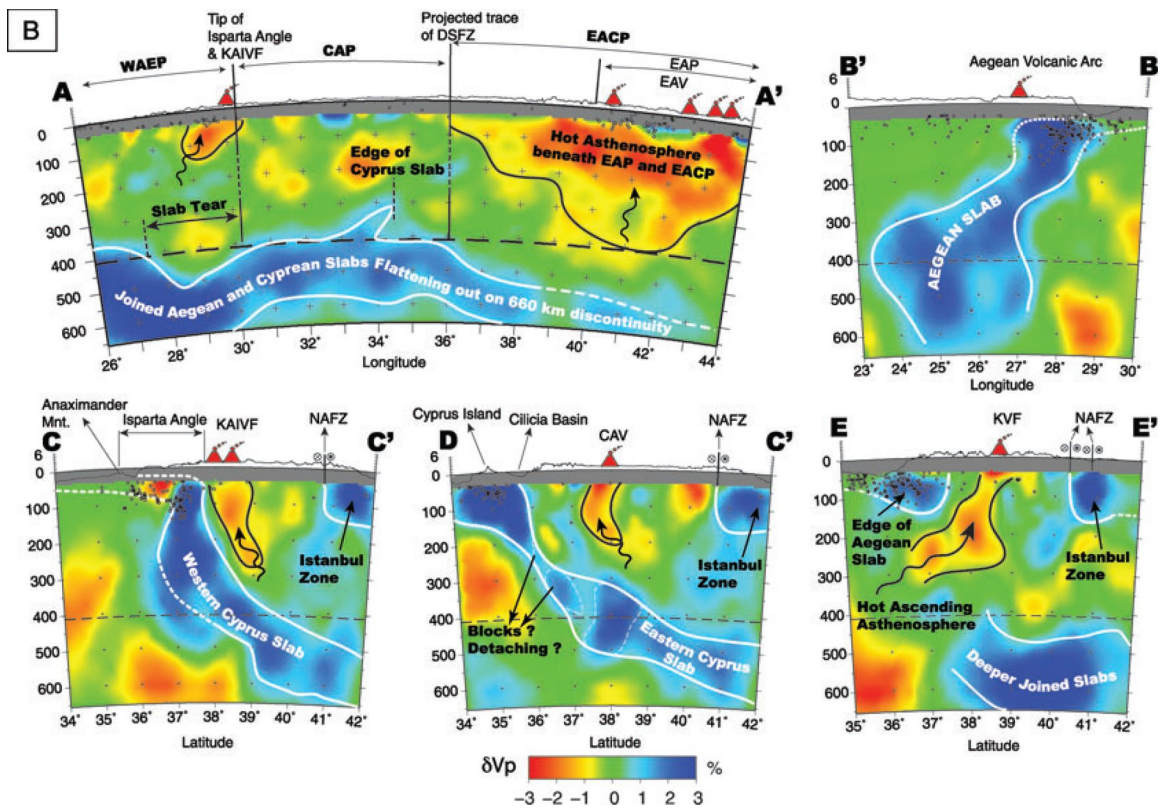
Figure 1.2 Seismic tomography results and associated interpretations that display a slab hole with hot, intruding asthenospheric material entering the mantle wedge of the subduction system, especially in cross-section E-E', located in the Anatolian Plateau (Figure 9B from Berk Biryol et al., 2011).

the T-axes of earthquakes occurring away from slab holes (Anderson et al., 2007; Hu and Liu, 2016). The primary difference between the T-axes near slab holes is that the vertical tensional component tends to be significantly greater than the horizontal tensional component (Hu and Liu, 2016).

The formation of lithospheric gaps, holes, or tears is not a process that is well understood and is not something that will be addressed in this study. Without an agreed upon mechanism for creating the slab gap/hole/tear, it would be difficult to create models where slab gaps are formed during subduction. In this thesis, two-dimensional (2D) and three-dimensional (3D) numerical models are run to investigate the effect of slab tears and holes after formation. The size and location of the slab tears and holes are varied to investigate the influence slab holes have on the magnitude (2D) and trend (3D) of topography generated at the surface, and comparisons of the flow velocities and their magnitudes into the mantle wedge through a lithospheric tear.

This thesis proceeds as follows: Chapter 2 describes the case studies used to motivate the study of slab holes, including evidence for their existence and physical properties that might be observed in the presence of slab holes and/or tears. Chapter 3 describes the numerical models used in the study and the methodology used to investigate and analyze different properties of these models. Chapter 4 discusses the results from the 2D and 3D numerical studies. Chapter 5 discusses the implication and importance of the results and Chapter 6 summarizes the main conclusions from the research studies.

CHAPTER 2. CASE STUDIES

2.1   Case Study I: Nazca-South America

One of the most prominent subduction zones today is located along the western

coast of South America, and involves the collision and subsequent subduction of the

Nazca plate beneath the South American plate to the east (Barazangi and Isacks, 1976).

Several studies suggest this subduction zone has experienced, and may to some degree

still be experiencing, flat slab subduction (Manea et al., 2012; Ramos and Folguera,

2009). Flat slab subduction involves a subducting slabs bending towards the surface upon

subduction and travel nearly horizontally for some distance before the slab continues to

move vertically again, meaning the angles of subduction in these regions are small

(English et al., 2003). One proposed attributing factor to the formation of flat slab

subduction is when the mantle wedge is closed over time by trenchward motion of thicker

cratons (Manea et al., 2012).

In addition to the proposition of flat slab subduction at the Nazca-South America

plate boundary, evidence shows the potential for the existence of a lithospheric gap (or

multiple gaps) at various depths beneath central Chile and Peru (Hu and Liu, 2016)

(Figure 2.1). The most prominent gap in Chile is estimated to be about 200 km in

diameter located at approximately 300 km depth (Lynner et al., 2017). The gap was

identified in shear wave splitting analysis as well as seismic tomography coverage of the

region (Lynner et al., 2017). The seismic tomography coverage of the region shows fast

seismic velocity anomalies overlaying slow velocity anomalies at depth, an abnormality

consistent with a gap in subducting lithosphere (Hu and Liu, 2016) (Figure 2.1, a-c). In

addition to this, the seismicity in the region and the associated stress orientations could

6
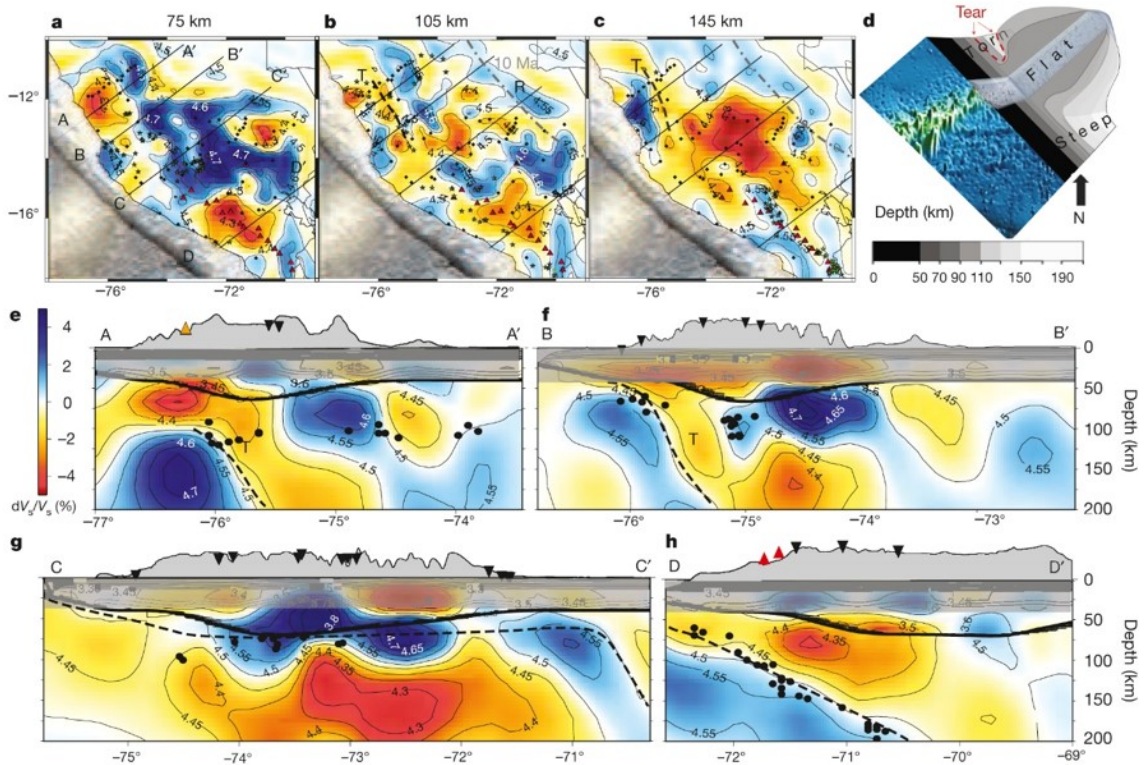
Figure 2.1 Surface-wave tomography models of the subducting slab at the Nazca-South America plate boundary. These models show the fast and slow surface wave anomalies located at various locations in the flat slab of Peru. Various tomographic images capture a) horizontal depth slice of seismic tomography at 75 km, b) horizontal depth slice of seismic tomography at 105 km, c) horizontal depth slice of seismic tomography at 145 km, d) map view orientation of depth slices, e-h) cross sections of seismic tomography data across A-A', B-B',C-C', and D-D', respectively. (Figure 2 from Antonijevic et al., 2015)

suggest the potential of a slab hole (Hu and Liu, 2016). There are large gaps in seismicity at the aforementioned locations, and the orientations of stress from earthquakes bordering the seismicity gaps agree with this interpretation (Hu and Liu, 2016). A seismicity gap is consistent with missing lithosphere since it is expected that lithosphere would behave in a brittle fashion, thus producing earthquakes when a rupture occurs. If there are no earthquakes present, it is reasonable to assume that lithosphere is no longer present in the area in question, and another material that does not deform in a brittle fashion is intruding. Finally, the presence of adakites at the surface near the proposed gap indicates an unusually hot subduction zone, which could further imply the melting of the basaltic crust by some intruding material (Hu and Liu, 2016).

2.2   Case Study II: Anatolian Plateau

The East Anatolian Plateau, which formed during the collision of Arabia with Eurasia, is another proposed location for a slab gap (Berk Biryol et al., 2011). The Bitlis-Zagros Suture Zone preserves the Miocene closure of the Neo-Tethis ocean in the Eastern Anatolian Plateau (Şengör and Yilmaz, 1981). The crust of the plateau is primarily experiencing shortening today, and is mostly accounted for within the northeast- and southeast-striking conjugate strike-slip fault systems within the plateau (Şengör and Yilmaz, 1981). Even though the crust in the Anatolian Plateau is experiencing shortening, isostasy estimates indicate that the region is isostatically undercompensated (Zor et al., 2003). From seismic velocity data in the region, it is apparent that mantle lithosphere must be missing in this region because the uppermost mantle is seismically slow (Delph et al., 2015) (Figure 2.2). These slow velocities extend throughout much of the upper
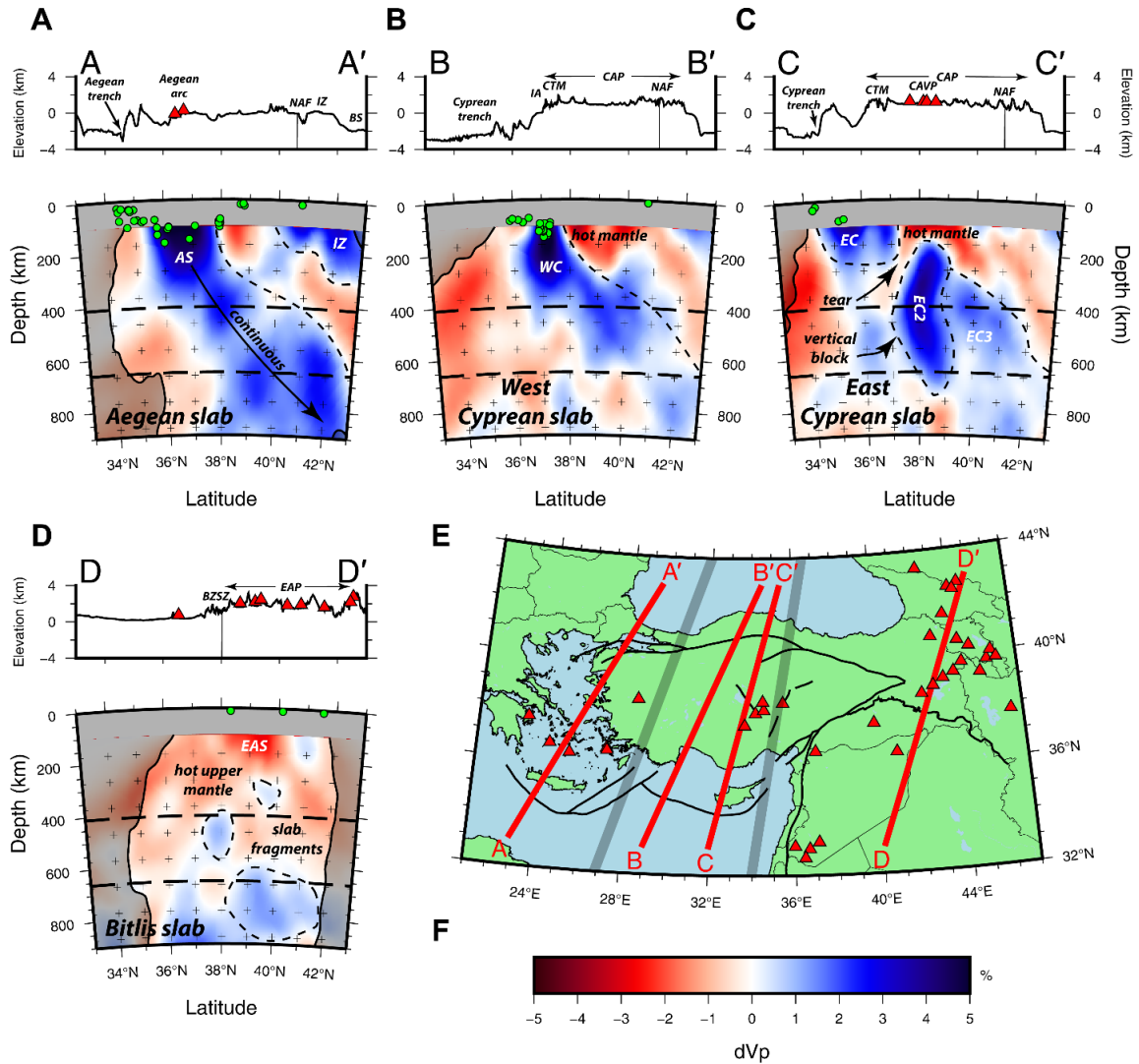
Figure 2.2 Example of seismic tomography transects taken in the Anatolian Plateau where slab holes are interpreted due to hot, intruding asthenosphere. A) shows a transect of A-A' and the associated seismic tomography found on the map in E, B) shows a transect of B-B' and the associated seismic tomography shown on the map in E, C) shows a transect across C-C' and the associated seismic tomography found on the map in E, D) shows a transect across D-D' and associated seismic tomography found on the map in E, E) shows the locations of all transects taken in the Anatolian Plateau, F) shows the scale bar of P-wave velocities used in A-D. (Figure 7 from Portner et al., 2018)

9

mantle and there is little evidence that shows any subducted Neo-Tethyan lithosphere above the MTZ (Mantle Transition Zone) (Berk Biryol et al., 2011).

In addition to anomalous seismic velocity in the uppermost mantle and mantle lithosphere, the plateau also consists of a large amount of volcanism both spatially and throughout time (Pearce et al., 1990). The majority of this volcanism occurred after the plateau experienced uplift (~12 Ma) until recently (Pearce et al., 1990). Because volcanism proceeded from north-to-south across the Anatolian Plateau from 11 Ma until present day, and the youngest volcano shows the least substantial signature geochemically, which indicates a great possibility that plateau uplift coincided with the steepening of the subducting slab, followed by the detachment of the slab (Keskin, 2003; Pearce et al., 1990). These findings, in conjunction with the seismic tomography data suggest that a lithospheric gap is present in this region because these anomalies suggest that hot, upwelling asthenosphere is intruding into the mantle wedge through the slab gap, which would produce the recent volcanism and can explain the high elevations in the plateau (Berk Biryol et al., 2011; Delph et al., 2015; Keskin, 2003; Portner et al., 2018; Şengör and Yilmaz, 1981). The proposed slab gap beneath Anatolia is approximately 200 kilometers in cross-sectional width, and consists of a more fragmented slab where the largest discontinuities begin around 200 kilometers depth and continue to just over 400 kilometers depth (Király et al., 2020).

2.3   Case Study III: Italian Apennines

The Italian peninsula is approximately 200 km wide on average and consists of the Apennine mountain range and the Calabrian arc. The Apennines-Calabrian chain has

been extensively studied due to the geological complexity that could pose some challenges to our current understanding of plate tectonics, and has been foundational in improving the theory over the years (Faccenna et al., 2014a). Some of these geological complexities include variable topography, uplift, crustal thickness, and seismicity across the Apennines-Calabrian chain (Faccenna et al., 2014b). The central Apennines consists of the thinnest crust (30-40 km), the highest relief (nearly 3 km), the highest mean elevation, and the shallowest seismicity in the Apennines-Calabrian chain (Faccenna et al., 2014b). In terms of seismicity in the region, in the Calabrian arc (southern Italy) the Wadati-Benioff zone extends as deep as approximately 400 km, whereas in the northern Apennines the vast majority of seismic events recorded are between 100 and 150 km depth, and in the central Apennines the deepest seismicity is only at approximately 100 km depth (Faccenna et al., 2014b). There is a complete lack of seismicity in the central Apennines beneath ~100 km, thus there are no intermediate or deep earthquake events sourced there (Faccenna et al., 2014b).

A slow seismic velocity anomaly has been observed using P-wave seismic tomography data in the central Apennines (continuing south) that extends from the surface to depths of approximately 400 km (Amaru, 2007; Piromallo and Morelli, 2003) (Figure 2.3). This seismic velocity anomaly has been interpreted to be a lithospheric gap, and there is additional evidence from calculations of dynamic topography in the region that supports missing lithosphere, causing the area to be undercompensated isostatically (Faccenna et al., 2014b). Further evidence to support the slab gap interpretation includes observed seismic anisotropy in the central Apennines that likely indicates mantle flow in the central region is not oriented parallel to the subduction arc, as is typical, but rather is
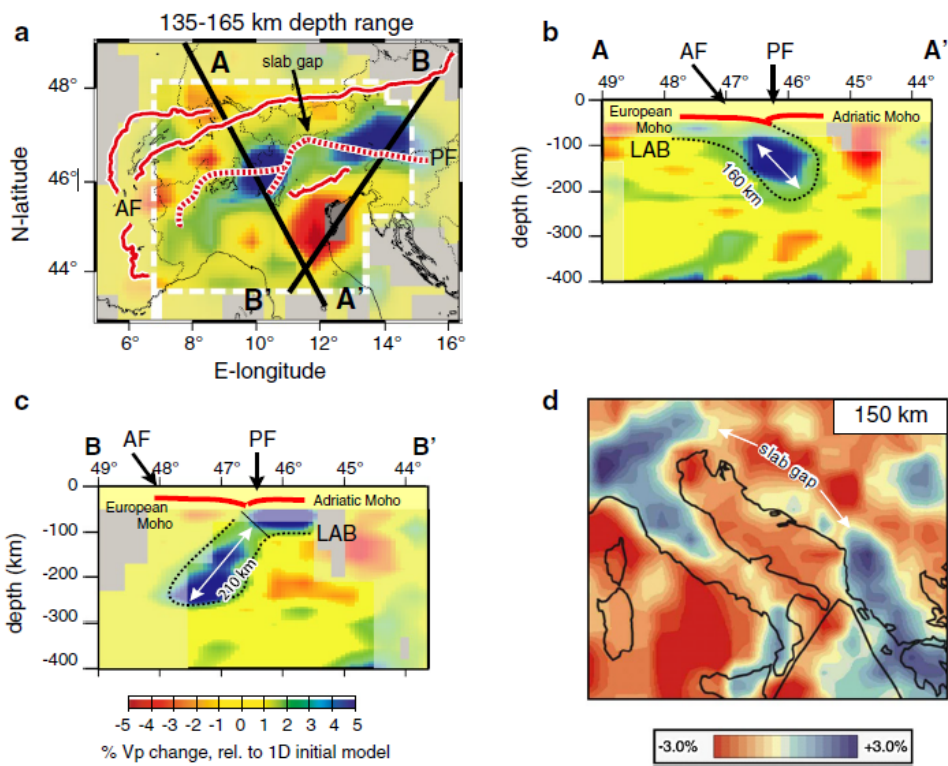
Figure 2.3 Modelled seismic tomography results in the Mediterranean that display possible evidence for slab gaps that could have played a major role in formation of the Alps-Carpathians-Dinarides. a) Shows the modelled tomography data from map view of the Mediterranean, b) shows the cross section from A-A' from a where a slab is descending, c) shows the cross section from B-B' from a, where a slab is descending beneath the Alps, and d) shows map view of seismic tomography at a depth of 150 kilometers and illustrates a slab gap from discontinuous fast P-wave anomalies. (Figure 4 from Handy et al., 2015).

oriented perpendicular to the subduction zone (Faccenna et al., 2014a). The dimensionality of the proposed slab gap beneath the Mediterranean is approximately 200 kilometers in cross-sectional width and occurs between depths of 200 kilometers and 350-400 kilometers, depending on location (Király et al., 2020).

2.4   Case Study IV: East Java

The island of East Java consists of two blocks of oceanic crust converging, the Indian plate, and the Eurasian plate. The Indian plate is subducting beneath the Eurasian plate, a process that has been ongoing for approximately 45 Myrs (Hall, 2012). Despite consistent subduction during this time, the associated volcanism has not been constant since 45 Ma (Smyth et al., 2008). Primarily expressed in the Southern Mountains Arc, volcanism became dormant between 45 Ma and 20 Ma, when the rock record indicates particularly acidic volcanism in the region (Smyth et al., 2008).

In addition to discontinuous volcanism, there is an evident seismicity gap in the Wadati-Benioff zone (Hall and Spakman, 2015). The gap in the Wadati-Benioff zone coincides with a gap in the subducting lithosphere anomaly visualized in seismic tomography maps in the region between 250 and 500 km depth (Widiyantoro et al., 2011) (Figure 2.4). It is proposed that the slab gap initially formed from buoyant material passing through the trench of the subduction zone, where this material could not continue subducting with the slab, and thus the buoyant material detached from the slab leaving a lithospheric gap in its place (Hall and Spakman, 2015). The subducting slab, along with the lithospheric gap, continued to subduct, and as the gap progressed downward, the potassic alkaline volcanism followed the gap location until subduction of the gap
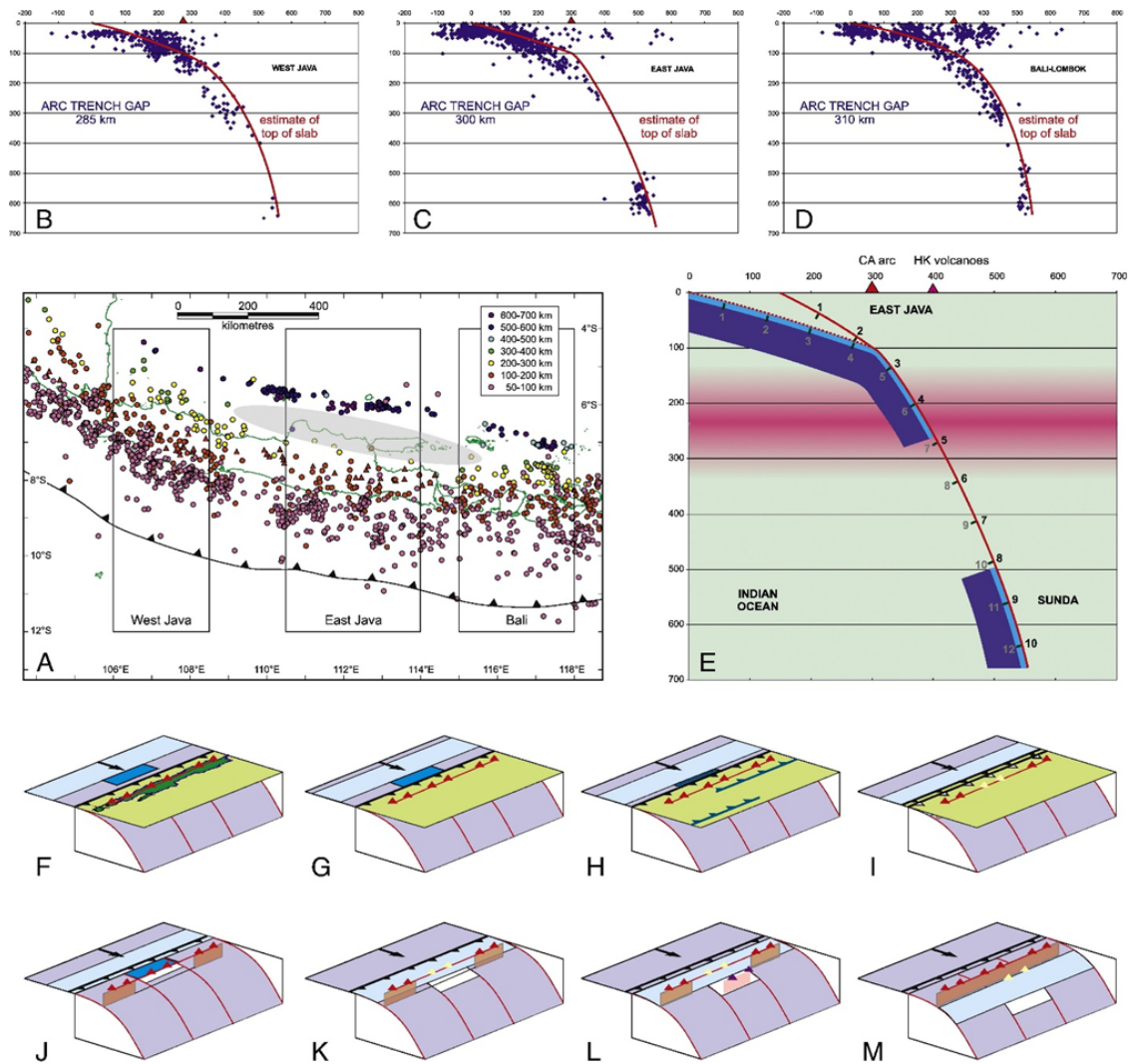
Figure 2.4 Annotated seismicity data from east Java that may be evidence for a lithospheric gap in the region, where A displays a regional map of all relevant seismicity data in the region of interest in east Java, B-D show seismicity data as blue dots at depth in west Java, east Java, and Bali with the estimated location of the slab projected in red. E shows the projection of the slab and associated gap at depth based on seismicity data as a method of projecting the age of the slab to describe the volcanic signatures present in the region (red triangles on x-axis). F-I show an example of congested subduction as a feature attempts to pass through the trench. J-M show interpretations of the removal of the upper plate and formation of a slab gap. (Figure 5 from Hall and Spakman, 2015)

progressed enough for the unique volcanism to end (Hall and Spakman, 2015). The

Wadati-Benioff zone gap remains visible in seismicity data however, as brittle

deformation could not occur in a region of missing lithosphere (Hall and Spakman,

2015). The proposed slab gap in East Java extends from about 150 kilometers in depth to

nearly 400 kilometers depth, and consists of about 150 kilometers of cross-sectional

width of the slab missing (Király et al., 2020).

CHAPTER 3. METHODS

3.1   Methods Overview

The following section outlines the methodology behind model creation, theory, various software used, and specific models ran that are discussed within the thesis document. Additionally, insight into how calculations and approximations were performed to produce the results presented in section 4 and discussed in section 5. The outline is broken into two sub-sections: 1) Two-dimensional methods describing the model setup, coding package(s) used, computational requirements, and visualization of the model post-run and 2) Three-dimensional methods describing the same procedures but with an added width dimension to the model geometry.

3.2   Two-dimensional Mechanical Models.

3.2.1   Background, theory, and model design

In *Underworld*, we can model subduction and plate motion in a two-dimensional cartesian box where we assume buoyancy forces are present on any material layer added into the box (Schellart and Moresi, 2013). These buoyant forces naturally arise from a mantle material layer that is specified as an incompressible fluid in which lithospheric layers sit atop (Schellart and Moresi, 2013). To make the necessary calculations that involve these physical properties, *Underworld* solves the following three equations (Schellart and Moresi, 2013):

A non-dimensional equation of motion:

$$-\nabla \cdot \tau + \nabla p = \Delta \rho g \hat{z} \tag{1}$$

An incompressibility relationship:

$$\nabla \cdot u = 0 \tag{2}$$

A deviatoric stress tensor equation:

$$\tau_{ij} = \eta \left(\frac{\partial u_i}{\partial x_j} + \frac{\partial u_j}{\partial x_i} \right) \tag{3}$$

where τ represents the deviatoric stress tensor, p is the dynamic pressure, ρ is the density

of the material, g is the gravitational acceleration, $\hat{z}$ is the unit vector defined in the

model that points downward, u represents the velocity, and η represents the dynamic

viscosity.

Models in Underworld can be designed with a number of features including model

scaling, addition of objects or materials to the model domain, as well as adding material

properties to each model object/material. Model parameter values used in this study for all

associated materials are provided in detail in Figure 3.1 and Table 3.1.

We begin by addressing the desired scale of the model for modeling a subduction

zone with the purpose of analyzing a near-surface response to potential intrusion of

mantle material through the mantle wedge that arrives in this region due to a lithospheric

gap. The model domain across all two-dimensional models is 4000 km long, from the

beginning of the continental material at the left wall to the extent of the subducting slab at

the right wall. This width is ideal for a subduction model to give enough material to

subduct through the trench for necessary data acquisition, without the tail end of the slab

influencing model results. The depth of the model is 1000 km, sufficient to visualize

mechanical convection processes within velocity data, and to observe the ambient mantle

Table 3.1 Model parameters for two-dimensional subduction models.

Parameter	Symbol	Value	Units
Model Geometry			
Air/sticky air thickness	h_a	12.5	km
Continental crust thickness	h_{cc}	35	km
Oceanic Slab thickness	h_{oc}	100	km
Mantle Transition Zone Depth	d_{MTZ}	660	km
Oceanic Slab length	ℓ	3100	km
Material Properties			
Density of air layers	ρ_a	1	kg/m^3
Density of upper mantle	ρ_{um}	3300	kg/m^3
Density of lower mantle	ρ_{lm}	4000	kg/m^3
Density of continental crust	ρ_{cc}	2650	kg/m^3
Density of mantle lithosphere	ρ_{ml}	3380	kg/m^3
Viscosity of Air	η_a	1.0×10^{18}	Pa s
Viscosity of sticky air	η_{sa}	1.0×10^{19}	Pa s
Viscosity of upper mantle	η_{um}	1.4×10^{19}	Pa s
Viscosity of lower mantle	η_{lm}	1.4×10^{20}	Pa s
Viscosity of continental crust	η_{cc}	1.0×10^{23}	Pa s
Viscosity of continental ML	η_{cml}	1.0×10^{22}	Pa s
Viscosity of upper oceanic ML	η_{ouml}	1.4×10^{22}	Pa s
Viscosity of core oceanic ML	η_{ocml}	7.0×10^{21}	Pa s
Viscosity of lower oceanic ML	η_{olml}	2.8×10^{21}	Pa s
Continental cohesion	c_c	48	MPa
Cohesion of upper oceanic ML	c_{ouml}	48	MPa
Cohesion of core oceanic ML	c_{ocml}	200	MPa
Cohesion of lower oceanic ML	c_{olml}	48	MPa
Other Parameters			
Gravitational acceleration	g	10	m/s^2

18
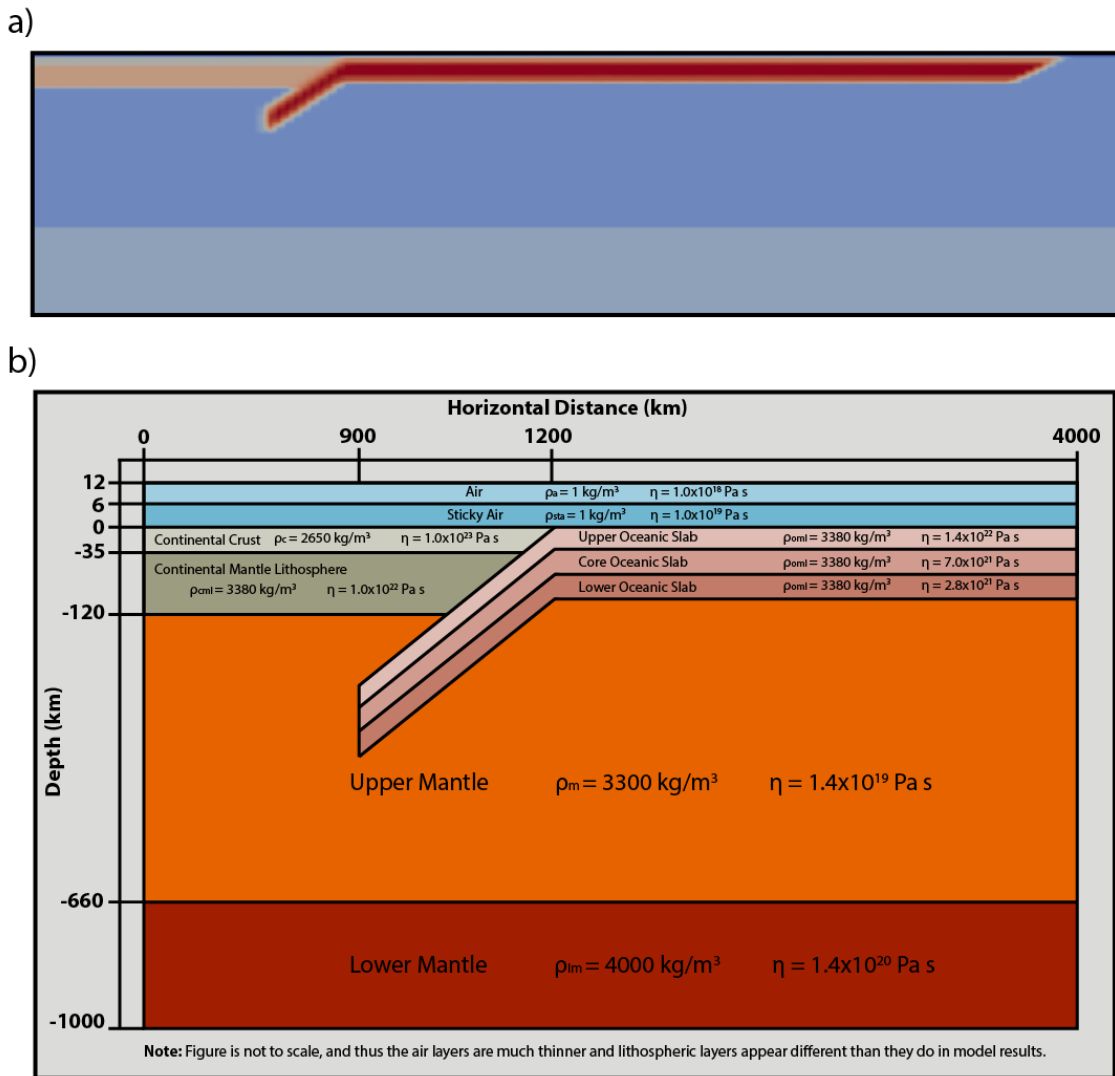
Figure 3.1 Schematic diagram of two-dimensional model setup in *Underworld 2*. A shows the model appearance in *Paraview* at the initial model timestep. B illustrates the materials used in the model domain, including material properties and model geometry. Refer to Table 1 for more model parameter information.

processes occurring that may be forcing the subduction of the slab. This extended model depth also allows the possibility of a slab subducting past the 660 km transition zone (TZ) without forcing a physical boundary at the TZ from the model domain size. We setup our model with an overriding continent on the left hand side of the model domain, a trench located at (x=1200 km), and a subducting slab on the right hand side of the model that extends almost to the end of the model domain. The slab is initially setup to be subducting at an angle of about 37 degrees about 300 km into the mantle. Figure 3.1 shows a schematic of the model setup in 2D. The details of the model materials used in this setup are described below.

Our model domain consists of 9 materials/model objects (Figure 3.1, Table 3.1). The first two materials are an air and sticky air layer, included for the purpose of monitoring the topographical changes that occur within the continental material due to subduction processes, and represent the air, sediment, and other surficial materials that may be present above the subduction zone. (Crameri et al., 2012) have shown that including a sticky air layer produces more realistic topography than in models without. The third model material is an upper mantle material which represents the Earth's mantle between the lithospheric mantle and the lower mantle boundaries. In our models, this upper mantle material extends from approximately 100 km depth to the TZ at 660 km depth (Figure 3.1). The amount of upper mantle material is slightly less beneath continental material, due to the increased thickness of the continental crust. The fourth material we introduce into the models is a lower mantle layer that begins at the depth of the TZ and extends to the bottom of the model domain (Figure 3.1). These two materials are primarily distinguished by a step increase in density and viscosity, which is

determined from the behavior of seismic waves as they penetrate the TZ (Rudolph et al., 2015).

The next materials added to the model are a continental crust and continental lithosphere. The continental crust extends to a depth of 35 km, typical of continental crust near plate boundaries (Christensen and Mooney, 1995). At the boundary between this material and the continental mantle lithosphere, there is a viscosity decrease but a density increase. The continental mantle lithosphere extends from 35 km depth to 125 km depth, where the approximate boundary between the lithosphere and asthenosphere occurs (Plomerová et al., 2002). These materials, as with the oceanic materials discussed next, are defined by coordinates in our cartesian model box. The previous materials were defined in layers that were specified to various depths. These continental materials remain to the left of the trench (x = 1200 km), as to represent the continental side of convergence. The continental materials are also attached to the left wall by a no-slip boundary condition, allowing the continental materials to stay in one location as subduction initiates and proceeds. To the right of the trench are the final two materials, the oceanic crust and oceanic mantle lithosphere. These layers extend to approximately 4000 km and approach but do not touch the model domain at the right, to maintain another no-slip condition on the right-side wall but still allow subduction to occur. The oceanic crust layer material is defined with the composition of oceanic crust in density, approximate viscosity, and anticipated brittle/ductile behavior (for specific values, see Table 3.1). The models have 10 km of oceanic crust beginning at 4000 km at the far right and continues to 210 km depth beneath the trench (Figure 3.1). Another 90 km of mantle lithosphere is included beneath the oceanic crust, characterized by a viscosity decrease,

21

but with the same density. This layer reaches a depth of 300 km at the tip of the subducting slab nose/edge (Figure 3.1).

Slab holes and tears are introduced into the subducting slab at model initiation, specified by replacing the slab material with upper mantle material at specified coordinates in the model domain (Figure 3.2). Specifying different sets of bounding coordinates allows for easily changing the geometry and location of slab tears and holes to easily compare all necessary results. Adding the slab tears was done by creating a box of coordinates, the vertices of which are specified, and any slab material present within those vertices becomes upper mantle material and no longer retains the typical properties of the slab (Figure 3.2,3.3). To increase the size of the hole, the two right vertices (if adding a top tear) of the box are moved further right or two left vertices are moved further left (if adding a bottom tear) (Figure 3.3). These features were added to the top and bottom of the slab in individual model runs to simulate all possible origins of potential weakness in subducting slabs. Slab holes/tears introduced in our models are specified to originate from the top of the slab as if to simulate the subduction of features at the trench that may cause tearing (Hu and Liu, 2016), whereas the tears/holes introduced to the bottom of the slab simulate a possible result of a plume or other process impinging on the slab. Because this is an area of ongoing research, attempting to generate a slab hole in our subduction system is not part of our overall goal but rather to examining the effects of the presence of slab holes after formation.

To monitor surface topography and flow through and around slab holes, we implement several sets of passive tracers (Figure 3.4). These tracers serve to provide information about the movement of particles in the model without affecting the behavior
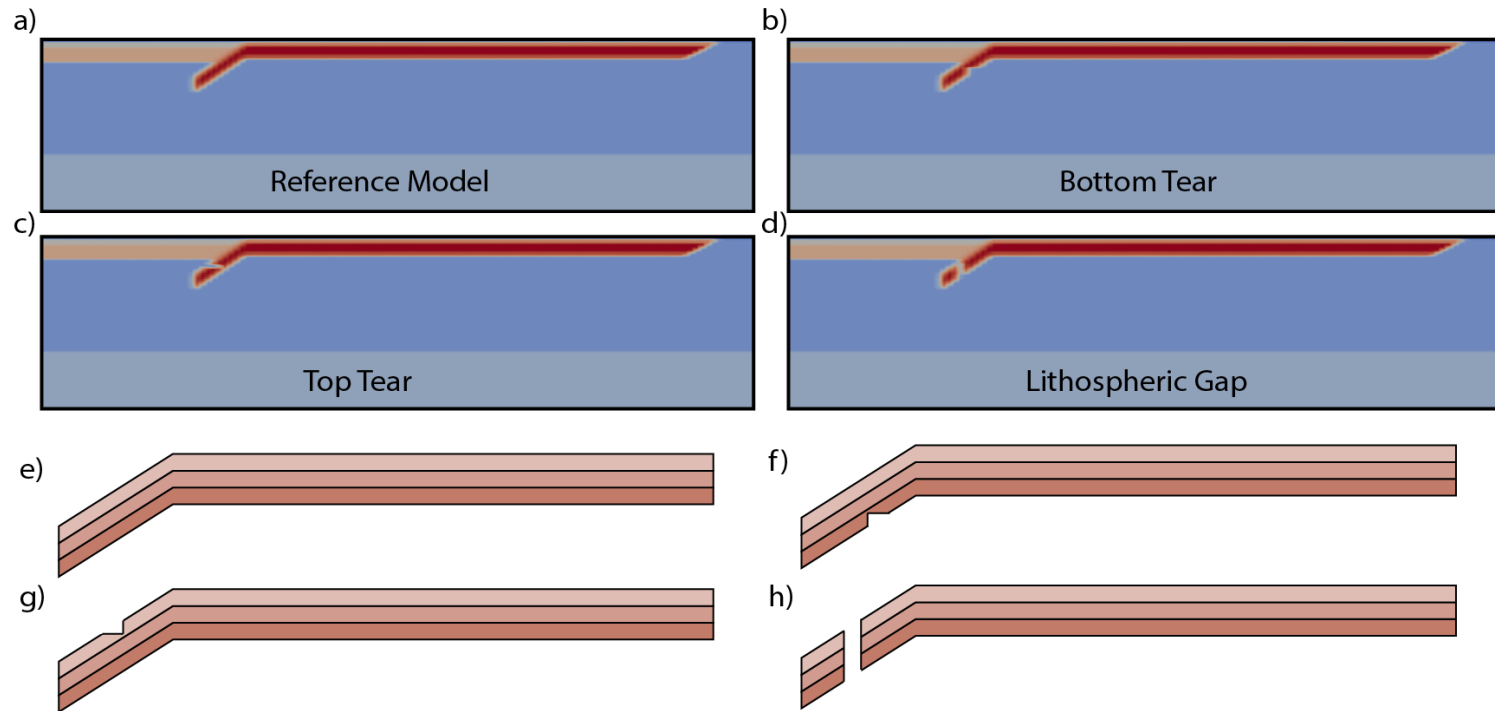
Figure 3.2 Schematic diagram of two-dimensional model setup in *Underworld 2*. A shows what a reference model would look like when loaded for visualization in *Paraview* at the initial timestep (0 Myr). B shows the same setup but for a tear that has been added at model initialization to the bottom of the subducting lithosphere within the nose of subducting lithosphere. C shows the same setup as B but for a top tear. D shows the case in two-dimensional models where a hole is added to the nose of the subducting slab, forming a complete gap in lithosphere. E-H show how these tears are cut into each slab in a schematic format.

a)

length

width

Area = 1/2(length x width)

b)

width

Length

Area = A_{rect} - $A_{triangles}$
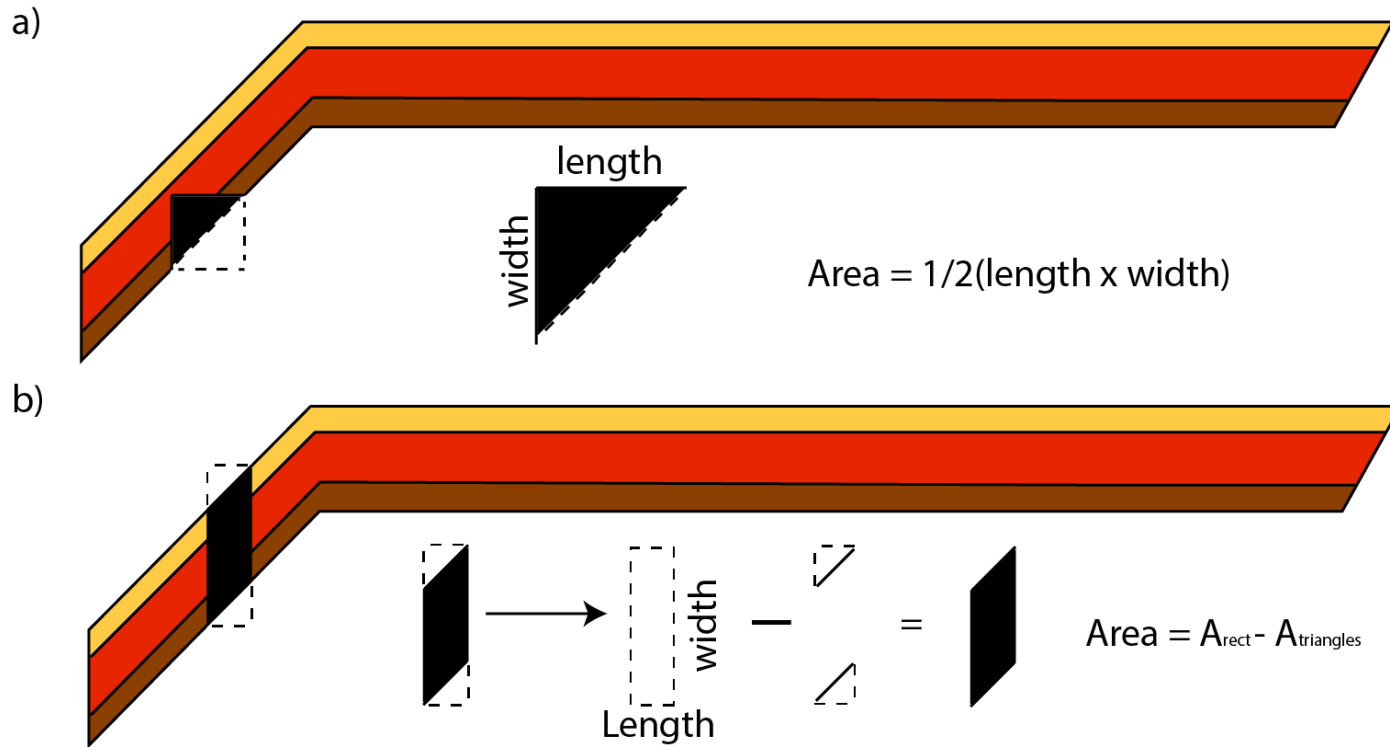
Figure 3.3 Schematic diagram of how the area of the missing lithosphere is determined in two-dimensional models. In the case of A, a slab tear, the area is simply that of a triangle that is half the area of a box used to cut the tear. In the case of B, a complete lithospheric gap, the area is determined by the assumption that a rectangle is used to cut the hole, and then remove the access rectangle area through the two triangles at either end to only obtain the area within the slab and no excess.
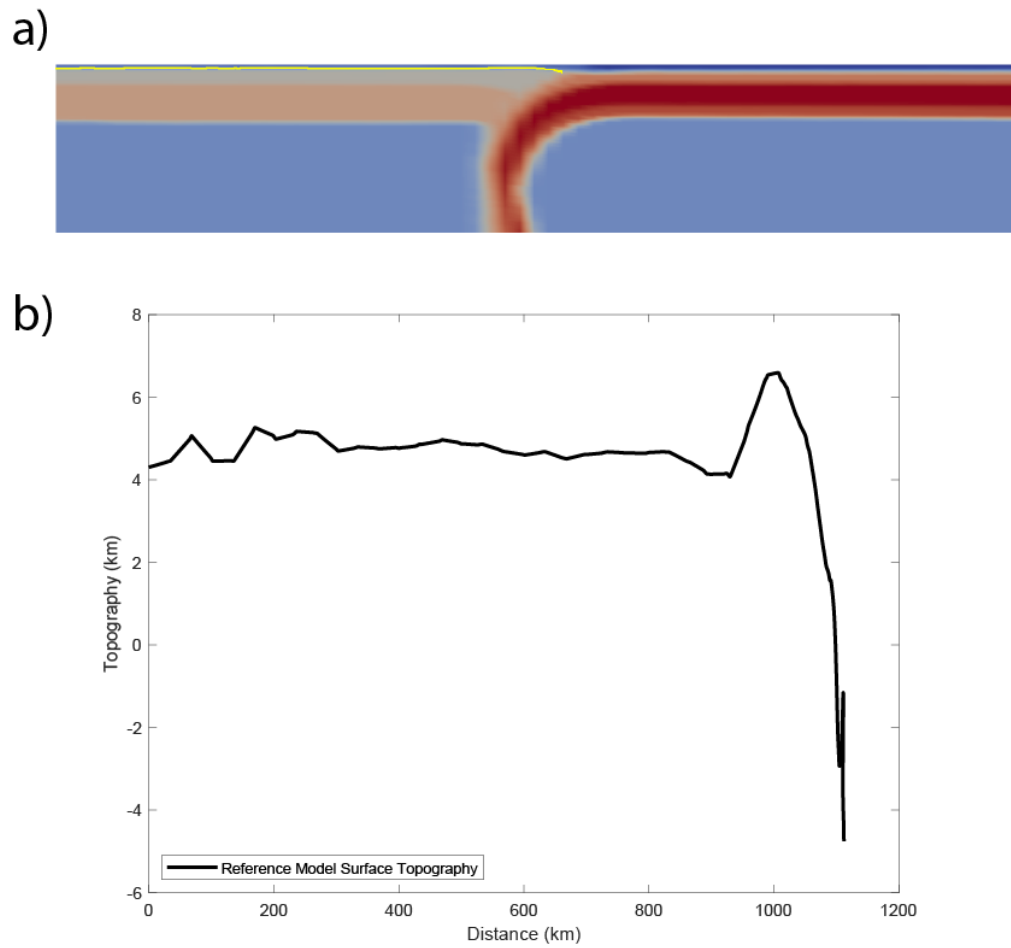
Figure 3.4 Schematic diagram of 2D surface topography methodology showing A, the tracer appearance within the model domain along the continental block. B illustrates the tracer topography of the reference model (version 47) once the data is plotted in external software such as *MATLAB*.

of the model or the model elements. The location of the passive tracers is recorded for

each timestep in the model and then visualization of the tracers can be done at any

timestep of interest. Tracers were added to the models to monitor the change in surface

topography above the subduction zones in the continental region. They were also added

above the oceanic portion of the subduction model, to which they monitor the subduction

of oceanic material into the mantle wedge, continuing into the mantle beneath the

continent. Beneath the surface, tracers were added to both the top and bottom of the slab,

such that any amount of flow passing through lithospheric gaps would be noted during

subduction, as breakoff occurs, and/or the slab hole/tear grows.

In addition to the specification of model materials and their associated properties,

boundary conditions of the models, as with any model, must be specified. In these

mechanical models, the boundary conditions utilized are a combination of free-slip and

no-slip conditions. None of the mechanical boundary conditions specified are internal but

only defined along the edges of the model domain. For mechanical models, the only

boundary conditions necessary are velocity boundary conditions. These boundary

conditions are specified by setting the value of the allowed flow velocity of particles in

each direction along the boundary interface. Along the left and right walls of the model

domain the velocity boundary condition is set to no-slip ($u_x=0$), meaning the particles are

not permitted to move in the horizontal direction at this interface. The vertical velocity

boundary condition along these walls is set to free-slip ($u_y=None$), meaning the particles

are permitted to move in any direction at any magnitude as determined by the model

solution at any given timestep. Along the top of the model domain the horizontal and

vertical boundary conditions are free-slip, while the bottom of the model domain is strictly no-slip in both horizontal and vertical directions.

Finally, once boundary conditions are defined, and model materials are created and assigned desired values, a solver must be selected for the model. The solver used in the *Underworld* code is a Stokes block system (Moresi et al., 2003):

$$\begin{bmatrix} K & G \\ G^T & C \end{bmatrix} \begin{bmatrix} u \\ p \end{bmatrix} = \begin{bmatrix} f \\ h \end{bmatrix} \tag{4}$$

Where u is …, p is …. Etc. Gaussian elimination can then be applied to the above system such that it can be re-written as (Moresi et al., 2003):

$$\begin{bmatrix} K & G \\ 0 & S \end{bmatrix} \begin{bmatrix} u \\ p \end{bmatrix} = \begin{bmatrix} f \\ \hat{h} \end{bmatrix} \tag{5}$$

where the variables used in Eqn 4 and Eqn 5 are all various components used in the velocity backsolve process to solve Eqns. 1-3 to obtain a change in model time over each timestep.

The mantle is assumed to deform over large timescales through viscous diffusion and dislocation creep (Moresi et al., 2003):

$$\eta_{eff} = \frac{1}{2} A^{\left(-\frac{1}{n}\right)} \dot{\epsilon}^{\left(\frac{1-n}{n}\right)} d^{\left(\frac{m}{n}\right)} \exp\left(\frac{E+PV}{nRT}\right) \tag{6}$$

where A is the Arrhenius prefactor, $\dot{\epsilon}$ is the square root of the second invariant of the deviatoric strain rate tensor, d is the mineral grain size, n is the stress exponent, m is the grain size exponent, E is the activation energy, P is the pressure, V is the activation volume, R is the gas constant, and T, the temperature (Moresi et al., 2003). These values

are solved for at each time step for a given viscous flow law that is assigned to each material by the user.

In addition to the solving of viscous creep flow laws that produce deformation of model materials, there are also plasticity laws added to the model materials that would deform plastically in nature. The plasticity law governing the plastic deformation of the 2D mechanical models is a Drucker-Prager solution where an effective plastic viscosity is given by:

$$\eta_{eff} = \frac{\sigma_y}{2\dot{\epsilon}} \tag{7}$$

where σ_y is the plastic yield value, η_{eff} remains to be the effective plastic viscosity of the material, and $\dot{\epsilon}$ remains to be the second invariant of the strain rate tensor, defined as (Moresi et al., 2003):

$$\dot{\epsilon} = \sqrt{\frac{1}{2}\dot{\epsilon}_{ij}\dot{\epsilon}_{ij}} \tag{8}$$

The yield value, σ_y, is defined by a Drucker-Prager yield criterion in two-dimensional models as (Moresi et al., 2003):

$$\sigma_y = C\cos\phi + \sin\phi P \tag{9}$$

where C and P are coefficients of friction, and ϕ is the friction angle of the material. In two dimensions, this follows the typical Mohr-Coulomb criterion, but if $\phi = 0$ the yield criterion is instead classified as Von Mises (Moresi et al., 2003). With a yield criterion of 0, or Von Mises yield criterion, the material has no cohesive strength assigned, whereas

Mohr-Coulomb criteria give the material some value for the cohesiveness such that the material is less prone to failure.

3.2.2 Computational resources used for model execution

Due to the computational expense of running many models simultaneously at high enough resolutions, the University of Kentucky supercomputer: Lipscomb Compute Cluster (LCC) is used to both run models over geologic time scales on a computational node, and also to visualize them in *Paraview* on a graphical node. Scripts are written using *Jupyter* notebooks and then uploaded to the LCC, where a submission script is written that specifies which node to run models on and how many processors to use for the job. Once submitted to the job queue, model results appear in an outputs folder to be visualized. All two-dimensional models are run at a resolution of 128 elements per cell in the length (x) direction and 128 elements per cell in the depth (y) direction. Thus, the total number of particles added to the swarm in two-dimensions is 16,384. This corresponds to a resolution of approximately 33 km per cell/element in the length dimension, and approximately 8 km per cell/element in the depth dimension. All models were run using 1 node and 46 processors and took approximately 12 hours to run to completion, corresponding to about 90 million years in the models.

3.2.3 Visualization and data analysis methods of 2D mechanical models

Visualization of the model results was done using the open-source software *Paraview*, a program designed to view and interact with complex model files. Model files

were loaded into *Paraview* first, followed by the tracer layers specified at model

initiation. *Paraview* software allows visualization such that the output of many different

model fields can be visualized at a given timestep. Thus, at each output interval, plots can

be visualized for the density, viscosity, velocity, pressure, strain and strain rate, and the

material field of the particles in the model domain. The files from each timestep can be

played sequentially such that it creates videos of what happens during the model in each

of the mentioned outputs. Subsequently, post-processing scripts generate plots of these

fields in coordinate space at each output interval, so that numerical values are obtained

for these fields.

Paraview was essential to gathering surface topography data because of the built-

in ruler feature that allows measurements to be made between the horizontal datum and

the height at which surface topography tracers were displaced as subduction proceeded.

Measurements of surface topography were taken in each model upon the subducting slab

arriving at the TZ (which happened at different times in each model) to avoid any

influence this collision would have on surface topography. It is from these measurements

that the topographical change at some time after model initiation can be plotted versus

horizontal distance (Figure 3.4). Plotting the tracers in a proper coordinate system allows

for visualization of the long-wavelength topography and how it changes with individual

models. The flow fields were examined near slab hole/tear zones in the subducting slab to

search for potential flow-through in a similar fashion. The plots are generated in

MATLAB based on the topography data gathered when using *Paraview*.

Surface topography data was further used to analyze the influence of the area of

missing lithosphere on maximum surface topography observed within the orogen created

in each simulation. Calculating the area of each piece of missing lithosphere is done by probing the location of the vertices of shapes where slab gaps are, and then using the shapes formed by the vertices to calculate the enclosed area. The approximate error on each measurement of area is 100 km^2. The maximum topography values for each model determined from the surface tracers are then pulled alongside this area data to test any possible correlation. Plots of maximum topography in the orogen (ignoring a datum elevation), versus the area of the missing lithosphere of the particular model are created and then tested for correlation using a least squares solution. The least squares solution is necessary when solving inverse problems and is utilized by beginning with:

$$Gm = d \tag{10}$$

where G is a data kernel matrix typically storing an array of values equal to 1, m is an array of model parameters (in this case the area of missing lithosphere), and d is the observed data points (in this case the maximum observed topography) (Menke and Menke, 2016). From this relationship, the least squares solution for the dataset is calculated by determining the predicted surface topography that would be produced by rearranging to:

$$m_{est} = (G'G)^{-1}G'd \tag{11}$$

Where m_{est} now becomes the new estimated model parameters (Menke and Menke, 2016). Finally, the data predicted by the estimated model parameters, d_{est}, can then be determined by:

$$d_{est} = Gm_{est} \tag{12}$$

The correlation between d and d_{est} is done to quantify fit of each dataset to a predicted amount of surface topography and test the expected trends. This was done separately for the bottom and top tears, and then all data with the respective least squares solutions together. To further quantify the degree of accuracy of the least squares solution, the R^2 values were obtained for each solution using the following relationship:

$$R^2 = 1 - \frac{SSE}{SST} \tag{13}$$

Where SSE is the sum of squared error, and SST is the sum of squared total. These calculations and analyses were not performed for flat slab cases due to a lack of data points necessary for correlation.

Paraview is also used to examine vertical profiles of the velocity field, in combination with vertical profiles of the material field of models used, taken from versions with and without missing lithosphere (Figure 3.5). All these profiles are taken at approximately the same horizontal distance, and all profiles are extracted at the same model time (non-dimensional model time =0.2 Myrs, or 3.0 Myrs equivalent real-world time). Scaling of model time and velocity are discussed further below. This was done by picking two points in a model domain and plotting the velocity field over the line connecting the two points (Figure 3.5). The vertical profiles can then be aligned side-by-side to compare both fields simultaneously at corresponding depths. When taken together, the plots generate the ability to see which model materials are present at a location, and what the velocity of model particles is at the given model depth. The velocity can be viewed in separate components for each direction, though we only utilize the horizontal direction, as this is the direction that would be most beneficial to visualize
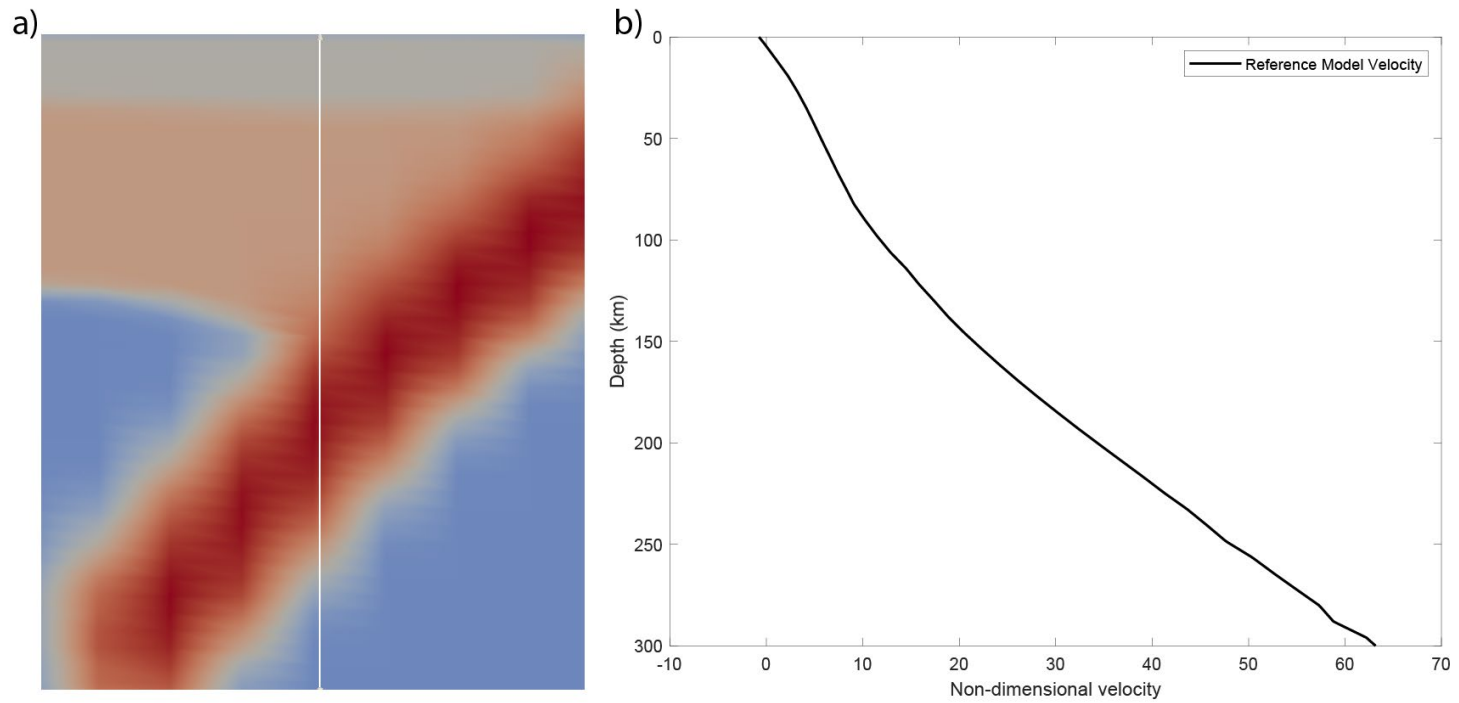
Figure 3.5 Schematic diagram of 2D velocity data analysis showing A, the appearance of the vertical velocity profile (using reference model, version 47) when attempting to plot data along a line in *Paraview*. B illustrates the resulting velocity data of the reference model when plotted in external software *MATLAB*.

any potential flow through a region of missing lithosphere. The velocity calculated when the model solves is non-dimensional in nature, and the exact magnitudes of the velocity depend primarily on the scale of the model.

Data analysis of the velocity profiles is performed in MATLAB and Microsoft Excel, where several useful data points can be analyzed and compared against one another. From the velocity and material field profiles, data is obtained for the velocity at 1000 distinct points, at 1 kilometer spacing from the surface (0 kilometers) to the bottom of the model domain at 1000 kilometers depth. The primary interest is in the upper 300 kilometers and narrowing even further to the region between approximately 125 kilometers depth and 300 kilometers depth in the region of subduction, where the slab hole/tear is located, and flow anomalies are likely. It is in this region where when comparing the velocity profile to the material field profile, the primary changes in velocity are most impactful to the study and most obvious. We calculate an average horizontal velocity for the subducting slab using two data points, the first data point representing the left edge of the subducting slab nose, and the other representing the right edge of the subducting slab nose. Using the profiles, a depth at which the maximum flow through the hole can be obtained for each profile (except the reference models), as well as the magnitude of the velocity at this point. A material field index value is then used to confirm if the material is mantle material. Finally, the magnitude of the velocity anomaly due to asthenospheric flow-through is calculated by subtracting out the background velocity of the slab to determine an "amplitude" for the flow-through velocity.

Models are run in non-dimensional time, and the velocities within are also non-dimensional. Model time and velocity can be scaled to real-world values using a simple relationship between non-dimensional and dimensional time:

$$t = \frac{d}{\bar{v}} \bullet t' \tag{14}$$

where t = real-world time, d = the maximum depth of the model or total height of the model domain, $\bar{v}$ = non-dimensional average particle velocity within the model, and t' = model time. The primary purpose of Eqn 14 is to convert a model time to a real-world time estimate, and subsequently be able to compare the events occurring at two different scales. We assume that the average non-dimensional particle velocity within the model remains constant throughout all models at approximately 66.67. This assumption is reasonable, given that there are no model parameters that change between running individual models, only the size/shape of different slab tears and the slab hole. The depth, d, also remains a constant 1000 km throughout all models such that the time only differs when a model requires data acquisition at different timesteps (the t' term). The approximation to real-world time results in 0.1 Myrs of model time being equal to 1.5 Myrs of real-world time, using the values determined above.

It should be noted that in nearly all two-dimensional models, the continental block uplifts approximately 2.99-4.72 km almost instantaneously, but does so consistently across the entire continental region. This geologically instantaneous uplift is used as a datum elevation, and is the topographical low of the surface tracers along the continental block. The datum elevation could then be used to calculate the total relief across the

continental block for each model by subtracting the datum elevation from the topographic high for a given model.

3.2.4   Specific models used and their respective geometries

Both surface topography and lithospheric gap/asthenospheric flow velocity were analyzed for eleven two-dimensional mechanical models. Table 3.2 lists the details for each of the 2D models run. Each version differs in the geometry and size of slab gap present as well whether regular or flat slab subduction is occurring. Model v152 consists of a "small" lithospheric tear of 30 km width, while the tear in v153 is 65 km in width and the tear in v154 is 85 km in width (Table 3.2). The tears in models v152 – v154 are located on the bottom of the subducting slab. Model v155 is a complete lithospheric gap spanning 30 km. Additionally, there are results presented for three models in which the tears are located on the top of the slab, versions 205, 206, and 208 (Table 3.2). These versions include tears that are of the same geometry and the same small, medium, and large tear size as the bottom slab tears.

To examine the effect that holes may play in geologically momentarily flat slab regions, we have modeled those scenarios in two additional model versions, 194 and 197 (large tear and hole, respectively). These models are compared to a flat slab reference model, version 190, where flat slab subduction occurs under normal circumstances with no lithospheric tearing or holes. Flat slab models consist of a portion of subducting slab that subducts at approximately 33 degrees to a depth of 250 kilometers, to which the slab then becomes horizontal for 200 kilometers at model initiation.

36

Table 3.2 Types of slab tears (and one complete gap) modeled in two-dimensions.

Model	Tear Size	Tear Type	Area (km^2)
v171	None	None	0
v152	Small	Bottom	333
v153	Medium	Bottom	1140
v154	Large	Bottom	1500
v155	Hole	Hole	3000
v205	Small	Top	345
v206	Medium	Top	1050
v208	Large	Top	1450

Error for the calculated areas of each tear is approximately +/- 100 km^2.

3.3   Three-dimensional Mechanical Models

3.3.1   Background, theory, and model design

Similar to the two-dimensional models, the three-dimensional models are designed in *Underworld*, where model design can now occur across a three-dimensional cartesian box (Moresi et al., 2003). Three-dimensional models also solve the same conservation equations 1-3. The Drucker-Prager yield criterion is modified for three-dimensional models, and no longer follows the Mohr-Coulomb criteria but rather a Mohr-Coulomb yield surface (Moresi et al., 2003):

$$\sigma_y = \left(\frac{6 C cos\phi}{\sqrt{3}(3-sin\phi)} \right) + \left(\frac{6 sin\phi P}{\sqrt{3}(3-sin\phi)} \right) \qquad (15)$$

The three-dimensional models used in this study were designed by modifying scripts initially used to study continental accretion in Australia, providing a large model domain with plenty of slab length and width, as well as depth coverage to 800 km (Moresi et al., 2014). In the Moresi (2014) study, a buoyant ribbon was subducted in the trench, but this ribbon was removed as to replicate a simpler subduction zone. The modified slab length for the three-dimensional models is approximately 4500 km, an increase from approximately 3100 km in the two-dimensional models. The total length of the model domain from the left to the right wall is specified at 7000 km, saving space for materials to be left separated from the walls of the model. The model domain is 3000 km in width, and the depth of the domain is 800 km (Figure 3.6). This is an ideal width for the model domain because it allows for implementation of slab gaps and tears without influence from the sides of the model domain. The depth, although shallower than the two-dimensional models, still allows visualization of the mantle transition zone at 660
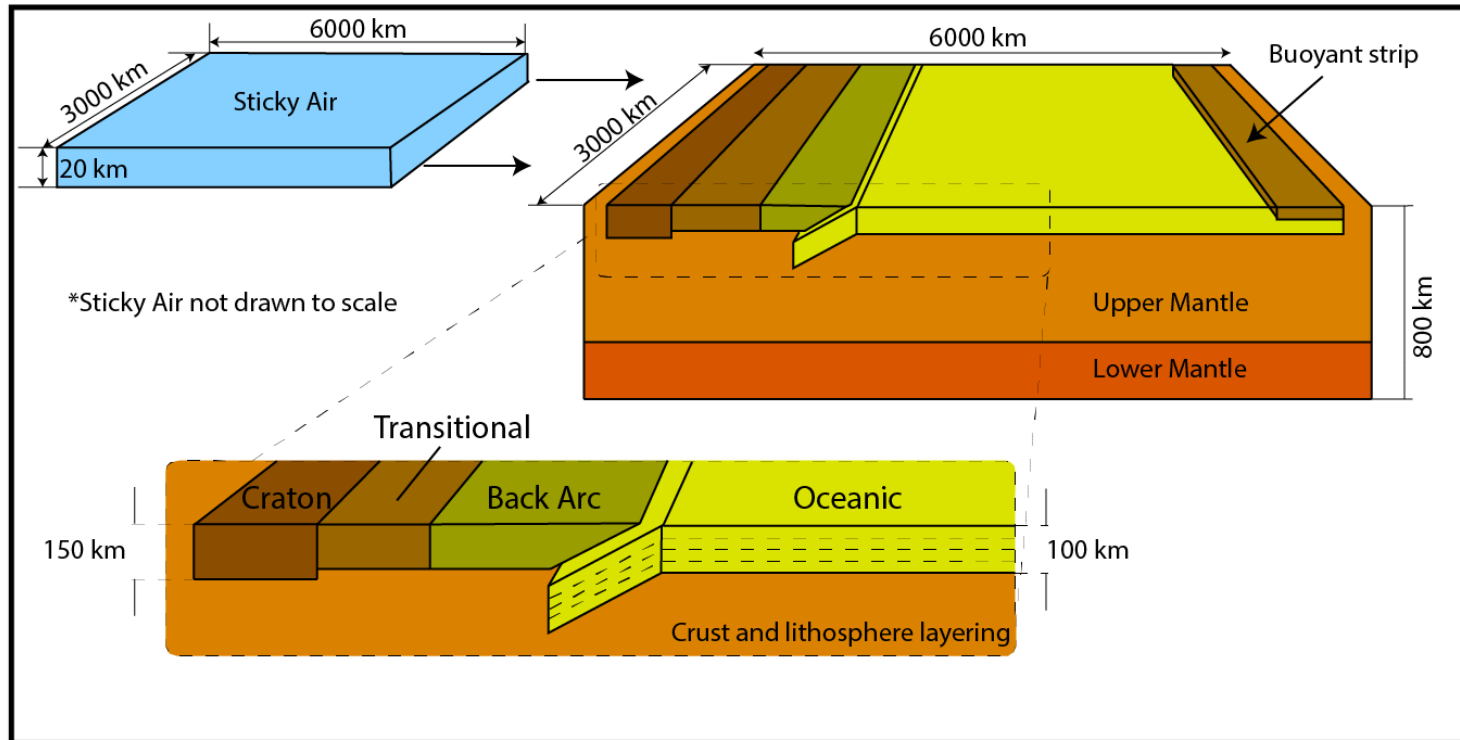
Figure 3.6 Schematic diagram of 3D model setup at model initiation (t = 0) that includes the model materials, model geometry, and size of the model domain used. (Modified from Moresi et al., 2014)

km depth, with greater than 100 km of lower mantle material still present in the model domain.

The number of model materials is increased in three-dimensional models to include 14 materials, with many matching the materials chosen in two dimensions (Figure 3.6, Table 3.3). The materials first specified in the three-dimensional models include an upper mantle layer and a lower mantle layer. The upper mantle layer extends, as it did in two dimensions, from the surface to a depth of 660 km. The lower mantle material begins at 660 km and extends to the bottom of the model domain at 800 km depth. Finally, a sticky air layer similar to the one in two-dimensional models is added above the surface which is 20 kilometers in thickness and serves to monitor three-dimensional surface topography changes as subduction proceeds (Figure 3.6).

The overriding plate is divided into three sections as shown in Figure 3.6. The region closest to the trench (back arc) has two material layers, the first being a stronger, 50 km thick region of back arc material that extends 1200 km horizontally from the trench landward, and the second with the same horizontal extent and thickness but weaker rheology that starts at 50 km depth and extends to 100 km depth. Like the back arc material, the next two continental materials represent a transitional domain in the overriding plate where the lithosphere becomes more compositionally similar to continental lithosphere rather than oceanic (Figure 3.6). These two materials extend from the leftmost back arc 350 km further landward at the same depths and thicknesses as the back arc region. The overriding plate consists of two additional material layers to the far left that have properties representing that of a craton. The lithosphere in this region

Table 3.3 Model parameters for three-dimensional subduction models.

Parameter	Symbol	Value	Units	Parameter	Symbol	Value	Units
Model Geometry				Viscosity of Slab layer 4	η_{sl4}	9.6×10^{21}	Pa s
Sticky air thickness	h_a	20	km	Viscosity of Back-Arc (Top/Bot)	η_{ba}	$5.0 \times 10^{23}/1.7 \times 10^{22}$	Pa s
Continental crust thickness	h_{cc}	125/150	km	Viscosity of Transitional Region (Top/Bot)	η_{tr}	$5.0 \times 10^{23}/1.5 \times 10^{23}$	Pa s
Oceanic slab thickness	h_{oc}	100	km	Viscosity of Cratonic Region (Top/Bot)	η_{cr}	$5.0 \times 10^{23}/1.7 \times 10^{23}$	Pa s
Buoyant material thickness	h_b	50	km	Viscosity of buoyant material	η_b	1.0×10^{25}	Pa s
Mantle Transition Zone Depth	d_{MTZ}	660	km	Model cohesion	c_{mod}	1000	Mpa
Oceanic slab length	ℓ	3300	km	Cohesion: Slab layer 1	c_{sl1}	12.5	Mpa
Model domain width	w_{mod}	3000	km	Cohesion: Slab layer 2	c_{sl2}	67.4	Mpa
Model domain length	l_{mod}	6000	km	Cohesion: Slab layer 3	c_{sl3}	121.3	Mpa
Material Properties				Cohesion: Slab layer 4	c_{sl4}	1000	Mpa
Density of sticky air	ρ_a	1	kg/m^3	*Other Parameters*			
Density of upper mantle	ρ_{um}	3400	kg/m^3	Gravitational acceleration	g	10	m/s^2
Density of lower mantle	ρ_{lm}	3400	kg/m^3	Surface Temperature*	T_{surf}	273.15	°K
Density of Slab layer 1	ρ_{oc1}	2900	kg/m^3	Model Base Temperature*	T_{base}	1573.15	°K
Density of Slab layer 2	ρ_{oc2}	3400	kg/m^3	Thermal Diffusivity*	α	3.0×10^{-5}	K^{-1}
Density of Slab layer 3	ρ_{oc3}	3300	kg/m^3	Thermal Conductivity*	κ	1.0×10^{-6}	m^2/s
Density of Slab layer 4	ρ_{oc4}	3200	kg/m^3	Initial Subduction Angle	Θ	30	° (deg)
Density of Back-arc (Top/Bot)	ρ_{ba}	3000/3100	kg/m^3				
Density of Transitional Region (Top/Bot)	ρ_{tr}	2900/3100	kg/m^3				
Density of Cratonic Region (Top/Bot)	ρ_{cr}	2800/3100	kg/m^3				
Density of buoyant material	ρ_b	2800	kg/m^3				
Viscosity of sticky air layer	η_a	1.5×10^{19}	Pa s				
Viscosity of upper mantle	η_{um}	1.0×10^{20}	Pa s				
Viscosity of lower mantle	η_{lm}	1.0×10^{22}	Pa s				
Viscosity of Slab layer 1	η_{sl1}	1.0×10^{25}	Pa s				
Viscosity of Slab layer 2	η_{sl2}	1.0×10^{25}	Pa s				
Viscosity of Slab layer 3	η_{sl3}	1.9×10^{24}	Pa s				
Notes: *Temperature related parameters are not assigned to the model, only used to determine the viscosity and density profiles upon initialization							

Top/Bot indicates the uppermost (nearest surface) or lowermost (deeper) section of the given material.

extends to a depth of 150 km to represent thicker crust with the upper material layer ending at 75 km depth and is rheologically stronger.

The subducting slab now consists of four layers, each are 25 km in thickness and range from beneath the overriding plate to a few hundred kilometers away from the edge of the model domain on the right wall. The final material added to the model domain is a buoyant strip that sits atop oceanic lithosphere at the far right of the model domain, which helps keep the slab afloat atop the less dense upper mantle, thus preventing any unwanted double-sided subduction while simultaneously not influencing the behavior of the slab at the trench.

In the three-dimensional models, pressure and temperature-dependent relationships were used in calculating viscosity, density, and cohesion parameters and were based on commonly accepted values for a half-space cooling model (Moresi et al., 2014). Each model material consists of viscosity, density, and plasticity/strength values (see Table 3.3) calculated using temperature and pressure-dependent rheologies beginning with a half-space cooling model for oceanic lithosphere where the temperature at the surface and bottom of the model are assumed (Moresi et al., 2014):

$$T(y, t) = T_{surf} + (T_{Bot} - T_{surf})\text{erf}\left(\frac{y}{2\sqrt{t\kappa}}\right) \tag{16}$$

where T is the temperature at the given depth (y) and age (t), T_{surf} is the temperature at the surface, T_{Bot} is the temperature at the bottom of the model domain, and κ is the thermal conductivity of the material.

The continental materials have temperatures calculated individually for each region due to lithospheric thickness changes between the craton and other continental

materials, thus multiple geotherms are utilized but they are all governed by the same general relationship:

$$T(y) = y \left(\frac{T_{Bot} - T_{surf}}{h + T_{surf}} \right) \qquad (17)$$

where h is the thickness of the lithosphere in the region. The continental materials are not age dependent like the oceanic lithosphere is, because we assume the age of continental materials to be a negligible factor in the behavior of the subducting slab in the trench and at depth.

Pressures within the model domain are calculated using a simple lithostatic pressure relationship (as they are in two-dimensions):

$$P(y) = \rho g y \qquad (18)$$

where P is the pressure at the given depth (y), ρ is the density of the material, and g remains to be gravitational acceleration.

The viscosities of a given material layer are then calculated using an Arrhenius viscosity relationship given the temperature and pressures calculated previously:

$$\eta(T, P) = \exp\left(\frac{E + VP}{RT} \right) \qquad (19)$$

where η is the viscosity of the material, T and P remain the temperature and pressure, respectively, E is the activation energy of the system, V is the activation volume, and R is the universal gas constant.

3.3.2   Computational resources used for 3D model execution

Like with the two-dimensional models, three-dimensional models were computed using the LCC supercomputer at UK. In these 3D cases, the computational cost was far greater, and thus motivated the major changes to model design from two to three dimensions. Because of the addition of a slab width to the model, the number of model particles rose exponentially, even with a decrease in overall model resolution. The maximum usable particle resolution in three-dimensional models was 96 elements per cell in the length (x) dimension, 64 elements per cell in the depth (y) dimension, and 96 elements per cell in the width (z) dimension. Thus, the total number of model particles added to the swarm is 589,824, all of which must be advected through the model at each timestep. Using any higher resolution resulted in failure of the model run due to out-of-memory errors.

3.3.3   Three-dimensional data analysis

Because of the added width dimension to the model domain, surface topography variations are analyzed along two slices/transects/lines along trench and perpendicular to the trench across the overriding continental plate. These variations are visualized across the entire width of the slab, including near model domain edges, but we focused on approximately 300 kilometers nearest the trench (a 300 km x 3000 km region) to discuss the topography changes in and near the primary orogenic belt generated in each simulation. The surface topography data is acquired from *Paraview* software like in two-dimensions, however this time gridded data across the continental surface is pulled rather than a line of data points.

In *MATLAB,* the gridded data is visualized through contour plots in map view and contoured surface plots to observe changes in all directions. Both plots use a scattered interpolant function to interpolate data points between gridded data. The grid spacing is set to 5 kilometers in the length dimension of the model when recreating the grid in *MATLAB.* The data is also visualized in one-dimensional profiles that run through the point of maximum topography of each model using the same interpolated data points and are perpendicular to the trench. In addition to these trench-perpendicular profiles, trench/orogen-parallel profiles are also produced to analyze changes in topography along the width of the model domain. The curvature of the subduction zone was approximated by using the following equation (also visualized in Figure 3.7):

$$C \approx \frac{\Delta x}{\Delta t} \tag{20}$$

where C represents the curvature of a particular stretch of the orogen, Δx represents the change in the x (length direction, perpendicular to trench), and Δz represents the change in the z (width direction, parallel to trench). A comprehensive study of the velocity profiles through lithospheric gaps in three dimensions is not performed due to velocity signatures mostly being overwritten by larger geodynamical processes such as sinking of the slab and larger scale mantle convection flow patterns. Velocity field files were examined, however, and subduction of the three-dimensional slab and flow into the mantle wedge from the left showed much larger velocities than that of any asthenospheric flow through the slab gaps present, thus, no reliable velocity data could be collected.

An additional step is taken in visualizing the three-dimensional trends, which involves the fitting of a 10th order polynomial to the surface topography data in profiles
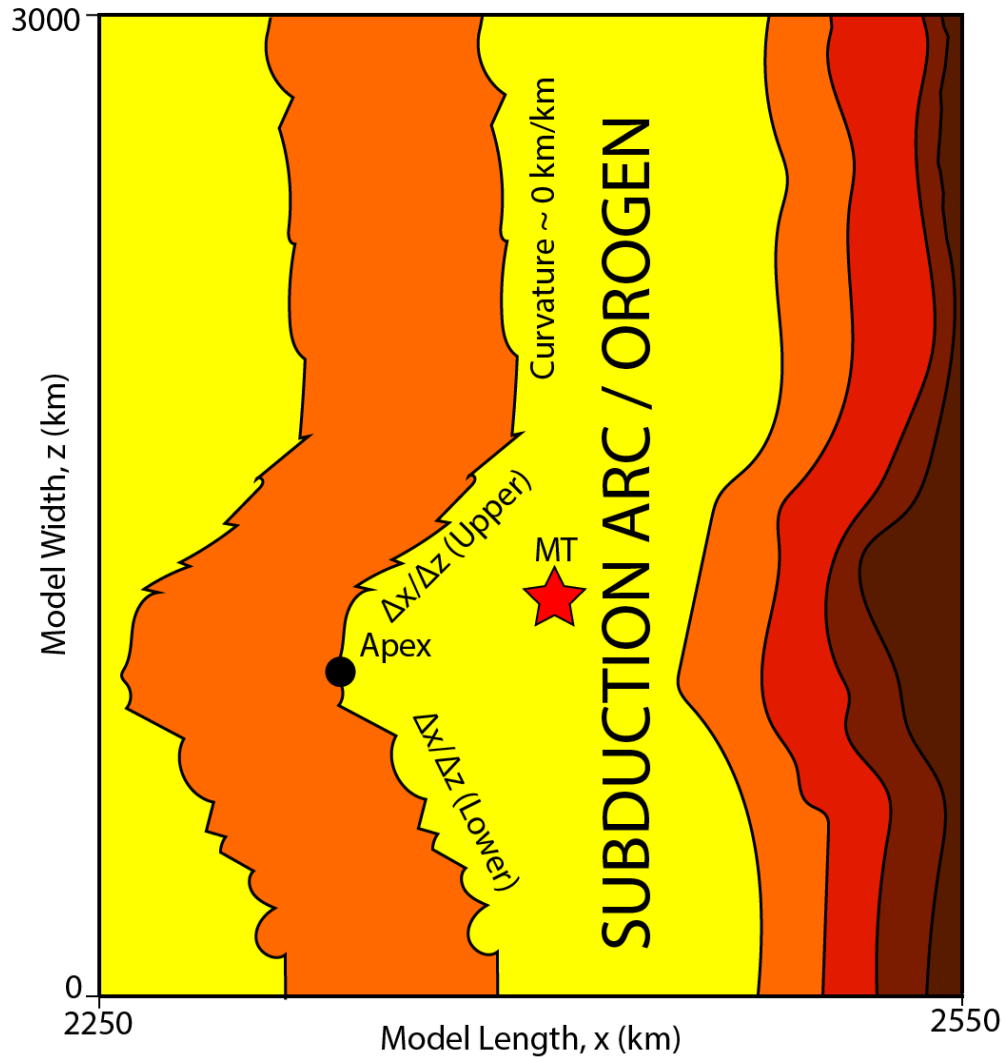
Figure 3.7 Schematic image of an example of curvature in a Map View profile of a three-dimensional subduction model. The apex is illustrated with a black dot that indicates the maximum extent of the curvature in the particular signature. Maximum Topography (MT) is illustrated by the red star. The subduction arc/orogen is labelled and contains the yellow "contour" to the right of the apex. Curvature is approximated using the change in kilometers in the Model Length divided by the change in kilometers in the Model Width once the orogen begins curving until it reaches the apex. The calculation is then made again on what we refer to as the Upper section of the curvature signature. Regions like that above the upper section in this schematic have approximately 0 curvature.

taken parallel to the trench. The purpose of this is not to quantitatively describe data

trends, but rather to make the desired trend more observable in the data. Thus, the 10th

order polynomial acts as a low pass filter in which only the low frequencies (long

wavelength topography) are allowed to pass through. This filters out higher frequency

data that may arise due to plotting and resolution errors in the surface topography grid,

which in turn makes the long wavelength topography along the orogen easier to visualize.

3.3.4   Three-dimensional models and their geometries

This study presents the findings of fourteen three-dimensional models of varying

hole geometries (Figure 3.8), and the details of all model parameters are found in Table

3.4. Model versions 34 through 37 consist of singular square or rectangular slab holes in

which the size of the hole increases in one or both dimensions (Table 3.4). These versions

illustrate the differences in resulting surface topography depending on the size of the slab

hole or volume of missing lithosphere. Model version 46 represents a scenario in which a

slab hole is offset from the center of the model domain to show that the observed features

resulting from slab holes will follow the hole, regardless of the position of the hole in the

model domain (i.e. no side wall interference). The reference model for three-dimensional

cases is model version 47 which includes no lithospheric/slab gap.

Additionally, the shape of the slab hole is altered to a large circular hole (version

56) to discuss any changes that the shape of the hole may have in resulting surface

topography or subduction zone curvature. In model versions 57 and 58 there is the

addition of a "slit" to the subducting lithosphere, where the hole through the slab is

substantially longer in one dimension than the other. In version 57, the slit is much longer

Table 3.4 Three-dimensional models and the associated hole geometry.

Model	Hole Length	Hole Width	LVM
v34	50	50	250000
v35	100	100	1000000
v36	150	150	2250000
v37	125	250	3125000
v46	150	150	2250000
v47	None	None	None
v56	Circ	Circ	1767146
v57	150	50	750000
v58	50	250	1250000
v63	130	150	1950000
v61	130	150	1950000
v62	130	150	1950000
v59	130	150	1950000
v64	130	150	1950000
v65	130	150	1950000
v60	130	150	1950000

Lithospheric Volume Missing abbreviated LVM.
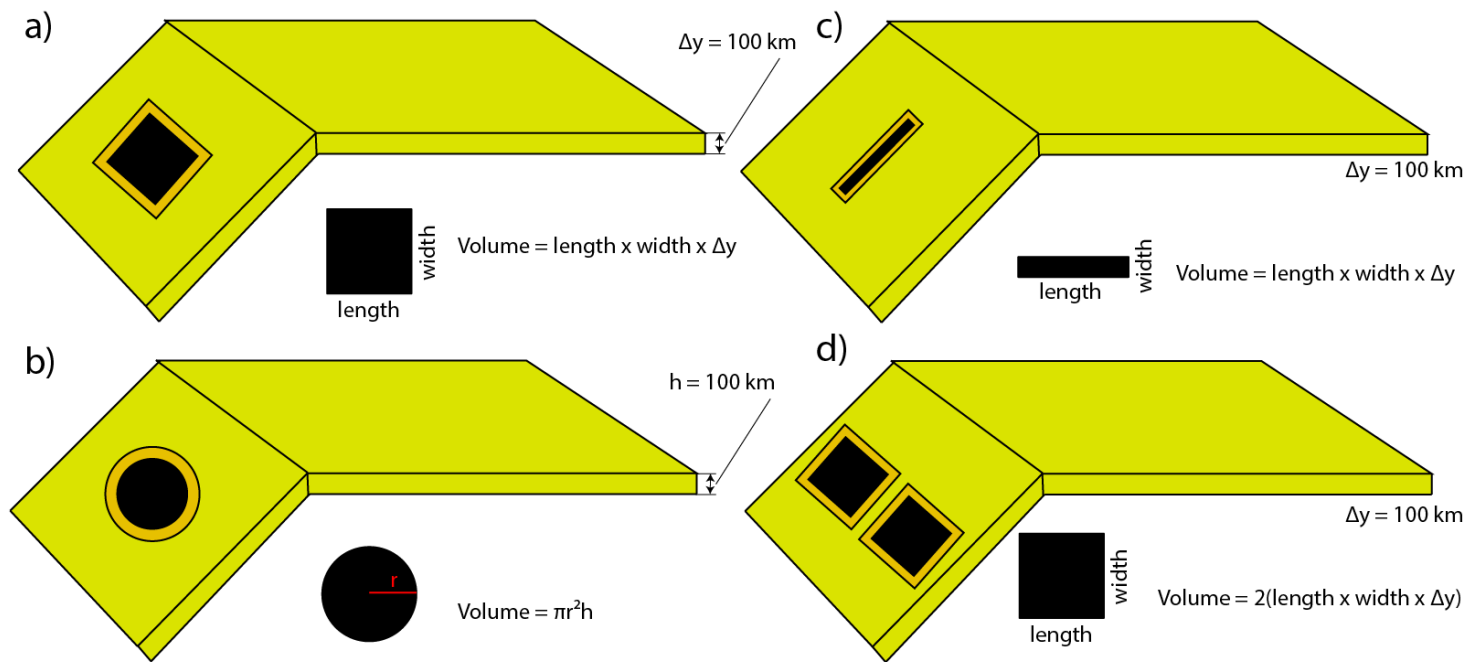
Figure 3.8 Schematic image showing how slab holes are added/cut into the slab at model initiation, in addition to the calculation of Lithospheric Volume Missing (LVM) due to the presence of the slab hole. A shows a square hole being added to the nose of the subducting slab, with volume calculated by multiplying the length and width of the square or rectangle by the thickness of the slab (constant 100 kilometers). B shows a circular hole being added to the nose of the slab, with volume being calculated by the formula of volume for a cylinder. C shows another addition of a rectangle thin enough to be referred to as a slit, a thin hole, with volume calculated by the same formula as A. D shows the addition of two holes added to the subducting slab, the volume of which is determined the same as in A but multiplied by two.

in the length dimension, while in version 58 the slit is much longer in the width dimension. Finally, a suite of models are ran to examine the topographical signature of multiple slab holes along the width of the slab at various distances separating one another (versions 59 through 63).

The code used can be found in the Appendices. The MATLAB scripts used throughout the research for visualization purposes and some calculations can be found in Appendix 1. The Jupyter notebooks containing the code for the different models can be found in Appendix 2.

CHAPTER 4. RESULTS

4.1   Two-dimensional Mechanical Models

The following subsection details the model results outlined in Tables 4.1 and 4.2. The results presented for each model involve the surface topography findings alongside the magnitude of particle velocity along the vertical profiles taken for the given model. The results begin with the two-dimensional reference model and proceed towards larger slab holes with each further subsection discussing a new size slab hole, with one case being on the top of the slab and one on the bottom. Models of flat slab cases are included here with results presented in the same manner as the normal subduction cases. Two-dimensional results conclude with the analysis of the magnitude of maximum surface topography and the amount of missing lithosphere from the slab.

4.1.1   Reference Model (v171)

The reference model (v171) has no introduction of slab holes, tears, or windows in the subducting lithosphere. This model is used as a normal subduction scenario so that comparisons could be made regarding surface topography and asthenospheric flow between models with no missing lithosphere and this one. The reference model had a topographical high of 6.59 km (Figure 4.1, Table 4.1), the highest peak of the normal two-dimensional mechanical models, located 105 km left of the trench, and 193 km from the original initial position of the trench at a horizontal distance of 1200 km (Figure 4.1, Table 4.1). This implies the trench advanced a total of 88 km over the course of the 1.0 Myr model time, a real-world equivalent calculated time of approximately 15 Myrs.

Table 4.1 Surface topography results from eleven two-dimensional subduction models.

Model	MT (km)	Datum Elev (km)	MT-D (km)	MTL (km)	DFT (km)	TM (km)	Time (Myr)	ATMR (km/Myr)
v171	6.59	4.07	2.52	1007	105	88	15.0	5.9
v152	6.52	4.30	2.22	990	124	86	15.0	5.7
v153	6.06	3.88	2.18	1005	117	78	18.0	4.3
v154	5.60	4.65	0.95	164	991	45	13.5	3.3
v155	6.83	4.72	2.11	65	1112	23	12	1.9
v205	6.42	4.14	2.28	1005	101	94	16.5	5.7
v206	5.66	4.45	1.21	163	992	45	13.5	3.3
v208	5.71	4.33	1.38	164	1007	29	10.5	2.8
v190	6.96	2.99	3.97	951	128	121	12	10.1
v194	7.02	3.97	3.05	961	127	112	15	7.5
v197	6.69	3.75	2.94	965	114	121	13.5	9.0

MT is the maximum topography observed across the continental surface tracers. MT-D is the datum elevation subtracted from the maximum topography that gives an estimate of the maximum relief across the continental block. MTL is the horizontal location of the maximum topography. DFT is the distance the maximum topography is from the trench at the time of data acquisition. TM is the amount of trench migration that occurred during the simulation. The time listed is real-world time. The ATMR is the average trench migration rate in the model over the course of the simulation.

Table 4.2 Velocity profile data results for eight normal subduction cases and three flat slab subduction cases.

Model	ASV	MFV	MFD (km)	MI	Amplitude
v171	41.66	NA	NA	NA	0
v152	███	2.98	161	6.18	0.57
v153	███	10.05	161	4.73	2.67
v154	███	-3.04	162	3.53	1.34
v155	███	-14.09	201	4.80	2.39
v205	███	11.56	177	4.22	0.82
v206	███	22.24	169	3.07	11.31
v208	███	19.79	177	3.07	10.52
v190	0.72	NA	NA	NA	0
v194	███	19.49	169	4.51	1.21
v197	███	2.71	193	3.88	0.46

ASV = Average Slab Velocity, only calculated for reference models where no lithosphere is missing, MFV = Maximum Flow Velocity, calculated at the point of maximum flow within the anomalous profile region, MFD = Maximum Flow Depth, the corresponding depth that the maximum flow velocity occurs, MI = Material Index, represents the material index at the depth of maximum flow velocity.
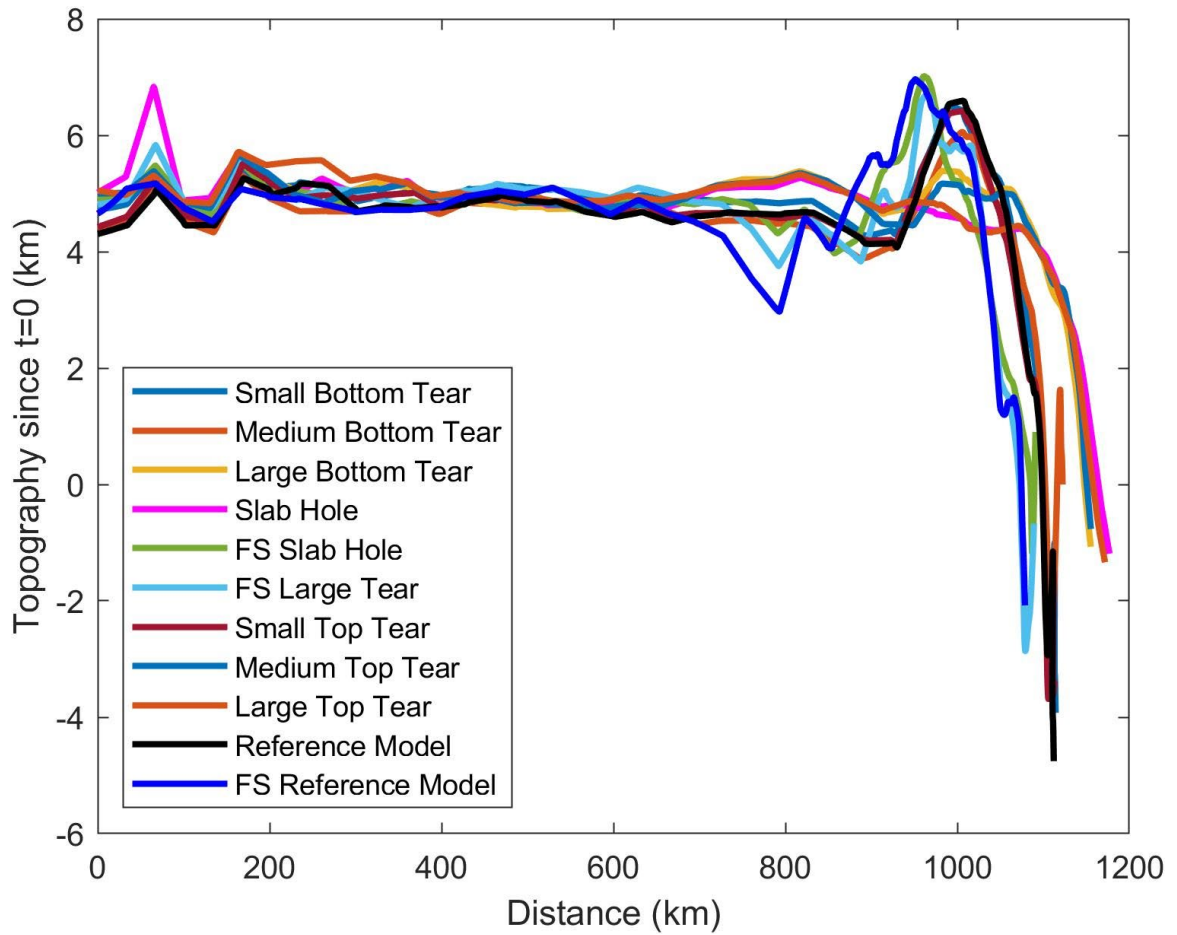
Figure 4.1 Plot of surface topography in the eleven two-dimensional subduction models including all normal cases and flat slab subduction cases, as well as their respective reference models.

Using these times and velocities, the trench migrated at an average rate of 5.9 km/Myr in the landward direction, aided by convergence from the overriding plate. Surface topography may also be referenced back to a datum elevation since all models experienced nearly the same amount of base uplift nearly instantaneously (Table 4.1). For the reference case (model version 171), the immediate uplift contributed approximately 4.07 km to the total uplift across the region (Figure 4.1). The surface topography derived from model surface tracers consists of the instant uplift, and then moving rightward gains several kilometers of elevation that represents the orogen before quickly descending in the trench of the subduction zone.

The non-dimensional slab velocity in the reference case is on average, 41.66 (Table 4.2). Particles representing the uppermost section of the slab moved slower, at a minimum of 27.53, while the particles near the bottom of the slab were moving much faster in the horizontal direction, approximately 55.78 (Table 4.2). Velocity components discussed in other model versions are not present in this model because no flow velocity is being monitored through the slab because there is no lithospheric gap. In the reference model, the maximum velocity is in the upper mantle beneath the subducting slab. The velocity then decreases until the transition zone, where the velocity slows towards 0 at the bottom of the model domain, corresponding to the boundary condition that is set forth in the model setup (Figure 4.2).
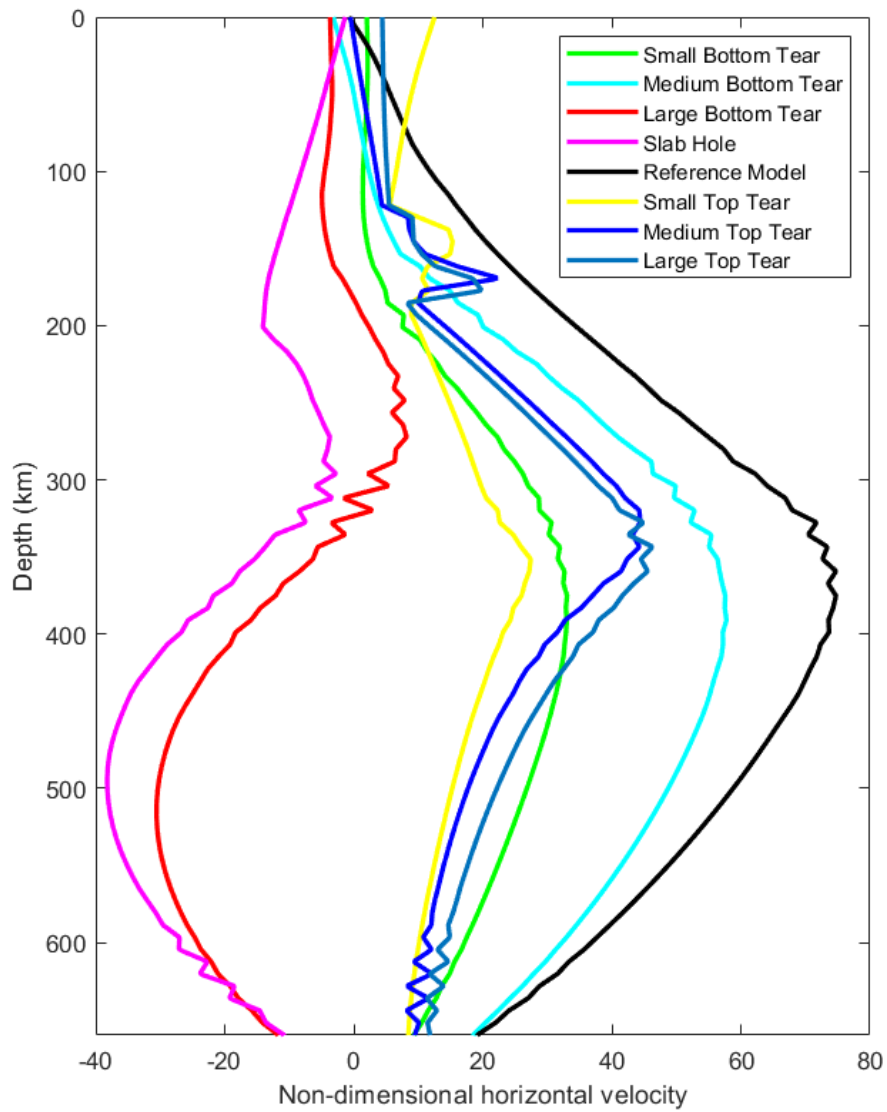
Figure 4.2 Vertical velocity profiles of all two-dimensional models ran excluding flat slab models. Negative velocities indicate leftward movement within the model domain, while positive velocities indicate movement of particles to the right.

4.1.2 Small slab tear models (v152 and v205)

The following subsection presents the findings of two models in which a small tear is added to the subducting lithosphere, one to the bottom of the slab (version 152), and one on the top (version 205). The missing area of slab from these holes is approximately 333 km^2 and 345 km^2, respectively. The results of each model are presented beginning with surface topography data in Table 4.1 with relevant observations and concluding with the velocity data further presented in Table 4.2.

4.1.2.1 Model version 152

This model (version 152) features the smallest lithospheric gap we studied and is located on the bottom side of the slab. It produced a maximum surface topography of 6.52 km, located about 124 km from the trench at the time of data acquisition, and about 210 km horizontally from where the trench began at the initial time (Figure 4.1,4.3-4.5, Table 4.1). This implies a trench migration of approximately 86 km over the course of 1.0 Myrs model time (real-world equivalent of 15.0 Myrs), to which the average trench migration velocity was calculated to be 5.7 km/Myr (Table 4.1). Topographical features in this version tend to follow the same pattern and location of the reference model, starting at the left with the uplifted "plateau", transitioning into an orogenic belt, and then to the deep ocean trench at the far left (Figure 4.1, 4.3-4.5). The datum elevation for this model is set to 4.30 km based on the initial uplift.

Tracers monitoring flow around the basal slab tear bend inwards at the edge of the tear, implying potential for attempted asthenospheric flow. In quantification of the flow
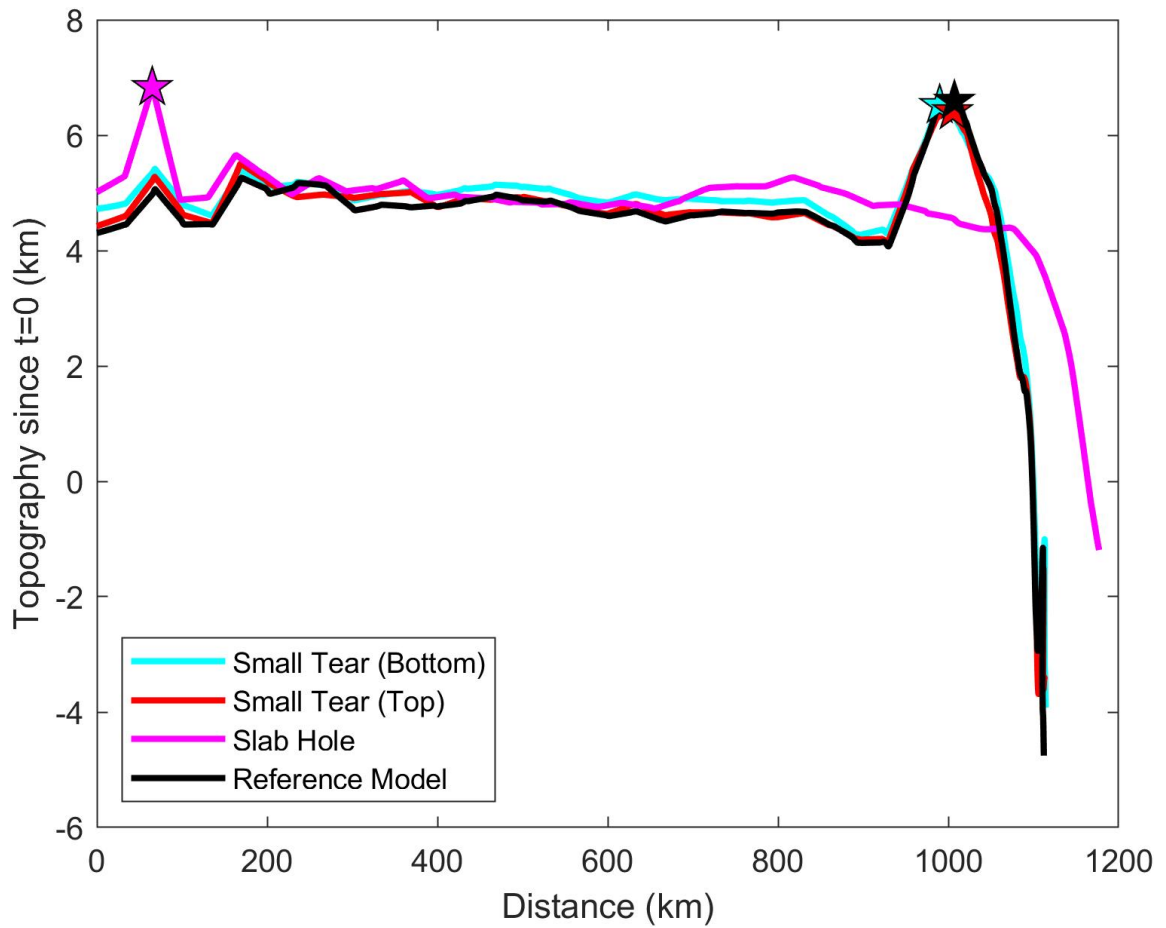
Figure 4.3 Surface topography of four subduction models presented that encompass all small slab tears introduced to the subducting slab (v152, v205), compared to the reference model (v171) and slab hole model (v155). Topography captured at 15 Myrs and 16.5 Myrs, respectively, for the small tears visualized.
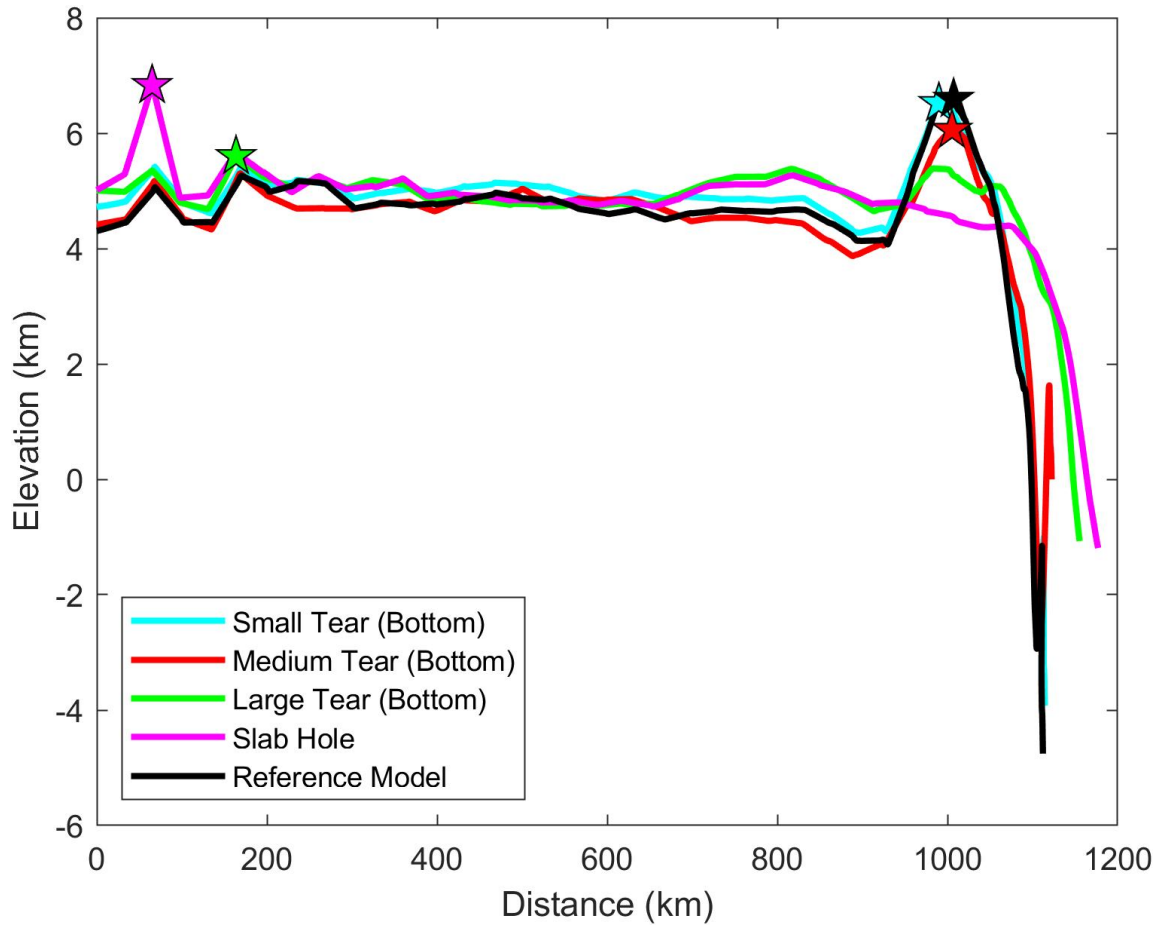
Figure 4.4 Surface topography of five subduction models presented that encompasses all slab tears introduced to the bottom of the subducting slab at varying sizes (versions 152-154), compared to the reference model (v171) and the model of a slab hole (v155). Topography captured at 15 Myrs, 18 Myrs, and 13.5 Myrs, respectively for the small tear models presented.
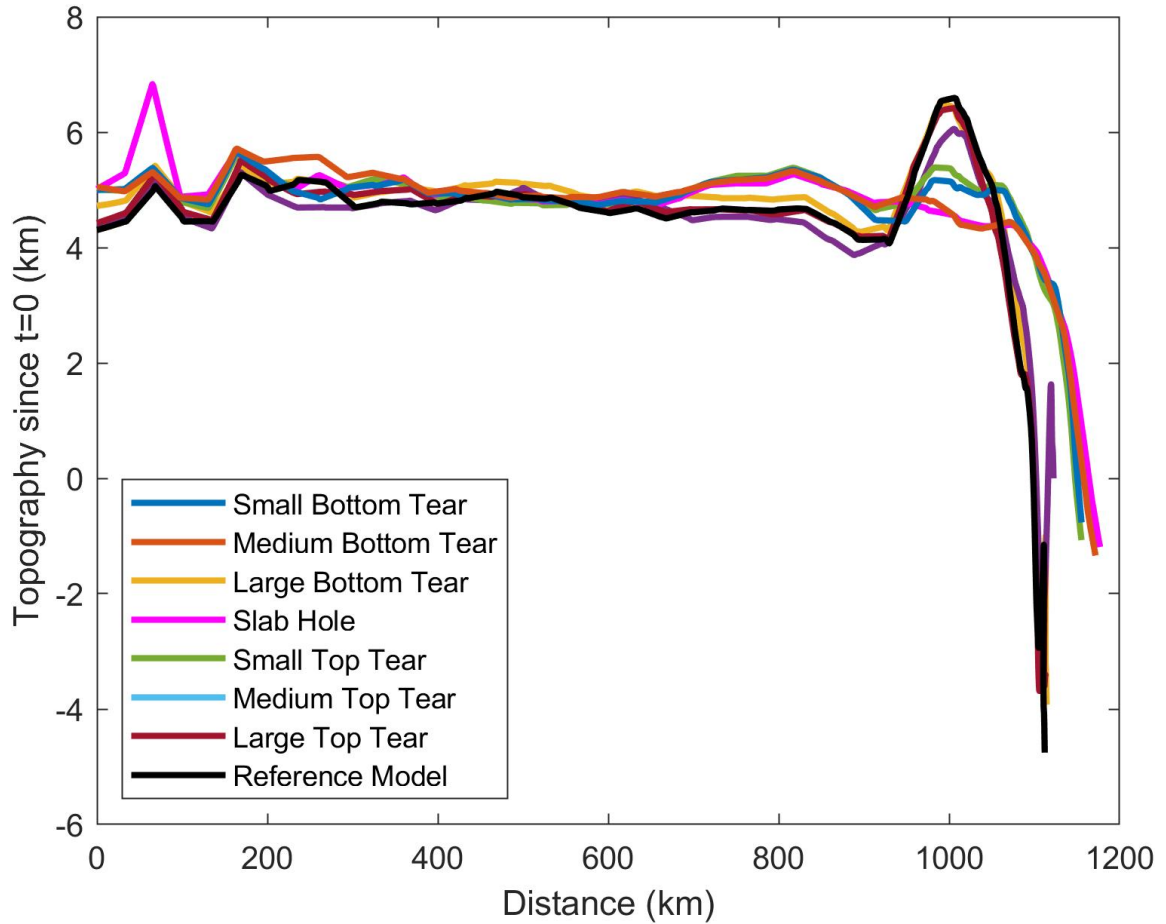
Figure 4.5 Surface topography plot of eight subduction models in which the slab subducts in a normal manner from initiation. Reference model (v171) and complete lithospheric gap (v155) models included. Topography for reference model captured at 15 Myrs, and topography captured for slab hole model at 12 Myrs.

field across the vertical velocity profile measuring the non-dimensional horizontal velocity, the maximum velocity identified as potential flow into the gap is 2.98 (Figure 4.6, Table 4.2). The depth at which this velocity occurs is 161 kilometers beneath the surface at a horizontal distance of 1070 kilometers from the left wall, and about 120 kilometers from the horizontal trench position at data acquisition. The corresponding material index for this data point is 6.18, the lowest material index value in this region of the profile, indicative of a shift of the model material here to being momentarily mantle material rather than slab material. The amplitude of the velocity anomaly is defined as the difference between the peak change in velocity from the background slab velocity in the region of the slab gap. The non-dimensional velocity anomaly amplitude for model version 152 is approximately 0.57 (Figure 4.6, Table 4.2).

4.1.2.2   Model version 205

The second model containing a small lithospheric gap is version 205 which features a small tear on the top part of the slab. This model has the best topographic fit to the original reference model (Figure 4.7). The highest point of surface topography produced from this small tear model was 6.42 km, the fourth highest topographical peak of the normal subduction models (Table 4.1). The datum elevation in this model is 4.14 km. This topographical high point is located 101 km leftward from the trench at the time of data collection, and about 195 km away from the initial trench location, similar to the version 152 with the small tear on the underside of slab. The trench migrated a total of 94 km over the course of 1.1 Myrs model time, equivalent to a real-world time of 16.5 Myrs. The average trench migration for version 205 is thus 5.7 km/Myr (Table 4.1).
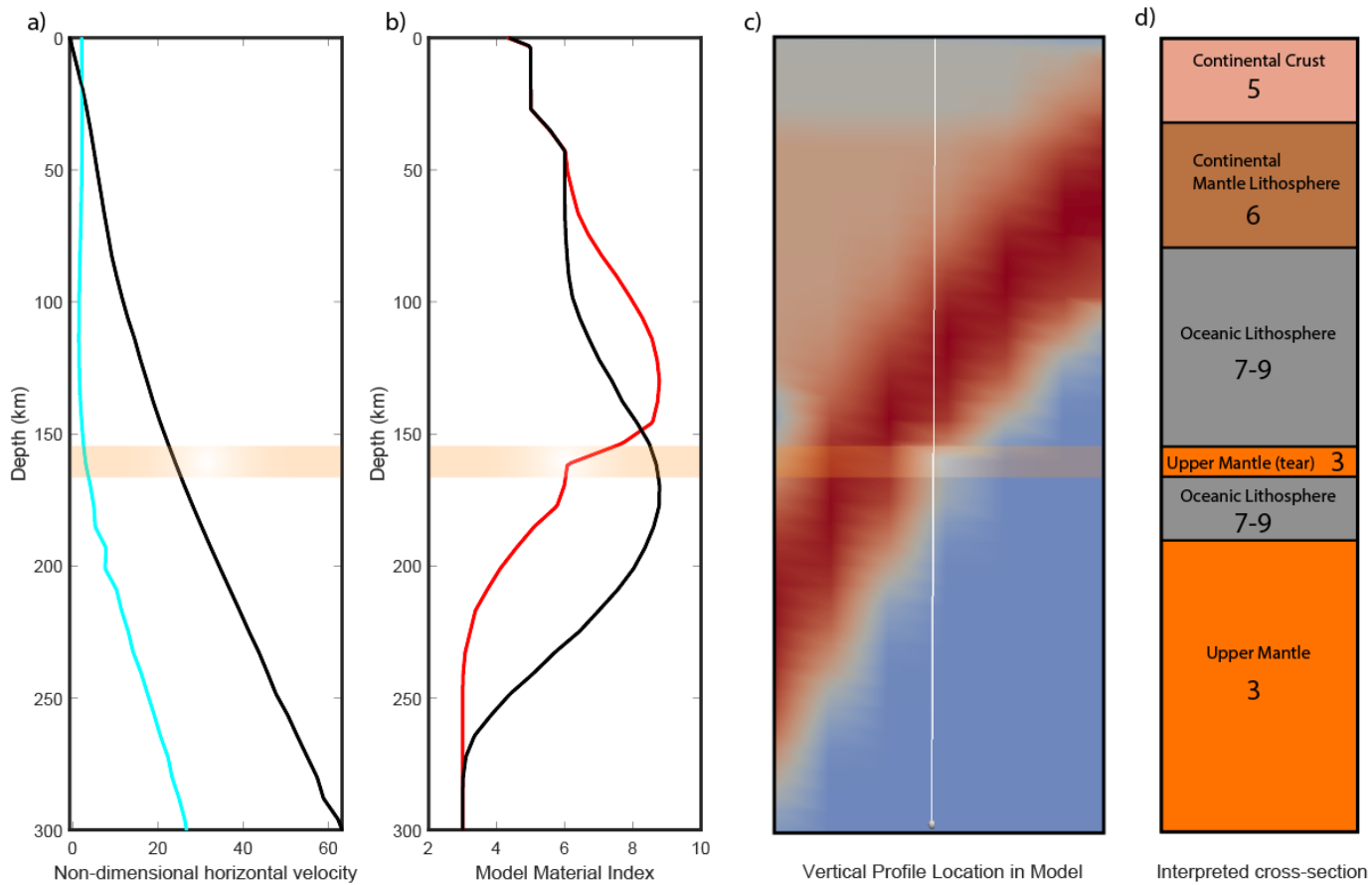
Figure 4.6 Velocity data for model version 152, with a small tear to the base of the lithosphere. A shows the velocity data for the horizontal component, with the black line indicating the reference case and the cyan line indicating velocity in version 152. B shows the corresponding material field at the same depths. C shows a snapshot of the location of the profile where the data in A and B were taken. D, a representation of the interpreted cross section of the model materials present through the profile.
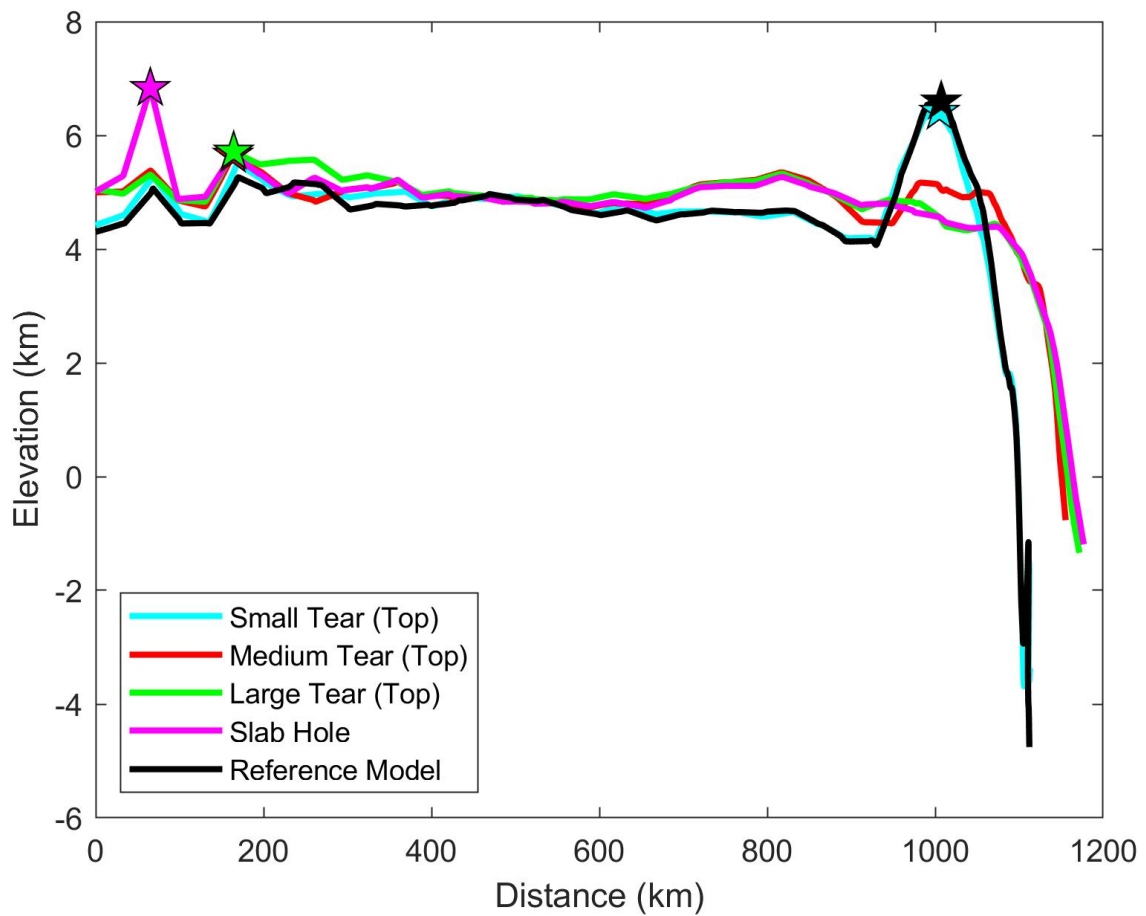
Figure 4.7 Surface topography of five subduction models presented that encompass all slab tears introduced to the top of the subducting lithosphere at varying sizes (versions 205, 206, and 208), compared to the reference model (v171) and slab hole model (v155). Topography captured at 16.5 Myrs, 13.5 Myrs, and 12 Myrs, respectively for the tears visualized.

Subsequently, this version did not show any penetration of mantle material through the slab, however flow-monitoring tracers bend towards the missing lithosphere of the slab, a sign of attempted asthenospheric flow. Additional evidence of potential flow comes from the velocity profile data through the lithospheric gap which shows a non-dimensional horizontal particle velocity of 11.56 at a depth of 177 km (Figure 4.8a) (in the lithospheric gap). This velocity high corresponds to a material field value of 4.22 at this exact same depth (Figure 4.8b) which means the velocity is flow of upper mantle material, and is visualized in the profile (Figure 4.8c) with a visual cross-section aid (Figure 4.8d). The amplitude of the non-dimensional velocity anomaly at 177 km depth is approximately 0.82. The average non-dimensional horizontal slab velocity determined in the nose from this profile (Figure 4.8c) is 12.86.

4.1.3   Moderate slab tear models (v153 and v206)

The following subsection presents the findings of two models in which a moderate/medium tear is added to the subducting lithosphere, one version where the tear is added to the bottom (version 153), and one version where the tear is on the base of the slab (version 206). The areas of missing lithosphere increase for these versions to 1140 km^2 and 1050 km^2, respectively. The results of each model are presented beginning with surface topography data located in Table 4.1 with relevant observations and concluding with the velocity data further presented in Table 4.2.
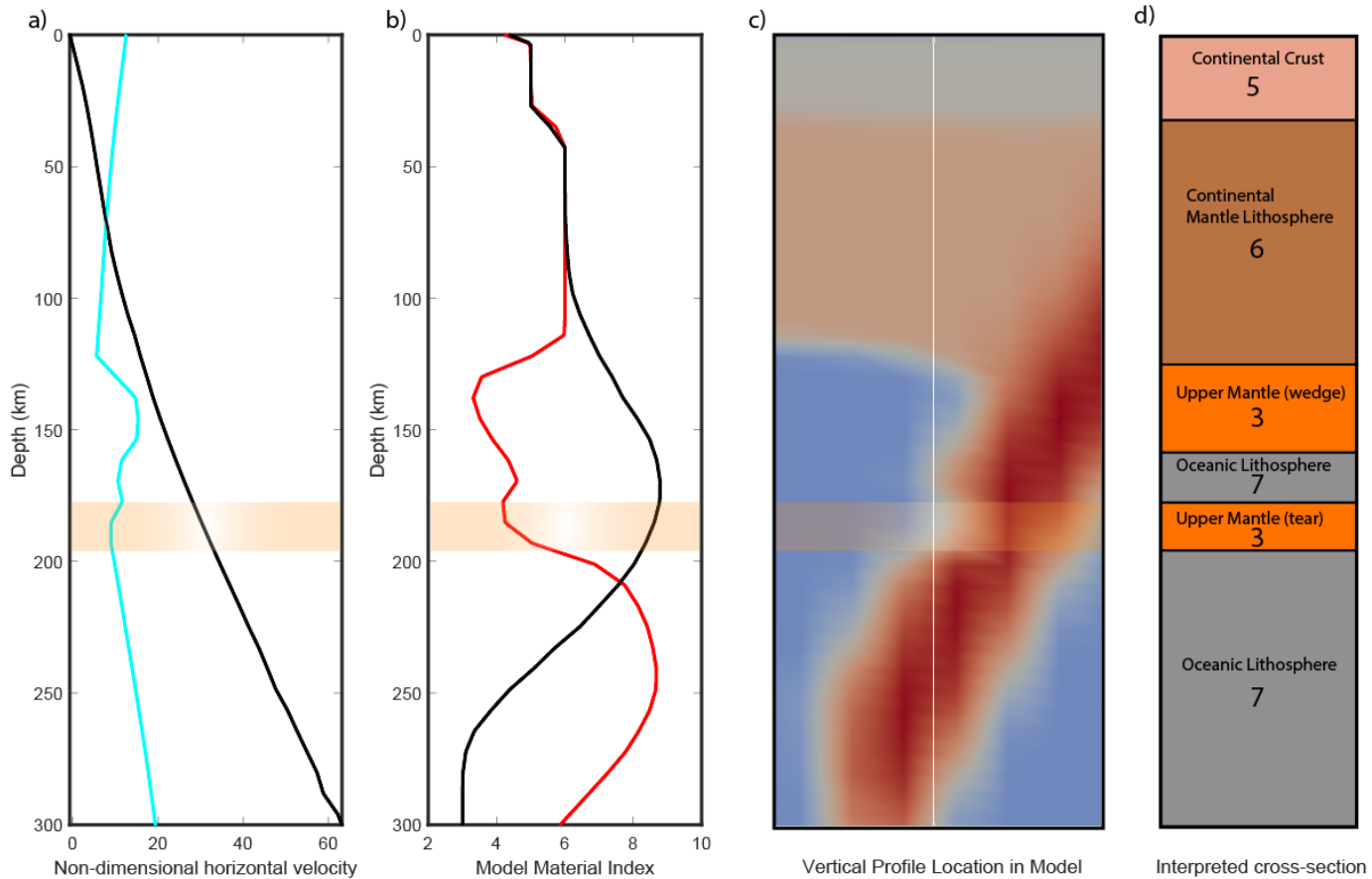
Figure 4.8 Velocity data for model version 205 involving a small tear to the top of the subducting lithosphere. A shows the velocity data in the horizontal component, with the black line indicating the reference case and the cyan line indicating velocity in version 205. B shows the corresponding material field at the same depths. C shows a snapshot of the location of the profile where the data in A and B were taken. D, a representation of the interpreted cross section of the model materials present through the profile.

4.1.3.1   Model version 153

A significant amount of lithosphere is missing in version 153, the first model with a moderate sized slab tear located on the bottom/basal side of the slab. The highest point of surface topography produced from the medium slab tear is 6.06 km, located 117 km from the trench at data collection, and 195 km from the trench at the initial model timestep (Figure 4.9, Table 4.1). The trench migrated 78 km in this version, which occurred over the course of 1.2 Myrs, the equivalent of 18.0 Myrs real-world time. Thus, the average trench migration during this time is 4.3 km/Myr (Table 4.1). The datum elevation referred to for this model is 3.88 km.

Evidence for asthenospheric flow through the slab hole is visualized in tracers placed at the top and bottom of the slab, where particles on both sides of the slab travel into the weak zone in the lithosphere. Given that slab breakoff did not occur in this model version, flow does not breach the slab to enter the mantle wedge from beneath, but likely does enter the tear (Figure 4.10). The maximum non-dimensional flow velocity present that corresponds to the slab gap in version 153 is 10.05, which occurs at the same depth as that of version 152, 161 kilometers (Table 4.2), which is approximately 130 kilometers away from the trench location at data acquisition, 1060 kilometers away from the left wall. The material index for the data point with maximum flow is 4.73 which still approximates upper mantle material. The non-dimensional amplitude is calculated to be 2.67 for the flow velocity anomaly (Figure 4.10, Table 6).
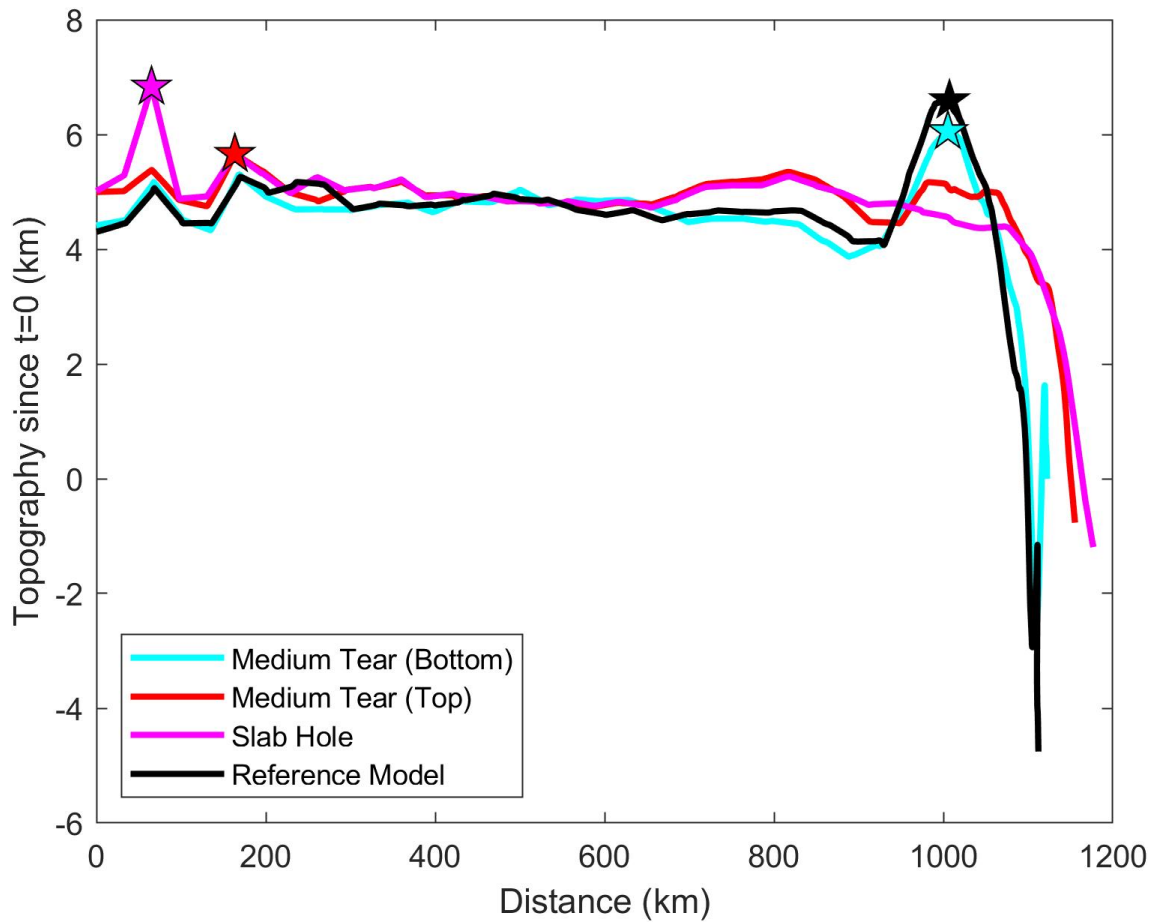
Figure 4.9 Surface topography results for four subduction models presented that encompass all medium slab tears introduced to the subducting slab (v153, v206), compared to the reference model (v171) and slab hole model (v155). Topography captured at 18 Myrs and 13.5 Myrs, respectively, for the medium tears visualized.
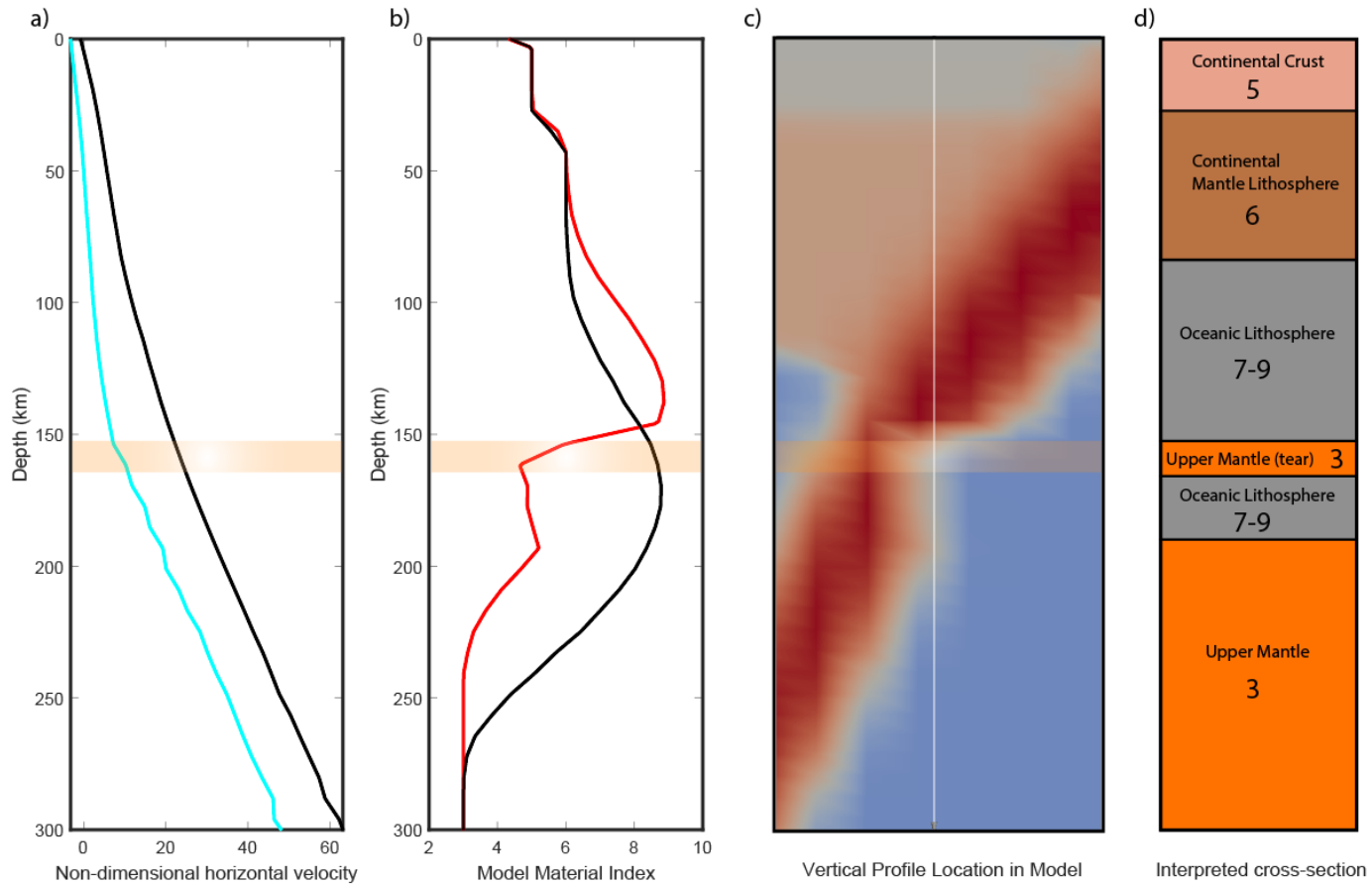
Figure 4.10 Velocity data for model version 153, with a medium tear to the base of the lithosphere. A shows the velocity data for the horizontal component, with the black line indicating the reference case and the cyan line indicating velocity in version 153. B shows the corresponding material field at the same depths. C shows a snapshot of the location of the profile where the data in A and B were taken. D, a representation of the interpreted cross section of the model materials present through the profile.

4.1.3.2   Model version 206

The second medium tear modeled is version 206, where the slab tear is now an incision into the top of the slab. The datum elevation for this model is 4.45 km. The highest point of surface topography produced from this medium slab tear is 5.66 km, and is located 992 km away from the trench at data collection, and 1037 km away from the initial trench location (Figures 4.7, 4.9, Table 4.1). In version 206 the trench migrated 45 km, which occurred from the initial timestep until 0.9 Myrs, and maintaining the same parameters as in version 153, is equivalent to 13.5 Myrs real-world time. Average trench migration velocity for this model is calculated to be 3.3 km/Myr (Figures 4.7, 4.9, Table 4.1).

Similar to version 153, the flow monitoring tracers show flow is attempting to penetrate the subducting lithosphere from both the top and bottom weak zones. This time the incision from the top appears to be too substantial for the slab to remain intact, thus breakoff occurs, with flow attempting to pass through the slab before and during the slab breakoff event. Once breakoff occurs, the tracers disperse due to the force of the breakoff. During the initial sinking of the slab, the average non-dimensional slab velocity (Figure 4.11) is calculated to be 18.92 (Figure 4.11, Table 4.2). There is a velocity anomaly present just beneath the mantle wedge, where the maximum non-dimensional flow velocity is 22.24, located at a depth of 169 kilometers beneath the surface and about 210 kilometers left of the trench (980 kilometers from the left wall) corresponding to the location of the slab gap. The amplitude of this non-dimensional velocity anomaly is approximately 11.31 (Figure 4.11, Table 4.2).
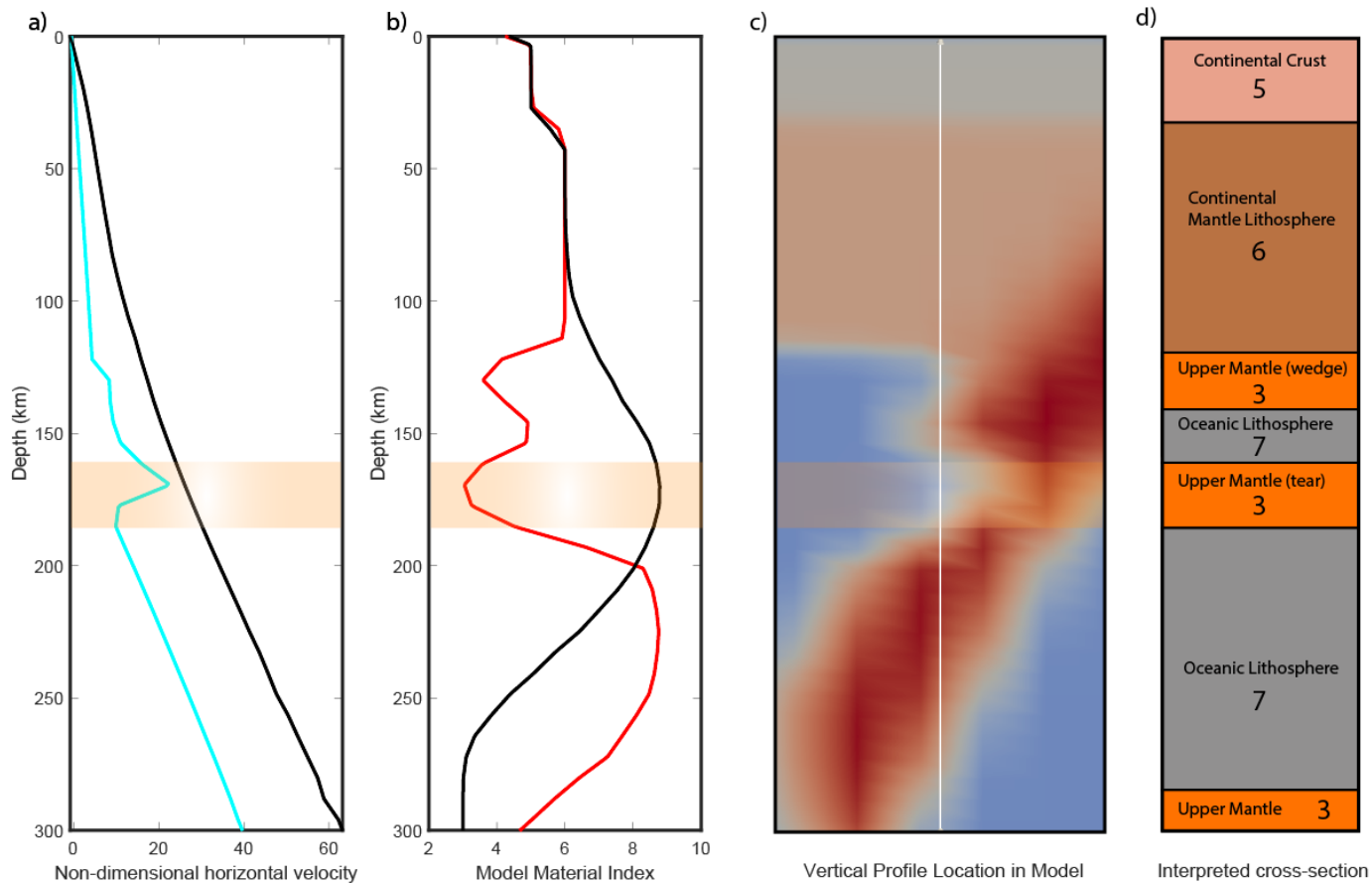
Figure 4.11 Velocity data for model version 206 involving a medium-sized tear to the top of the subducting lithosphere. A shows the velocity data in the horizontal component, with the black line indicating the reference case and the cyan line indicating velocity in version 206. B shows the corresponding material field at the same depths. C shows a snapshot of the location of the profile where the data in A and B were taken. D, a representation of the interpreted cross section of the model materials present through the profile.

4.1.4   Large slab tear models

The following subsection presents the findings of two models in which a large

tear is added to the subducting lithosphere. In version 154, the large tear is added to the

bottom of the slab, whereas in version 208 the large tear is added to the top of the slab.

Areas of missing lithosphere for the large tears are 1500 km^2 and 1450 km^2, respectively.

The results of each model are presented beginning with surface topography data located

in Table 4.1 with relevant observations and concluding with the velocity data further

presented in Table 4.2.

4.1.4.1   Model version 154

This model (version 154) features a large incision into the subducting lithosphere

located along the base of the slab. The topographical high for this large tear model is 5.60

km, which is located 991 km from the trench at the time of data collection and 1036 km

from the trench at the time of model initialization (Figures 4.4, 4.12, Table 4.1). The

trench migrated 45 km from the original position, occurring over a model time of 0.9

Myrs, a real-world equivalent of 13.5 Myrs. From these results, average trench migration

velocity is calculated to be 3.3 km/Myr (Table 4.1). The datum elevation used in model

version 154 is 4.65 km.

In version 154, the slab breaks off due to substantial resistance in the subduction

hinge, resulting in some observed attempted flow through the region where the slab tear

was present. Similarly to the medium top tear model (version 153), the slab breakoff

caused tracers to disperse on both sides of the subducting slab. The magnitude of the
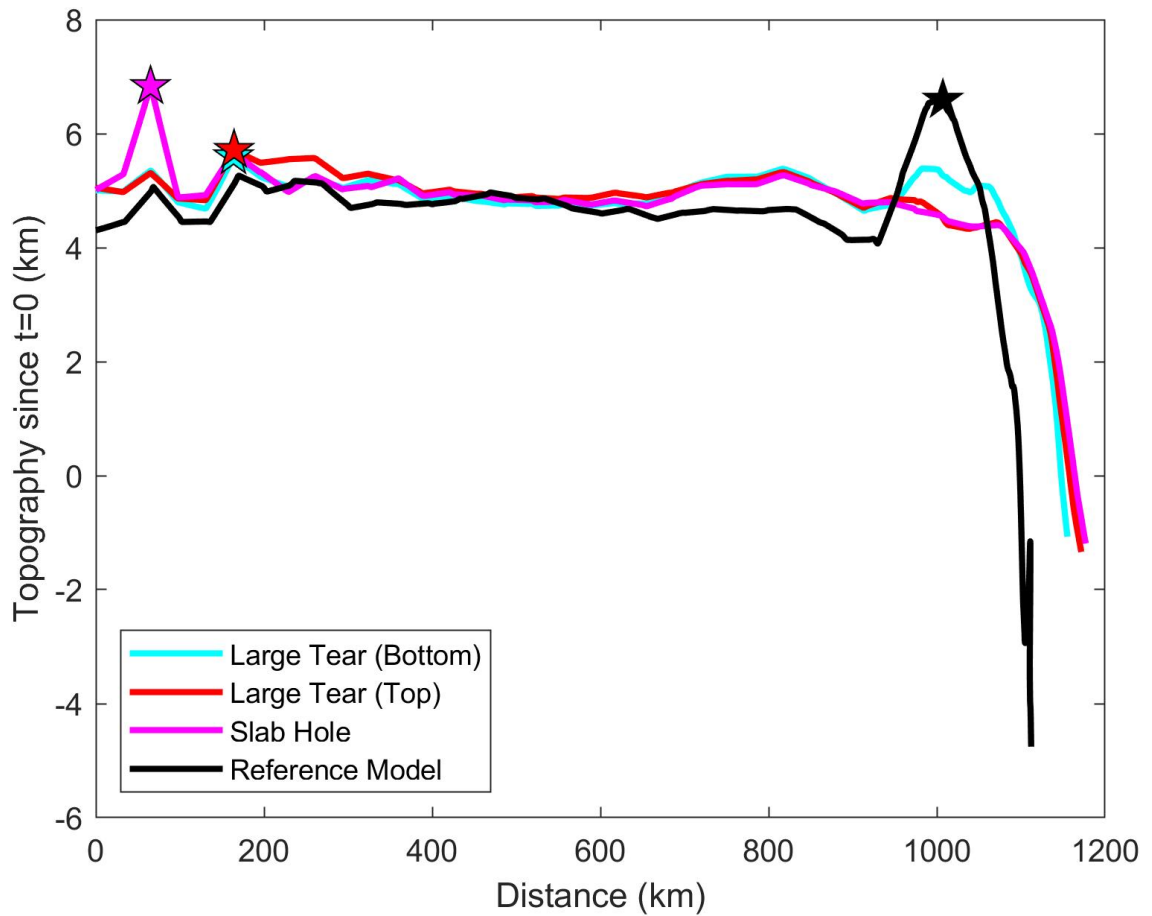
Figure 4.12 Surface topography data from four subduction models presented that encompass all large slab tears introduced to the subducting slab (v154, v208), compared to the reference model (v171) and slab hole model (v155). Topography captured at 13.5 Myrs and 10.5 Myrs, respectively, for the large tears visualized.

maximum non-dimensional flow velocity anomaly in version 154 is 3.04, however this

velocity is in the leftward direction, thus it is negative (Figure 4.13, Table 4.2) meaning

the flow is moving primarily through the slab from underneath towards the mantle wedge

and top of the slab. The depth of this anomaly is 162 kilometers, located approximately

140 kilometers leftward of the trench at data acquisition and 1050 kilometers left of the

continental extent to the left wall of the model domain. The material index corresponding

to this anomaly is 3.53 meaning it was also mostly upper mantle material, and the non-

dimensional amplitude of the velocity anomaly is 1.34 (Figure 4.13, Table 4.2).

4.1.4.2   Model version 208

The second large tear model analyzed in this work is model version 208, in which

there is a large incision into the top of the subducting lithosphere. The elevation datum

used for model version 208 is 4.33 km. The highest point of elevation in this model is

5.71 km and is located 1007 km from the trench at data collection, and a total of 1036 km

from the trench starting position (Figures 4.7, 4.12, Table 4.1). The trench advanced 29

km over a model time of 0.7 Myr, resulting in an average trench migration velocity of 2.8

km/Myr (Table 4.1).

Model version 208 breaks off soon after the initiation of subduction, occurring as

resistances in the trench are once again too much for the slab to remain intact. The flow

tracers reflect dispersion of the velocity field in this region when breakoff occurs. The

average velocity of the slab is not calculated for this tear because too much lithosphere is

missing to give an accurate average in this profile. Quantification of the flow reveals that

73
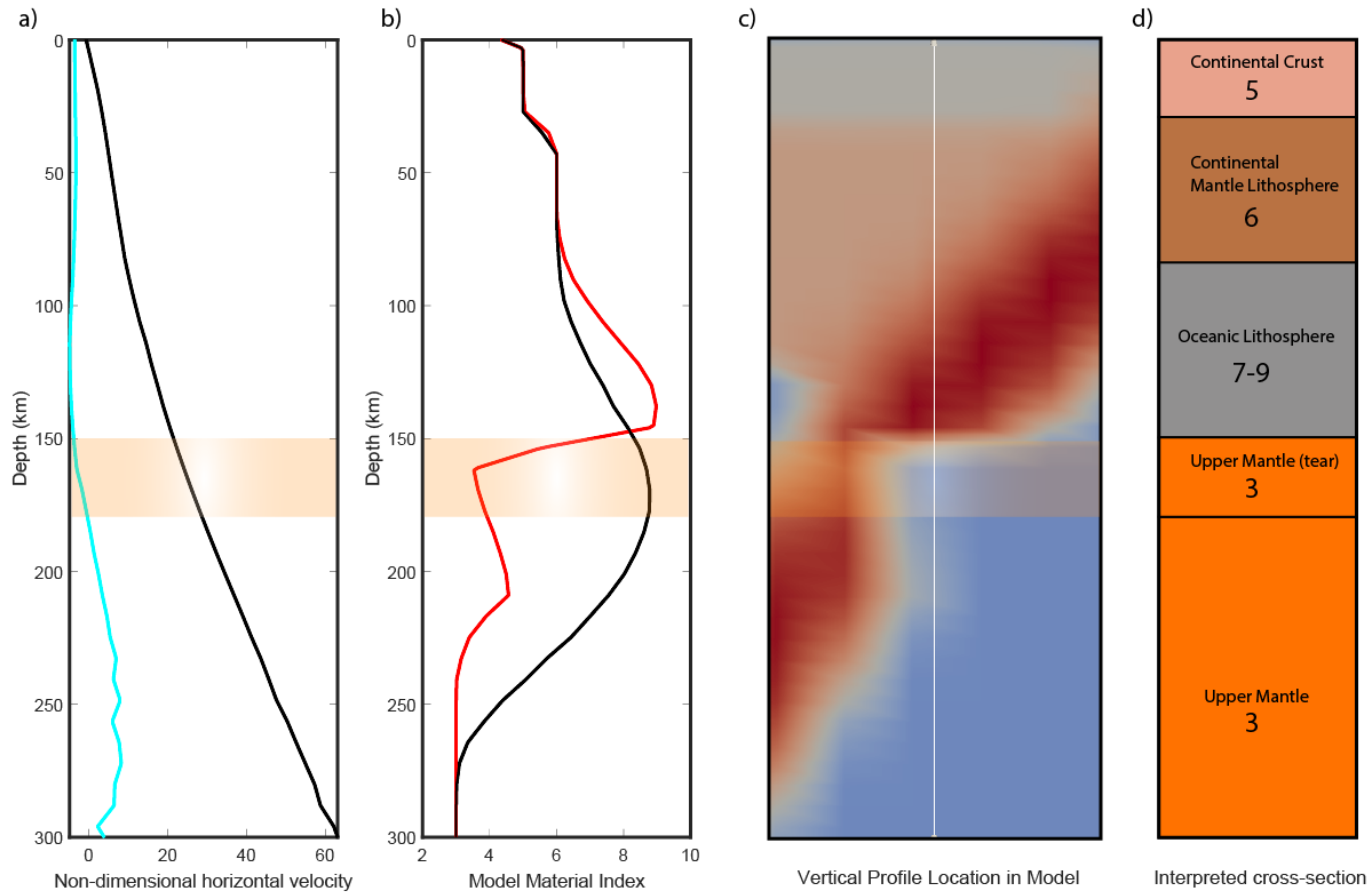
Figure 4.13 Velocity data for model version 154, with a large tear to the base of the lithosphere. A shows the velocity data for the horizontal component, with the black line indicating the reference case and the cyan line indicating velocity in version 154. B shows the corresponding material field at the same depths. C shows a snapshot of the location of the profile where the data in A and B were taken. D, a representation of the interpreted cross section of the model materials present through the profile.

the maximum non-dimensional flow velocity into the torn region of the slab at 3.0 Myr is

19.79 (Figure 4.14, Table 4.2), which occurs at a depth of 177 kilometers, approximately

208 kilometers left of the trench (982 kilometers right of the left wall of the model

domain). Additionally, the non-dimensional amplitude calculated for the peak of the

velocity anomaly is 10.52 (Figure 4.14, Table 4.2).

4.1.5   Lithospheric gap/hole model (v155)

The model of a lithospheric gap in two dimensions consists of a slab that appears

to have undergone slab detachment at model initiation (Figures 3.2, 4.15). The area of

missing lithosphere for the lithospheric gap model is approximately 3000 km^2. This has

some obvious limitations but allows us to explore the flow when no piece of slab is present

at the same depths as the other slab tears. The highest topographical point in the lithospheric

gap model is 6.83 km and is located 1112 km from the trench during data collection and

1135 km from the initial position of the trench, implying the trench migrated 23 km

between these times (Figure 4.5, Table 4.1). The trench migrated this distance over a model

time of 0.8 Myr, a real-world equivalent time of 12 Myr, thus the average rate of trench

migration for model version 155 is approximately 1.9 km/Myr (Figure 4.5, Table 4.1). The

datum elevation used for comparison for this model is 4.72 km.

Similar to other models that exhibit breakoff after subduction begins (versions

153, 154, 206, 208), the initial breakoff in version 155 provides the same result as the

others in terms of the effects on the flow-monitoring tracer particles. The maximum non-

dimensional velocity interpreted as flow through the gap is observed to be -14.09, located

at a depth of 201 kilometers (Figure 4.15, Table 4.2) which means flow was moving from
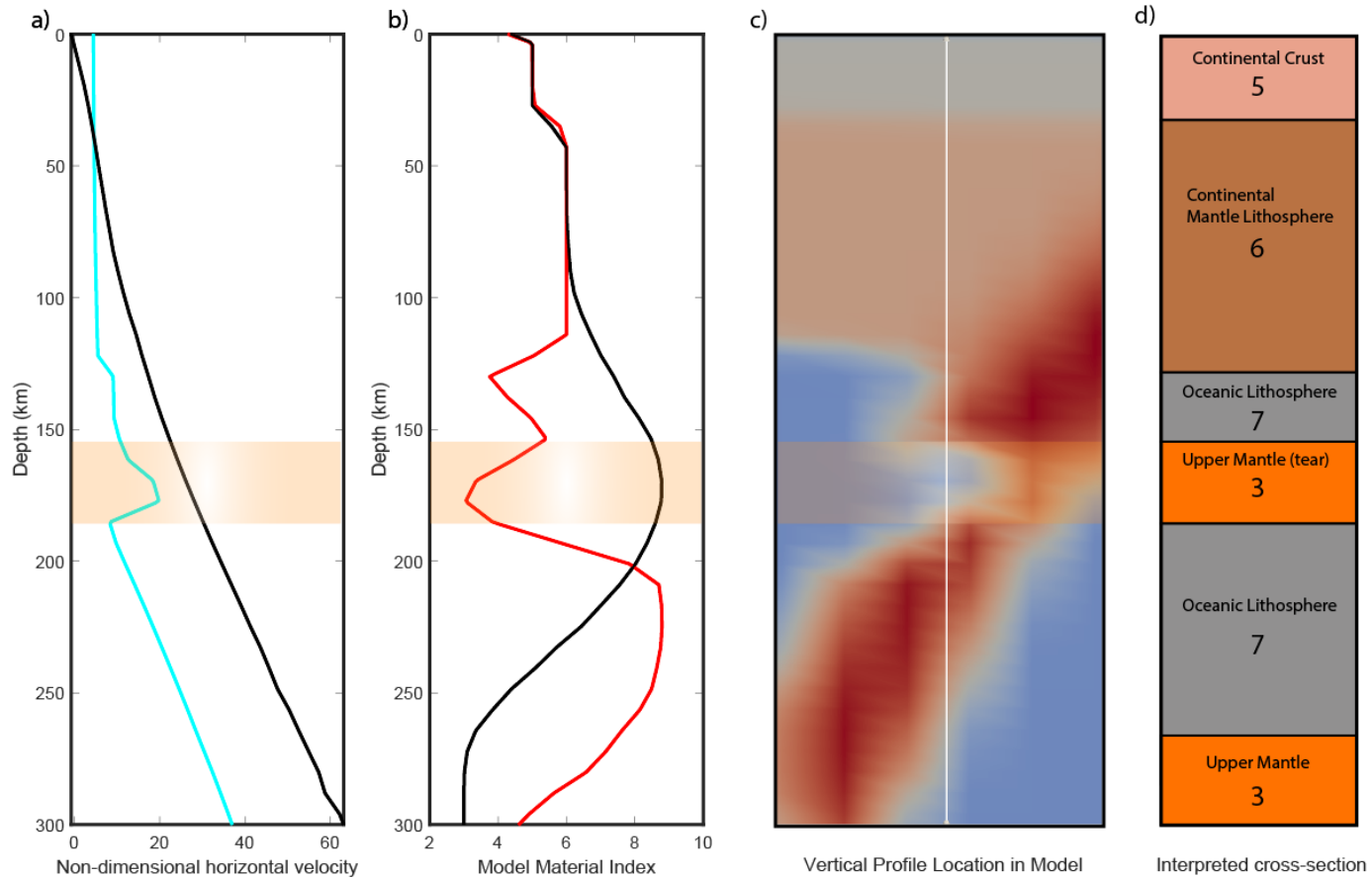
Figure 4.14 Velocity data for model version 208 involving a large-sized tear to the top of the subducting lithosphere. A shows the velocity data in the horizontal component, with the black line indicating the reference case and the cyan line indicating velocity in version 208. B shows the corresponding material field at the same depths. C shows a snapshot of the location of the profile where the data in A and B were taken. D, a representation of the interpreted cross section of the model materials present through the profile.
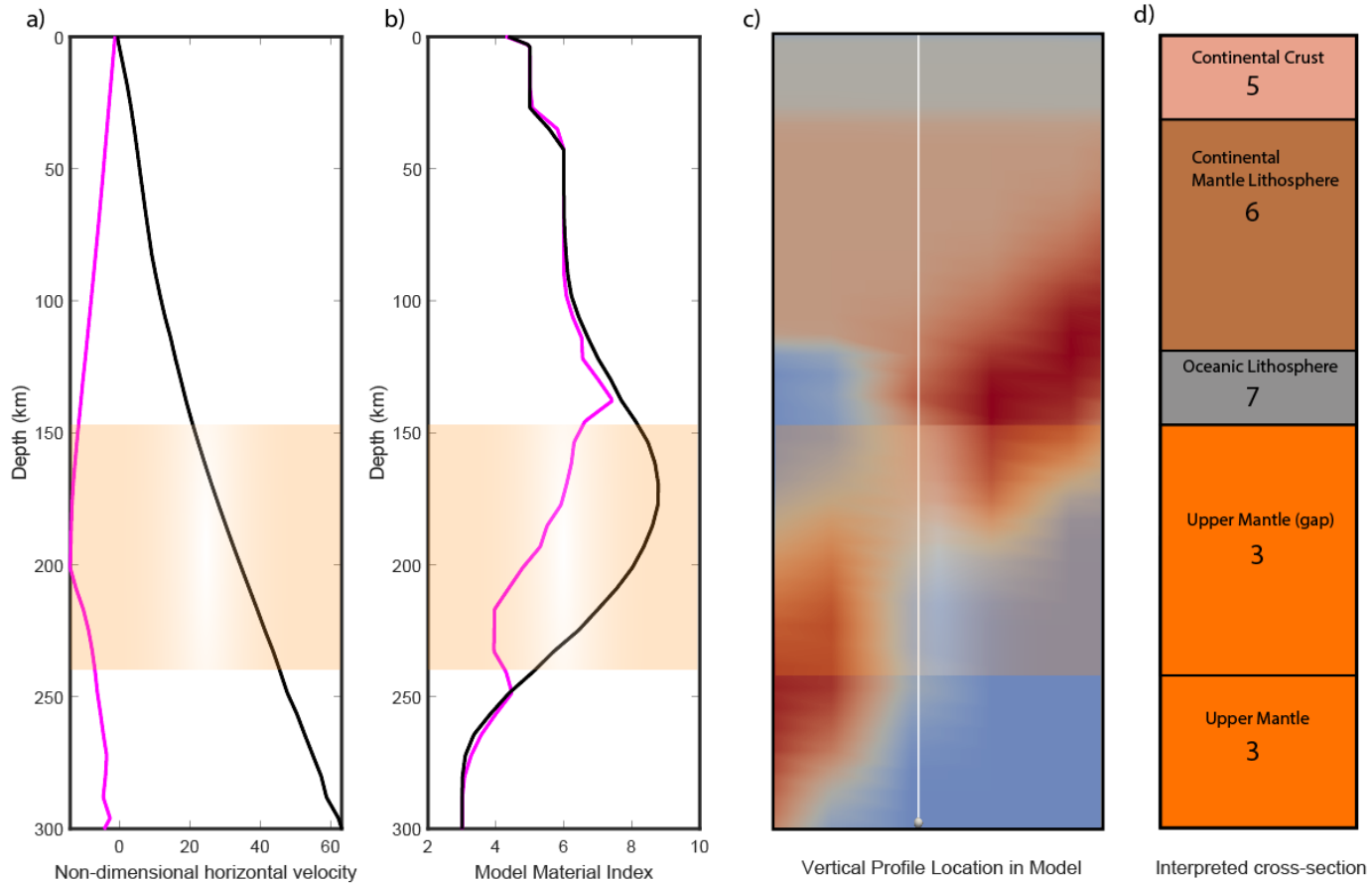
Figure 4.15 Velocity data for model version 155, with a complete lithospheric gap. A shows the velocity data in the horizontal component, with the black line indicating the reference case and the magenta line indicating velocity in version 155. B shows the corresponding material field at the same depths. C shows a snapshot of the location of the profile where the data in A and B were taken. D, a representation of the interpreted cross section of the model materials present through the profile.

the underside to topside of the slab. The corresponding material index to this data point is

4.80 meaning the max velocity is representing upper mantle material flowing through the

slab gap, and the non-dimensional amplitude of the velocity anomaly is estimated to be

2.39 (Figure 4.15, Table 4.2).

4.1.6   Flat slab subduction models (v190, v194, and v197)

Results for flat slabs are presented beginning with the flat slab reference model

case and proceed to present the results for two other cases in which there is missing

lithosphere. The other two cases in which results are presented here are that of a flat slab

containing a lithospheric gap (version 194) and a flat slab containing a large tear into the

top of the flat portion (version 197). Similar to the normal subduction cases, the results

are presented such that the surface topography results are outlined first for each model,

followed by the velocity data results.

4.1.6.1   Model version 190

Model version 190 is the reference model for flat slabs, thus there is no introduction

of slab tears or holes in this version, and this model is most comparable to the reference

case (version 171) of the normal subduction models. The datum elevation used for this

model is 2.99 km, which represents a topographical low in the back-arc just before the

orogen. The maximum topography generated in this model is 6.96 kilometers, which occurs

at a model location of 951 kilometers, which is 128 kilometers from the trench upon data

acquisition and 249 kilometers away from the trench location at model initiation (Figure

4.16, Table 4.1). Using these values, a total trench migration for the flat slab reference model is calculated to be 121 kilometers. Data is gathered over the course of 0.8 Myrs model time, a real-world equivalent of 12 Myrs. The average trench migration rate was calculated for version 190 to be 10.1km/Myr during this simulation (Figure 4.16, Table 4.1).

Values for flow are not obtained for the reference model, as no anomaly is present, however the average non-dimensional horizontal slab velocity is 0.72 (Figure 4.17, Table 4.2). Values for the velocity field in the reference flat slab case at the particular time interval (0.2 Myrs model time / 3.0 Myrs real time) tend to stay low for the entire upper 300 km of the model domain that is sampled. The velocity slowly increases from the bottom of the continental mantle lithosphere until roughly 300 kilometers depth (Figure 4.17).

4.1.6.2 Model version 194

Model version 194 consisted of a lithospheric gap in the flat portion of the subducting slab approximately 40 km in width and located nearly 300 km from the location of the trench at model initiation. Model version 194 is comparable to the lithospheric gap model (version 155) in the normal subduction cases. The datum elevation used for model version 194 is 3.97 km. The maximum topography in this version is 7.02 kilometers, located 127 kilometers from the trench, and 239 kilometers from the trench at model initiation (Figure 4.16, Table 4.1). From this, the amount of trench advance is calculated to be 112 kilometers, which occurred over a time span of 1.0 Myr model time (15.0 Myrs real-world equivalent), providing an average trench advance rate of 7.5 km/Myr (Figure 4.16, Table 4.1).
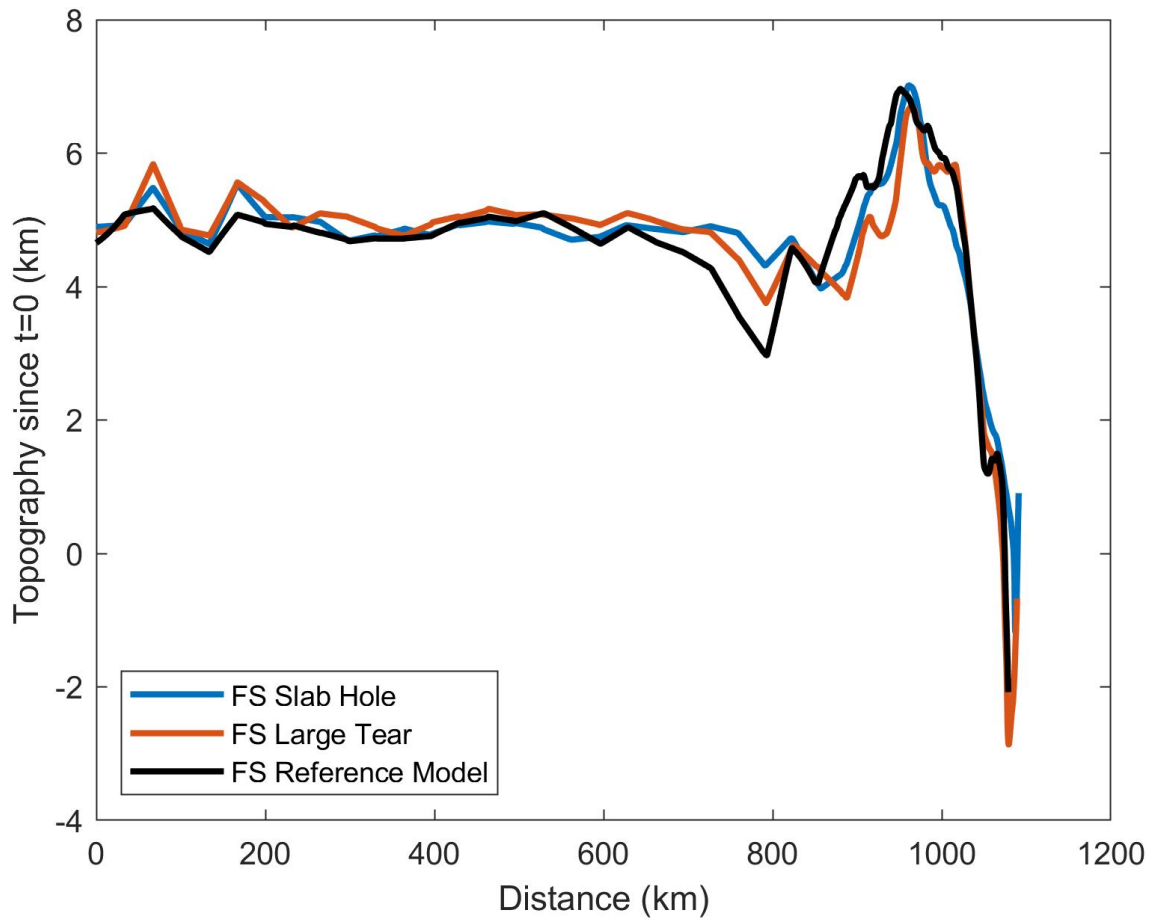
Figure 4.16 Surface topography of three subduction models presented that encompass the flat slab tear and hole introduced to the subducting slab (v194, v197), compared to the flat slab reference model (v190). Topography captured at 15 Myrs and 13.5 Myrs, respectively, for the flat slab tear and hole visualized, and the reference model topography was captured at 12 Myrs.
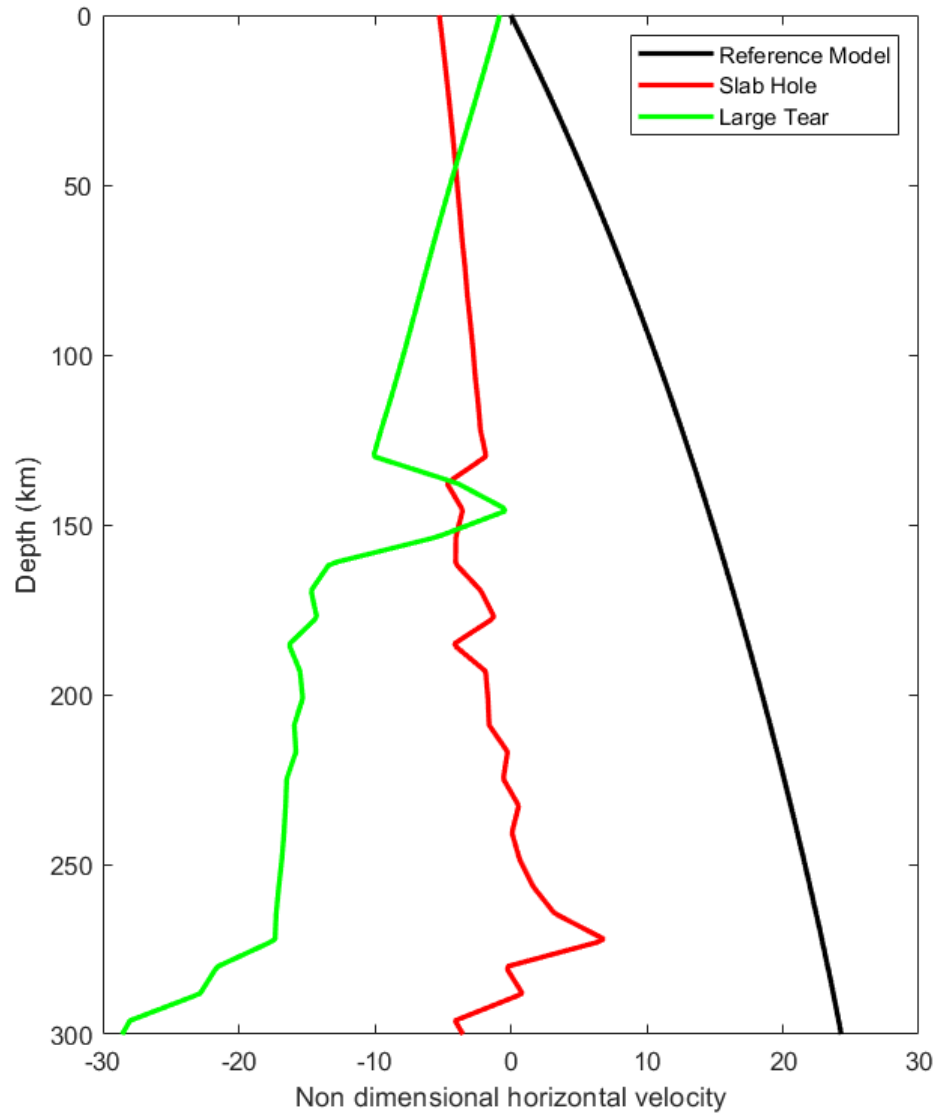
Figure 4.17 Velocity profiles of three subducting flat slabs acquired at a model time of 0.2 Myrs (real-world equivalent of 3.0 Myrs) from the surface to 300 kilometers depth. Depicted are model versions 190, 194, and 197, the reference model, lithospheric gap, and large slab tear, respectively. Negative velocities correspond to movement of particles leftward in the model domain, while positive velocities correspond to rightward motion of particles.

The maximum non-dimensional velocity has a magnitude of 19.49 in the horizontal direction and occurs at a depth of 169 kilometers (Figure 4.17, Table 4.2). The corresponding averaged material index at this depth is 4.51 meaning we are measuring the upper mantle flow velocity. The non-dimensional amplitude of the velocity anomaly is 1.21. Average slab velocity, as with the normal slab cases, was not determined for version 194, as this still would include effects of the lithospheric gap if it were calculated. The velocity profile indicates the horizontal velocity field is more highly perturbed than the reference model case, and shows minor varying velocities through the slab hole, followed by a much larger anomaly just beneath the slab at 280 kilometers depth (Figure 4.17, Table 4.2). The velocity profile of version 194 is far offset from the other flat slab model versions (both reference case and large tear case).

4.1.6.3   Model version 197

This model version 197 consisted of a large tear in the lithosphere of the flat portion of the subducting slab approximately 50 km in width, with an additional 60 km thickness cut vertically into the slab on the top/bottom. The datum elevation used for this version is 3.75 kilometers, a topographical low located in the back arc of the subduction zone. The maximum topography observed is 6.69 kilometers, which occurs at 965 kilometers distance, which is located 114 kilometers from the trench at the time of data collection (Figure 4.16, Table 4.1). The trench migrated 121 kilometers during the simulation, meaning that the trench was 235 kilometers away from the maximum topography location at model initiation. The trench advance of 121 kilometers occurred over 0.9 Myrs model

time (13.5 Myrs actual), which gives an estimated average trench migration rate of 9.0 km/Myr (Figure 4.16, Table 4.1).

Flow field results indicate a maximum non-dimensional velocity in the region of the slab tear of 2.71, which occurs at a depth of 193 kilometers (Figure 4.17, Table 4.2). The material index value corresponding to this anomaly is 4.51meaning this measures upper mantle flow near the slab tear/gap. The non-dimensional velocity anomaly amplitude is 0.46 (Figure 4.17, Table 4.2). The average slab velocity was not calculated for this version, because the tear is significant enough to reduce confidence in any kind of slab velocity measurement. As in the slab hole version (194), there are perturbations in the flow field primarily beginning just above the slab tear. The velocity anomaly that is likely pertinent to flow into the mantle wedge is present beneath the slab and near the tear as in the slab gap model (version 194) with minor velocity changes within the slab and gap. The overall velocity near the slab tear is not offset substantially from the reference model.

4.1.7   Maximum orogenic topography versus missing lithosphere

Focusing on the normal subduction cases, we calculated the least square solution between the maximum orogenic topography and the amount of missing lithosphere in our models. Figure 4.18 shows a plot of missing lithosphere versus maximum topography for all bottom tear cases. The data is then compared to the predicted data from the least squares solution to see if a relationship exists. For the bottom tear models (versions 152, 153, and 154), the least squares solution predicts a linear trend fits the observations of maximum orogenic topography (Figure 4.18). The R^2 value calculated as an estimate of the predicted
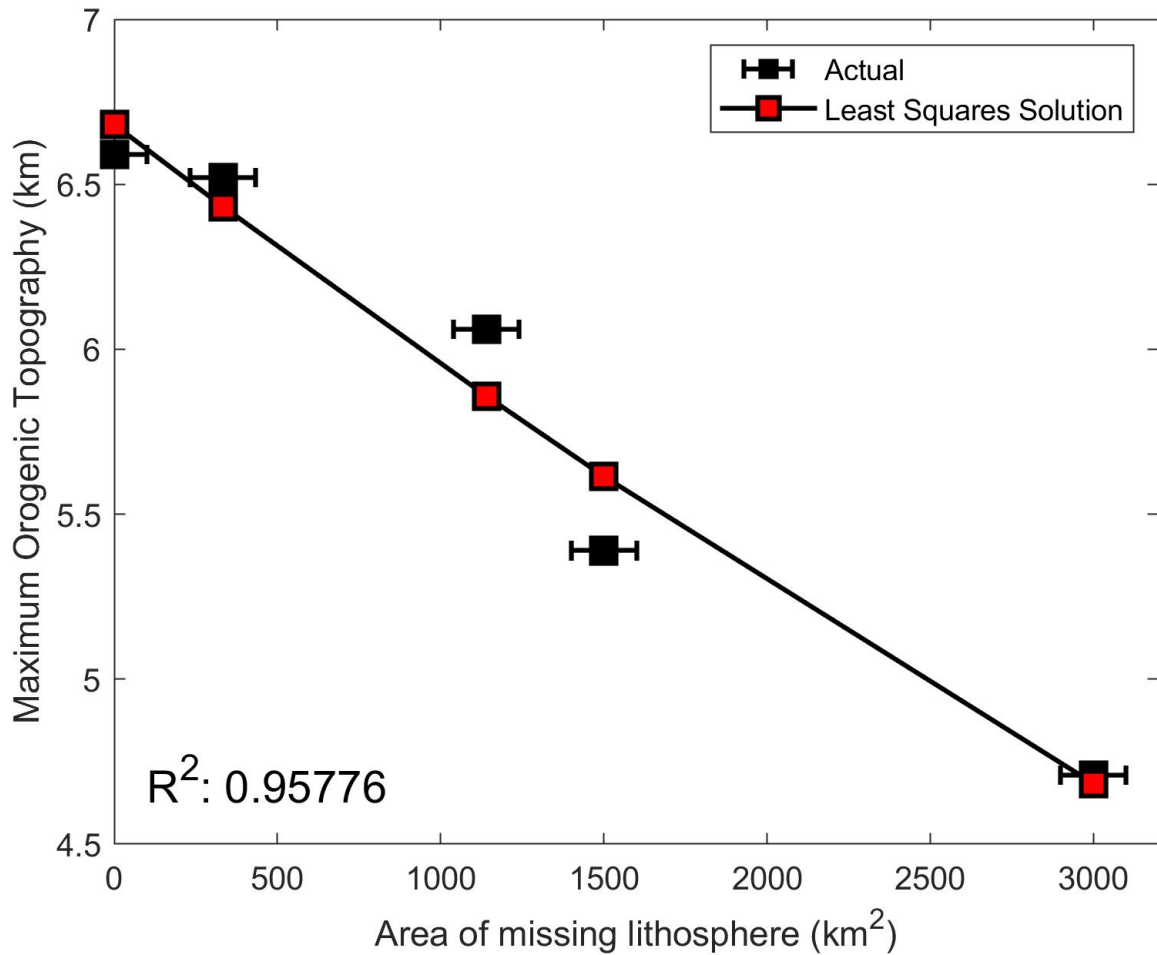
Figure 4.18 Analysis of surface topography trends in two-dimensional tears to the bottom of the subducting slab nose using a least squares solution plotted alongside data points of area of the slab tears/hole versus the amount of topography produced at the highest point. The least squares solution is indicated by the solid black line where datapoints are interpolated for a given amount of missing lithosphere to produce a predicted amount of surface topography. The R-squared estimate is located in the bottom left corner to give an estimation of accuracy of predicted data points by the least squares solution.

data fit is 0.9578 (Figure 4.18). The predicted maximum topography values for the bottom tears were 6.68 km for the reference model (v171), 6.43 km for the small bottom slab tear model (v152), 5.86 km for the medium bottom slab tear model (v153), 5.62 km for the large bottom slab tear model (v154), and 4.68 km for the slab hole (v155) (Figure 4.18).

Figure 4.19 shows the maximum topography versus missing lithosphere for models with tears on the top of the slab. For top slab tear versions (versions 205, 206, 208), the least squares solution predicts a semi-linear trend to fit the observations of maximum orogenic topography (Figure 4.19). The approximate R^2 value as an estimate of fit for the top tear least squares solution to the observed data points is 0.9625. The values predicted for maximum surface topography in the orogen are 6.75 km for the reference model (v171), 6.14 km for the small top tear model (v205), 5.28 km for the medium top tear model (v206), 4.90 km for the large top tear model (v108), and 4.69 km for the slab hole (v155) (Figure 4.19).
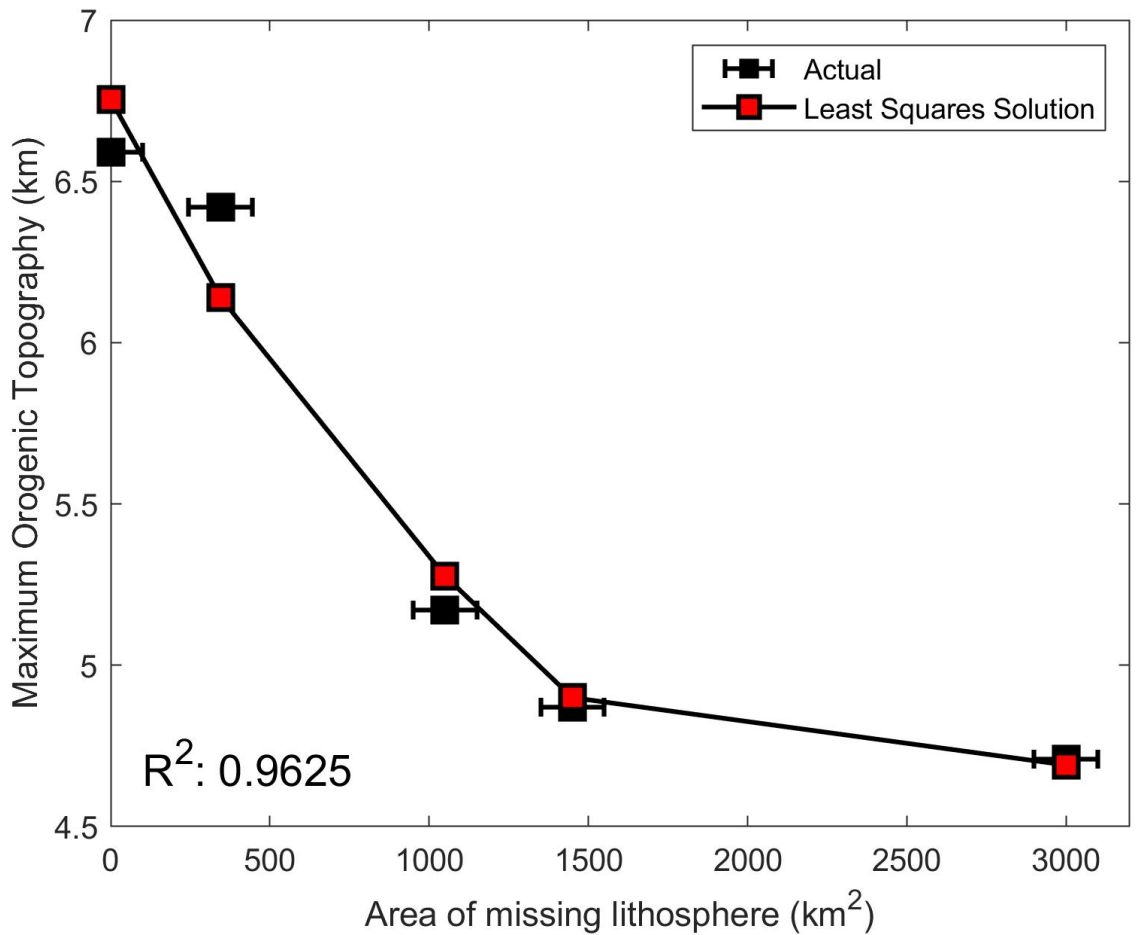
Figure 4.19 Analysis of surface topography trends in two-dimensional tears to the top of the subducting slab nose using a least squares solution plotted alongside data points of area of the slab tears/hole versus the amount of topography produced at the highest point. The least squares solution is indicated by the solid black line where datapoints are interpolated for a given amount of missing lithosphere to produce a predicted amount of surface topography. The R-squared estimate is located in the bottom left corner to give an estimation of accuracy of predicted data points by the least squares solution.

4.2   Three-dimensional Mechanical Models

Results for three-dimensional models are presented beginning with cases where the slab hole shape remains the same and centered around the same location but increases size with each successive model version. Next, we present the same results for a model where the centered location along the slab width changes. The results proceed to discuss a model (version 56) where the shape changes to a circle with similar size to the largest square tear (version 36). Next, the three-dimensional model results are presented for rectangular slit models. Finally, the results are presented for the double hole models in a longer subsection.

4.2.1   Reference Model (v47)

Model version 47 is used as the reference model for comparison to models that contain lithospheric gaps of varying size, shape, and location. This model has no missing lithosphere, the Lithospheric Volume Missing (LVM) (Table 3.4) is 0 km^3. The topographical peak within the orogen is 5.90 km high, located 65 kilometers from the end of the topographical profile (the trench), and located at a distance of 1788 kilometers along the width of the model domain (Figure 4.20). The curvature across the entire subduction arc in the reference model is approximately 0, with small variations across the width of the subduction arc not attributed to larger scale curvature (Table 4.3).

Table 4.3 Three-dimensional model surface topography and curvature results

Model	Single/Double	HS (km)	MT (km)	MTL [x,z] (km)	Lower Δx/Δz (km/km)	Upper Δx/Δz (km/km)	Max Δx	Sym? (Y/N)
v34	Single	N/A	5.92	[2484, 1788]	0.003	0.004	5	Y
v35	Single	N/A	6.01	[2482, 1788]	0.027	0.032	15	Y
v36	Single	N/A	6.09	[2477, 1787]	0.038	0.067	30	N
v37	Single	N/A	6.12	[2474, 1787]	0.062	0.063	45	N
v46	Single	N/A	6.21	[2476,1788]	0.049	0.047	33	Y
v47	Single	N/A	5.90	[2485,1788]	0	0	0	N/A
v56	Single	N/A	6.08	[2479,1788]	0.040	0.047	33	N
v57	Single	N/A	5.97	[2483,1788]	0.014	0.017	10	Y
v58	Single	N/A	6.07	[2480,1788]	0.039	0.038	20	Y
v63	Double	100	6.14	[2471,1787]	0.068	0.076	60	N
v61	Double	200	6.14	[2471,1787]	0.059	0.065	50	N
v62	Double	300	6.13	[2471,1787]	0.046	0.058	45	N
v59	Double	600	6.08	[2472,1787]	0.030	0.050	35	N
v64	Double	800	6.04	[2476,1969]	0.067	0.055	30	N
v65	Double	1000	6.04	[2478,1969]	0.045 / 0.055	0.050 / 0.027	30	Y / N
v60	Double	1200	6.03	[2478,1970]	0.065 / 0.068	0.085 / 0.039	25	N

HS is the amount of Hole Separation present between two slab holes if two are present, with single/double being the indicator of this. MT (Maximum Topography) represents the maximum topography produced in the orogen of the subduction model, while MTL (Maximum Topography Location) is the location of that data point in the model domain. Δx/Δz represents the curvature in the model, with Lower being the section of topography beneath the curvature apex and Upper being the section of topography above the apex. The maximum Δx is the offset of the apex of curvature and the original position of the orogen in regions unaffected by curvature. Sym indicates whether curvature in the orogen of a model was symmetrical about either side of the apex.
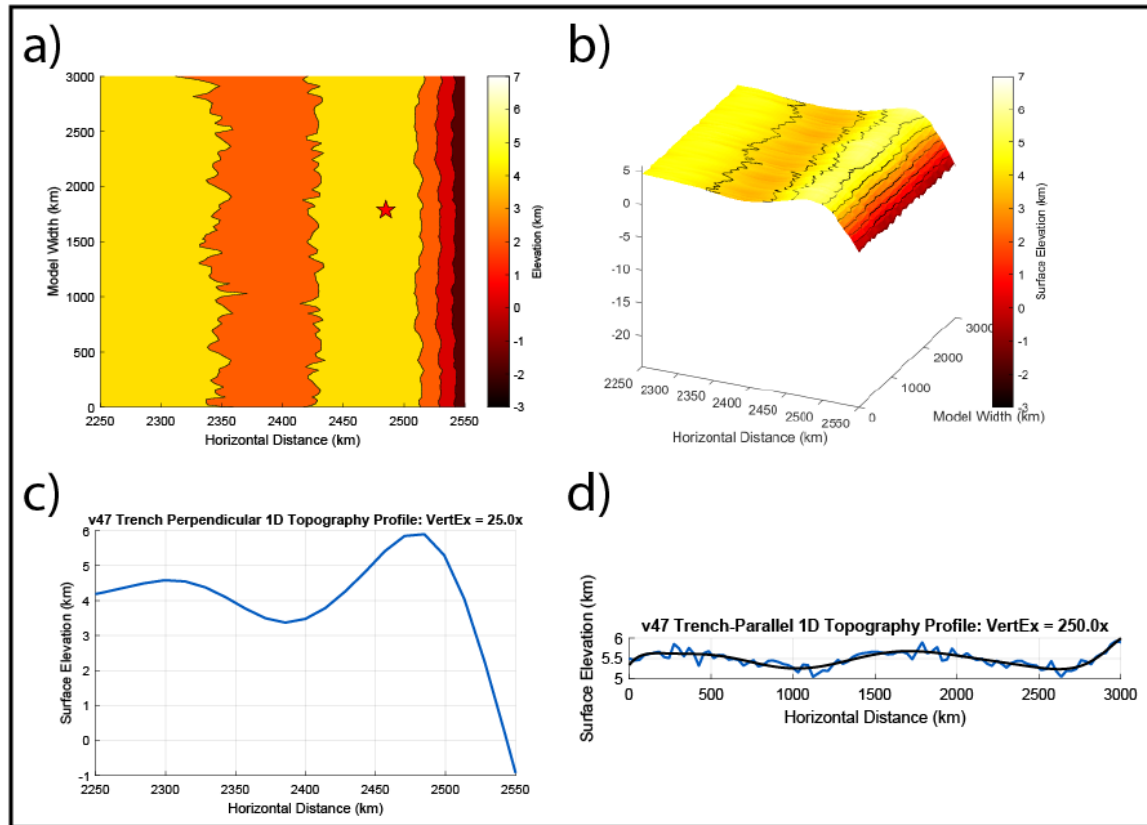
Figure 4.20 All data gathered for the three-dimensional reference subduction model version 47, including a) Map view/contour plot of the surface topography elevation approximately the first 300 kilometers landward from the trench, with a red star indicating the exact point of highest orogenic topography, b) Oblique view of a surface plot of the same topography in part a, c) 1-D transect of surface topography data along a line that passes through the star and travels exactly horizontal through the figure from 2250 kilometers to 2550 kilometers (perpendicular to the trench and orogen), d) 1-D transect of surface topography data along a line that passes through the star and travels exactly vertical through the figure from 0 kilometers width to 3000 kilometers width (parallel to the trench and orogen).

4.2.2 Centered square and rectangular models (v34-v37)

For each of these models, results are presented such that the surface topography results are discussed first, followed by the curvature of the orogen along the width of the model domain for models where the slab holes stay in the center of the model but increase in size from version 34 (smallest) to version 37 (largest) hole.

4.2.2.1 Model version 34

The small square hole model (v34) has approximately 250,000 km^3 of missing lithosphere, determined from the hole geometry of a 50 km long x 50 km wide x 100 km thick region (Table 3.4). The maximum topography in the orogen is located at 66 km left of the trench, and is 5.92 kilometers in elevation (Figures 4.21, 4.22, Table 4.3). This global maximum point of topography is located at z = 1788 kilometers (1788 kilometers from the front wall) (Figures 4.21-4.23).

Curvature within the lower section of the orogen (the side of the orogen closer to zero and below of the maximum point of curvature) is approximately 0.003 kilometers in slab length direction per kilometer change in slab width direction, thus for every kilometer travelled parallel to the orogen, the orogen shifts an average of 3 meters to the left/right (Figure 4.23, Table 4.3). On the upper side of the orogen (the section above the apex of subduction arc curvature), the curvature of the arc is approximately 0.004 kilometers per kilometer (Figure 4.23, Table 4.3). At the apex of the orogen curvature, the arc has shifted 5 kilometers from its original location at the upper and lower model domain edges, z = 0 kilometers, and z = 3000 kilometers, respectively. Because the
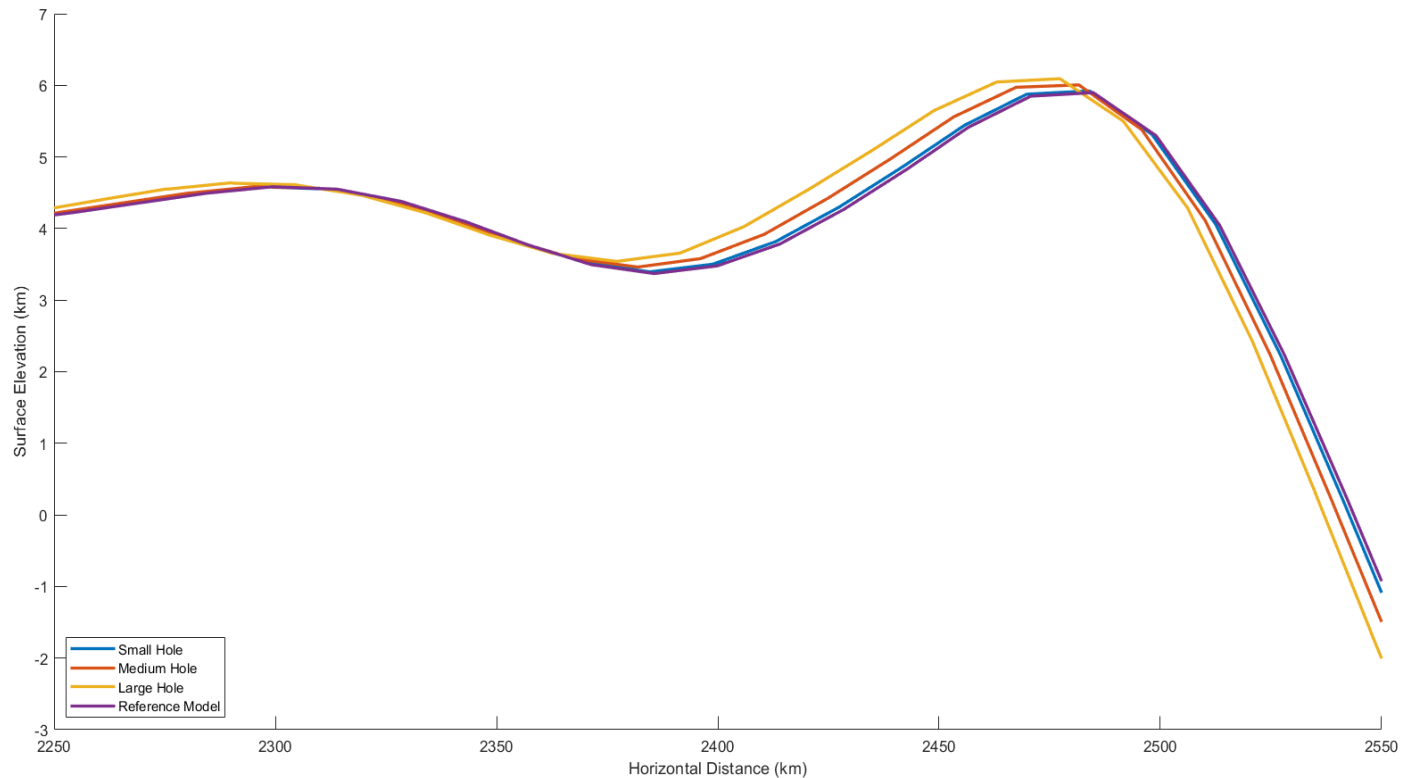
Figure 4.21 Plot of 1D surface topography profiles from four three-dimensional models where the trend between increasing hole size and maximum surface topography can be analyzed. The profile for each plot is taken through the point of maximum topography (represented by red stars in map view figures) in the increasing x-direction (perpendicular to the orogen and trench). Thus, the profiles go from 2250 kilometers at the far left to 2550 kilometers at the far right. The z coordinate for all profiles is either 1787 or 1788 kilometers depending on the occurrence of maximum topography in the model (see Table 7 as a reference). Model versions 34-36 are compared. The reference model (version 47) is also present as a comparison for a case with no hole.

Figure 4.22 Plot of 1D surface topography profiles from four three-dimensional models where the trend between increasing hole size and maximum surface topography can be analyzed. The profile for each plot is taken through the point of maximum topography (represented by red stars in map view figures) in the increasing z-direction (parallel to the orogen and trench). Thus, the profiles go from 0 kilometers at the front to 3000 kilometers at the back. The x coordinate for all profiles depends on where the maximum topography occurs (see Table 7 as a reference). Model versions 34-36 are compared. The reference model (version 47) is also present as a comparison for a case with no hole.

Figure 4.23 Comparison of the resulting surface topography in four three-dimensional subduction model versions where in a) version 47 (reference) is compared with b) version 34, in which a 50x50 kilometer square hole is introduced to the subducting lithosphere, c) version 35, in which a 100x100 kilometer square hole is introduced to the subducting lithosphere, d) version 36, in which a 150x150 kilometer square hole is introduced to the subducting lithosphere. Red stars represent the point of maximum observed surface topography in the orogen of a particular model. Black shapes help illustrate hole geometry used within each model.

curvature on the upper section and the curvature on the lower section of the arc are within

+/- 0.005 km/km of each other, we consider the curvature of the orogen to be

symmetrical (Table 4.3).

4.2.2.2   Model version 35

The medium square hole model (v35) has a region of missing lithosphere totaling

1,000,000 km^3, determined by the hole dimensionality of 100 kilometers width x 100

kilometers length x 100 kilometer slab thickness (Table 3.4). The point of maximum

topography in the orogen is at an elevation of 6.01 kilometers, located a distance 68

kilometers from the trench, and at z = 1788 kilometers along the subduction arc (Figures

4.21-4.23, 4.24, Table 4.3).

The curvature at the bottom of the model domain at z = 0 kilometers to z = 1090

kilometers is ~0 km/km. From z = 1090 kilometers to z = 1650 kilometers, the curvature

is 0.027 km/km as the orogen shifts to the left and reaches the curvature apex at z = 1650

kilometers (Figure 4.24, Table 4.3). From this point, the orogen retreats to the original

horizontal position with a curvature of 0.032 km/km from the apex at z = 1650 kilometers

to z = 2125 kilometers (Figure 4.24, Table 4.3). From this point to z = 3000 kilometers,

the curvature is ~ 0 km/km again. At the apex of arc curvature, the maximum amount the

orogen shifted leftward was 15 kilometers (Figure 4.24, Table 4.3). Because 0.027

km/km and 0.032 km/km are within the +/- 0.005 of one another, the arc that formed in

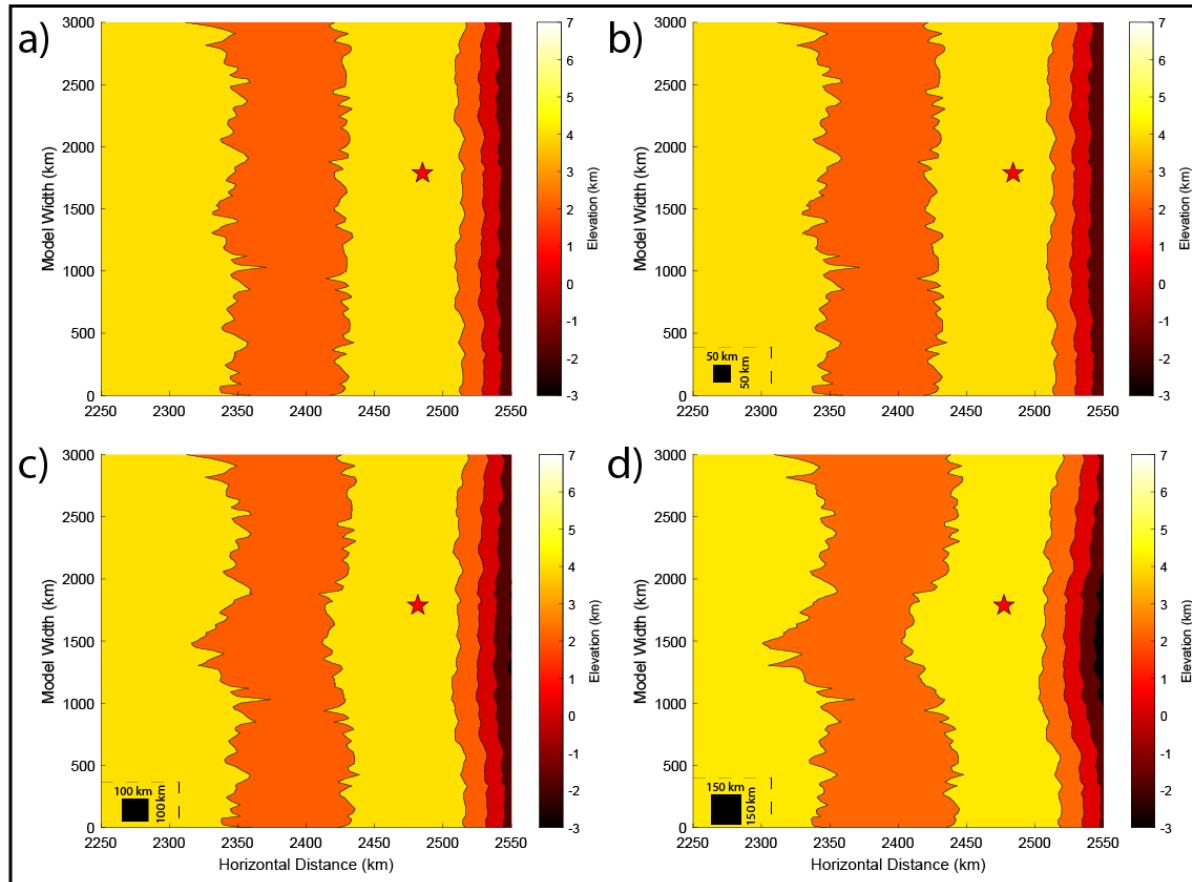this model is also considered symmetrical (Figure 4.24, Table 4.3).
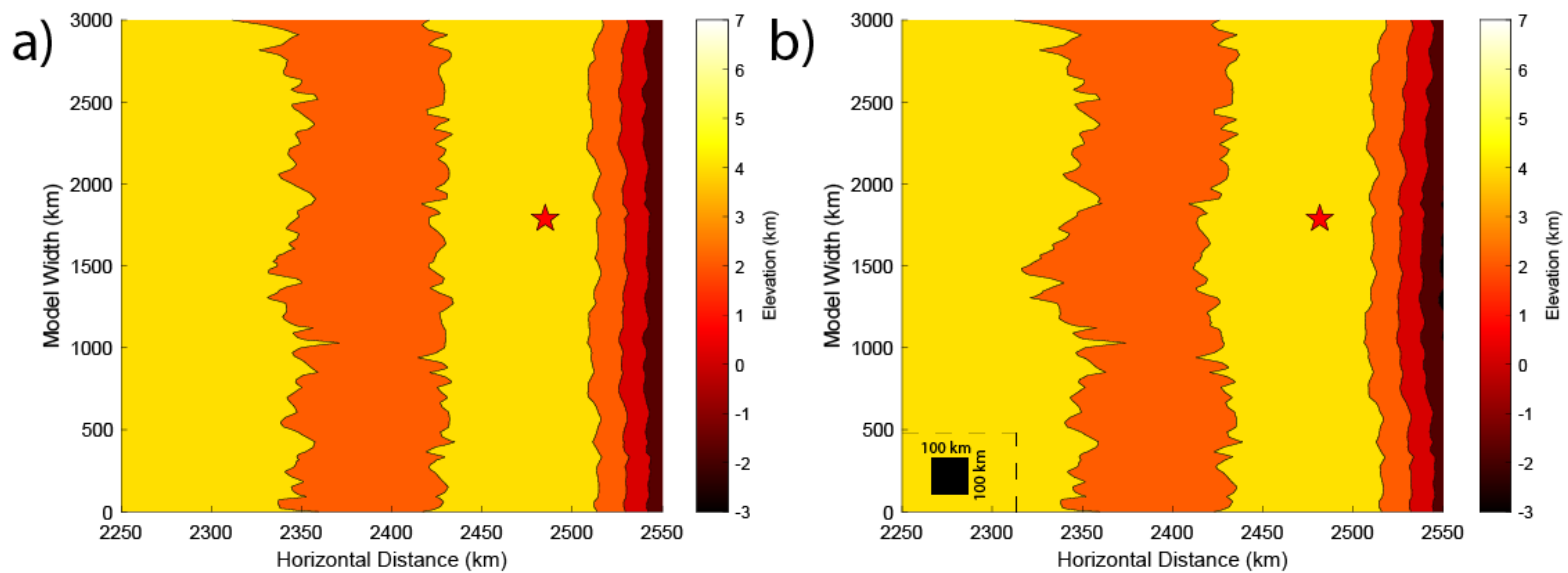
Figure 4.24 Comparison of the resulting surface topography in two three-dimensional subduction model versions where in a) version 47 is compared with b) version 35, which has a 100x100 kilometer square slab hole introduced to the subducting lithosphere. Stars are the areas of maximum topography within the orogen of the subduction zone. The shape in the bottom left corner of b represents the amounts of missing lithosphere from the slab hole.

4.2.2.3   Model version 36

The large square hole model (v36) centered within the central orogen has a total volume of missing lithosphere equivalent to 2,250,000 km^3 from the dimensionality of the hole of 150 kilometers in length x 150 kilometers in width x 100 kilometers in thickness (Table 3.4). Maximum topography within the orogen is at an elevation of 6.09 kilometers, located a distance of 73 kilometers leftward of the trench and at z = 1787 kilometers along the subduction arc (Figures 4.21-4.25, Table 3.4).

Curvature along the subduction arc is ~ 0 km/km from z = 0 kilometers to z = 825 kilometers. From z = 825 kilometers to z = 1620 kilometers, the curvature is approximated at 0.038 km/km. The apex of curvature in this arc is 30 kilometers leftward of the arc location at the z = 0 and z = 3000 kilometers where no curvature is present. The upper side of the orogen has an approximated curvature of 0.067 km/km from the apex location to z = 2070 kilometers (Figure 4.25, Table 4.3). From z = 2070 kilometers to the top of the model domain at z = 3000 kilometers, the arc curvature is ~ 0 km/km (Figure 4.25). Because the values of curvature for the upper side and lower side of the orogen are outside of +/- 0.005 of one another (0.038 & 0.067), the arc is considered asymmetrical (Table 4.3).

4.2.2.4   Model version 37

The slab hole in this model version (v37) is centered around the center of the subduction arc as in versions 34 through 36, but is elongated in the model width dimension and the volume of missing lithosphere in this version is calculated from a
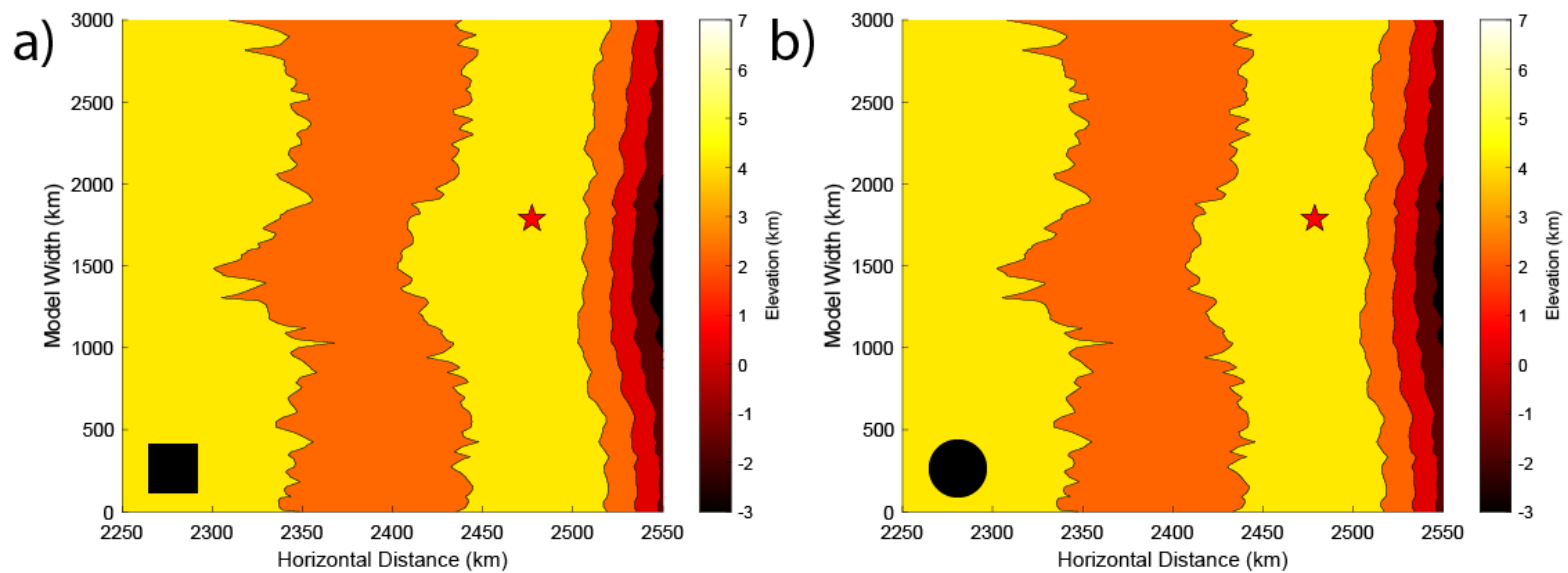
Figure 4.25 Comparison of the resulting surface topography in two three-dimensional model versions where in a) version 36, we use a square hole of 150x150 kilometers dimensionality and b) version 56, where we use a circular hole with a radius of 75 kilometers. The red star shows the location of maximum orogenic topography in both cases. The symbols in the bottom left re-iterate the shape of the slab hole used in each model.

dimensionality of 125 kilometers length x 250 kilometers width x 100 kilometer

lithospheric thickness (Table 3.4) for a volume of 3,125,000 km^3. The maximum

topography in the orogen is 6.12 kilometers in elevation, located at a distance of 76

kilometers leftwards of the trench and at z = 1787 kilometers along the subduction arc

(Figures 4.26-4.28, Table 4.3).

Curvature from z = 0 in the subduction arc to approximately z = 785 kilometers is

~ 0 km/km. From z = 785 kilometers to z = 1515 kilometers, the arc curvature is

approximated to be 0.062 km/km until the apex of arc curvature is reached (Table 4.3). At

this apex, the orogen is now located 45 kilometers left (landward) from the original

horizontal arc location. From z = 1515 kilometers to z = 2230 kilometers, the curvature in

the arc is approximately 0.063 km/km as the arc curves back towards its original horizontal

location. The curvature from z = 2230 kilometers heading towards z = 3000 kilometers is

~ 0 km/km along the orogen (Figure 4.26). The arc in this subduction model is symmetrical

due since there is only 0.001 km/km separation between the approximated curvatures on

either side of the subduction arc apex (Figure 4.26, Table 4.3).

4.2.3   Offset square hole model (v46)

The volume of missing lithosphere in the offset hole model (v46) is calculated from

the hole geometry of 150 kilometers in length x 150 kilometers in width x 100 kilometers

in slab thickness in a hole that is equal in volume to version 36 and offset from the center

of the origin and instead centered around z = 2000 kilometers (Figure 4.29, Table 3.4).

Maximum topography in this model is located at an elevation of 6.21 kilometers, a distance

Figure 4.26 All data gathered for the three-dimensional subduction model version 37 with a very large rectangular hole, including a) Map view/contour plot of the surface topography elevation approximately the first 300 kilometers landward from the trench, with a red star indicating the exact point of highest orogenic topography, b) Oblique view of a surface plot of the same topography in part a, c) 1-D transect of surface topography data along a line that passes through the star and travels exactly horizontal through the figure from 2250 kilometers to 2550 kilometers (perpendicular to the trench and orogen), d) 1-D transect of surface topography data along a line that passes through the star and travels exactly vertical through the figure from 0 kilometers width to 3000 kilometers width (parallel to the trench and orogen).

Figure 4.27 Plot of 1D surface topography profiles from 3 three-dimensional models where two models give very similar topographical signatures despite one having one very large hole introduced (Model version 37) to subducting lithosphere and the other case with two holes introduced (Model version 61). The profile for each plot is taken through the point of maximum topography (represented by red stars in map view figures) in the increasing x-direction (perpendicular to the orogen and trench). Thus, the profiles go from 2250 kilometers at the far left to 2550 kilometers at the far right. The z coordinate for all profiles is either 1787 or 1788 kilometers depending on the occurrence of maximum topography in the model (see Table 7 as a reference).

Figure 4.28 Plot of 1D surface topography profiles from 3 three-dimensional models where two models give very similar topographical signatures despite one having one very large hole introduced (Model version 37) to subducting lithosphere and the other case with two holes introduced (Model version 61). The profile for each plot is taken through the point of maximum topography (represented by red stars in map view figures) in the increasing z-direction (parallel to the orogen and trench). Thus, the profiles go from 0 kilometers at the front to 3000 kilometers at the back. The x coordinate for all profiles depends on where the maximum topography occurs (see Table 7 as a reference).
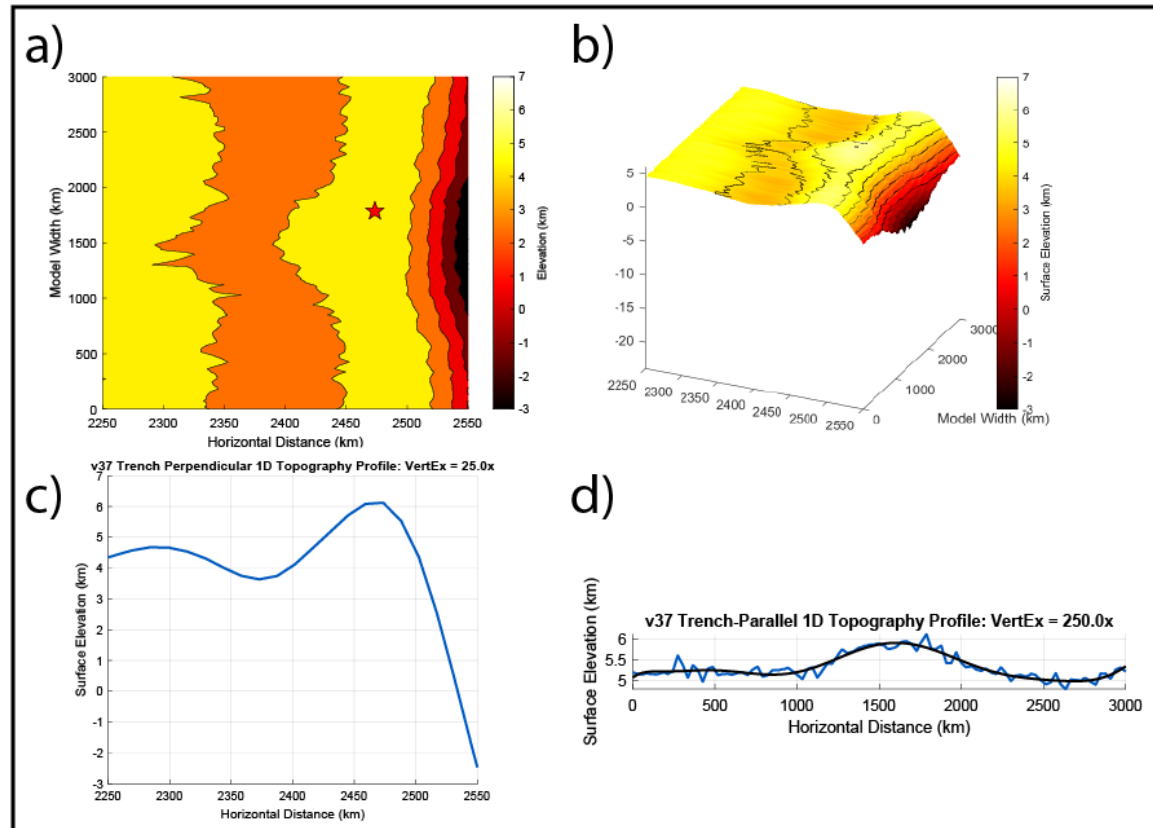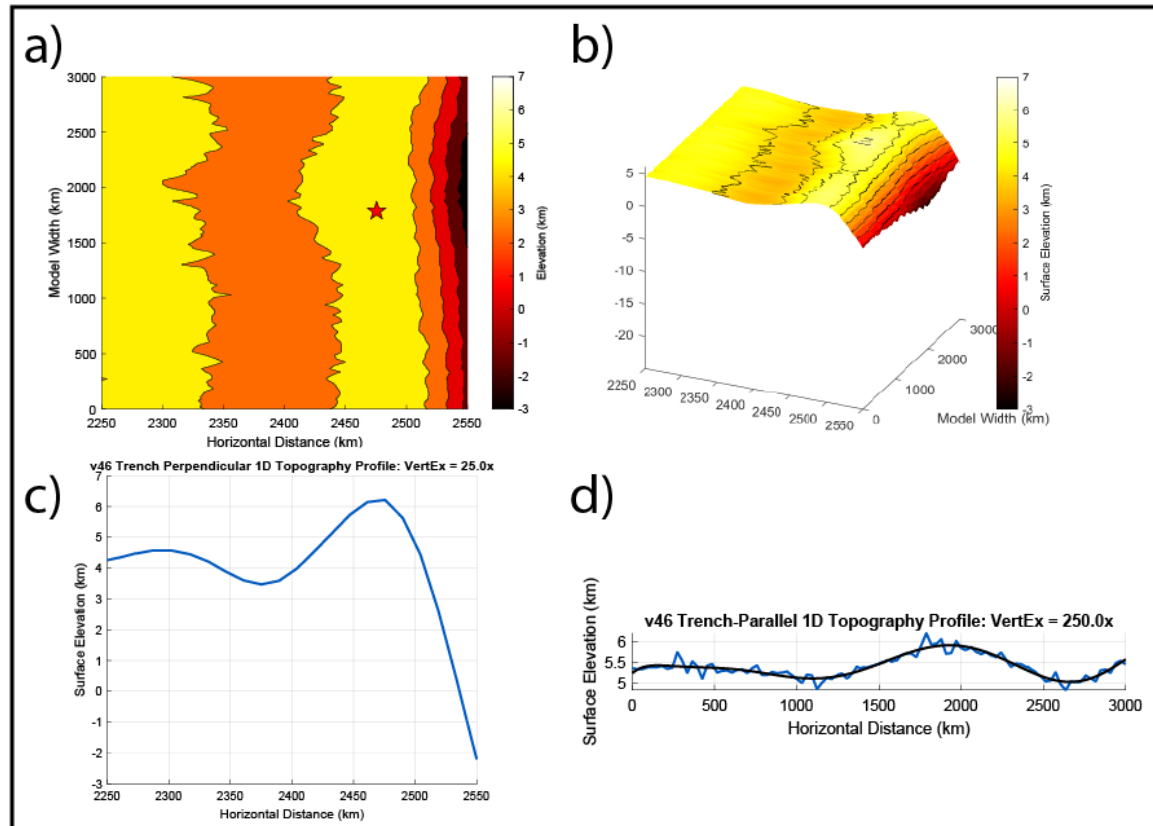
Figure 4.29 All data gathered for the three-dimensional subduction model version 46 with an offset square hole, including a) Map view/contour plot of the surface topography elevation approximately the first 300 kilometers landward from the trench, with a red star indicating the exact point of highest orogenic topography, b) Oblique view of a surface plot of the same topography in part a, c) 1-D transect of surface topography data along a line that passes through the star and travels exactly horizontal through the figure from 2250 kilometers to 2550 kilometers (perpendicular to the trench and orogen), d) 1-D transect of surface topography data along a line that passes through the star and travels exactly vertical through the figure from 0 kilometers width to 3000 kilometers width (parallel to the trench and orogen).
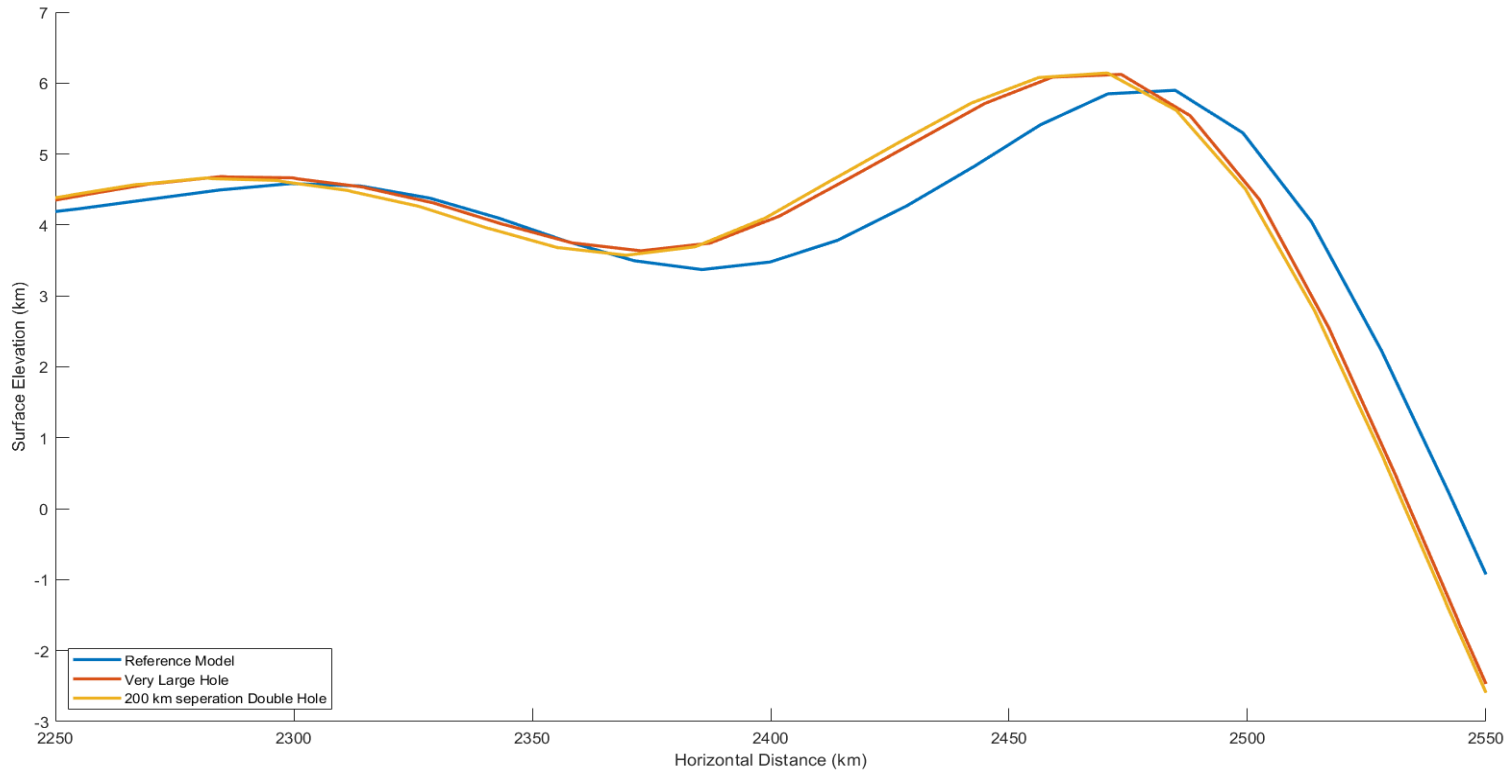
of 74 kilometers leftward/landward from the trench and at z = 1788 kilometers along the subduction arc (Figure 4.29, Table 4.3).

Curvature from the southern edge of the model domain to z = 1190 kilometers is ~ 0 km/km (Figure 4.29). Between z = 1190 kilometers and z = 1865 kilometers the curvature is approximately 0.049 km/km, with z = 1865 kilometers being the apex of the subduction arc (Figure 4.29, Table 4.3). The apex is located 33 kilometers further landward than the sections of the arc with no curvature (Figure 4.29, Table 4.3). From z = 1865 kilometers to z = 2560 kilometers, the curvature is approximately 0.047 km/km, and beyond z = 2560 kilometers up to z = 3000 kilometers, the curvature is ~ 0 km/km once again. The two sides of the apex in this subduction arc are within the bounds to be labeled symmetrical.

4.2.4   Circular hole model (v56)

The volume of missing lithosphere of the circular hole model (v56, cylindrical volume) is calculated from a hole with a radius of 75 kilometers and slab thickness of 100 km to be ~ 1,770,000 km^3 and is centered around the origin (Figure 4.30, Table 3.4). The location of maximum topography within the orogen is 71 kilometers leftward/landward from the trench location, at z = 1788 kilometers, and is at an elevation of 6.08 kilometers (Figure 4.30, Table 4.3).

In terms of subduction arc curvature, the first stretch of the orogen between z = 0 and z = 815 kilometers has a curvature of ~ 0 km/km. This curvature changes at z = 815 kilometers to z = 1630 kilometers to approximately 0.040 km/km until the apex of the
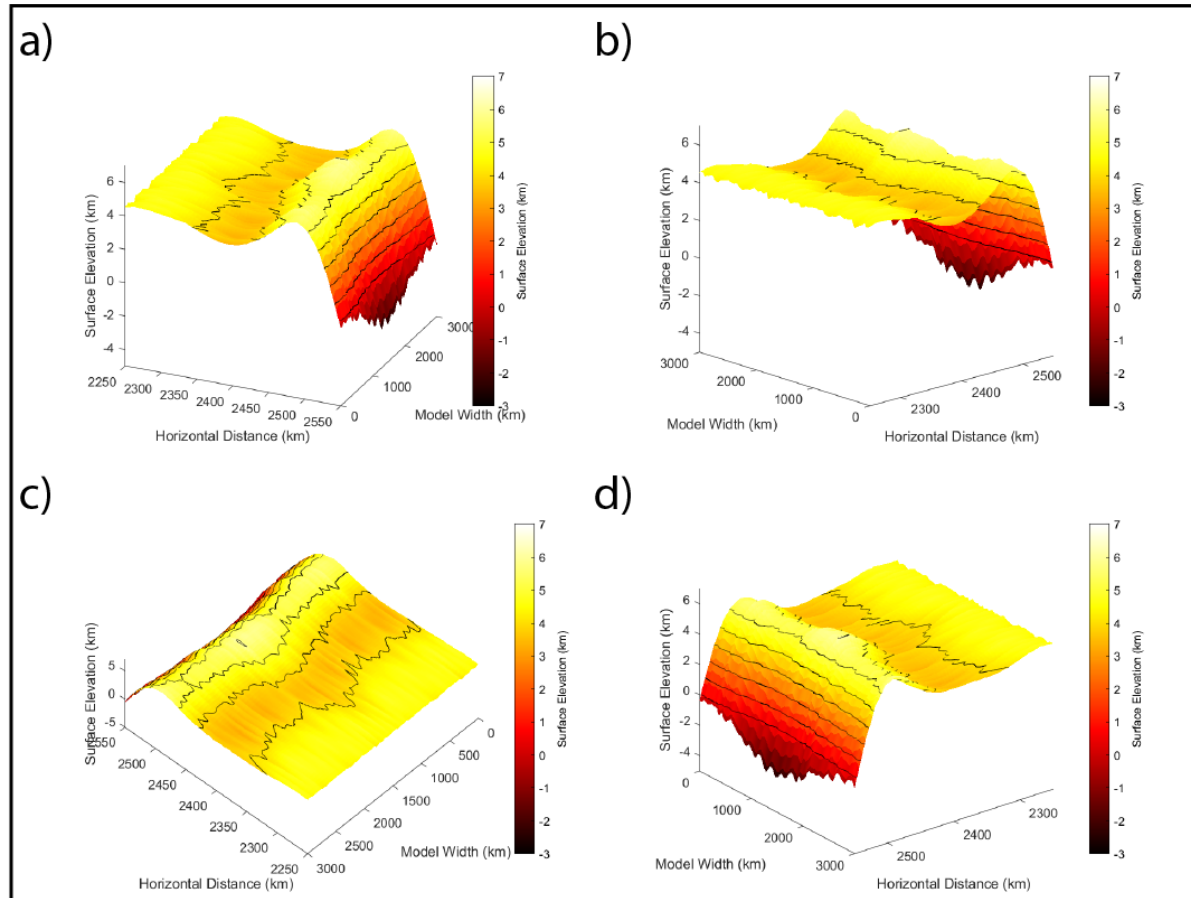
Figure 4.30 A series of contoured surface plots of the three-dimensional subduction model version 56 where, a) Camera angle looking from the z = 0 direction obliquely across and away from the orogen, b) Camera angle looking from the z = 0 direction obliquely across and toward the orogen, c) Camera angle looking from the z = 3000 direction obliquely across and toward the orogen at a higher camera elevation, d) Camera angle looking from the z = 3000 direction obliquely across and away from the orogen.

curved section of the subduction arc (Figure 4.30). This apex is located 33 kilometers further landward than sections of the subduction arc that show no curvature (Figure 4.30, Table 4.3). From z = 1630 kilometers to z = 2330 kilometers the curvature is approximately 0.047 km/km, and as z increases from 2230 kilometers to the edge of the model domain at 3000 kilometers the curvature returns to 0 km/km (Figure 4.30, Table 4.3).

4.2.5   Rectangular "slit" models (v57-v58)

For these models results are presented such that the surface topography results are discussed first, followed by the curvature of the orogen along the width of the model domain for models with thinner rectangles that are elongated in the length (version 57, x dimension) and width (version 58, z dimension) but located at the center of the model domain.

4.2.5.1   Model version 57

The volume of missing lithosphere for the x-elongated rectangular slit is calculated to be 750,000 km^3 from a hole geometry of 150 kilometers in length x 50 kilometers in width x 100 kilometer slab thickness, and remains at the center of the origin (Table 3.4). The location of maximum topography is at a distance of 67 kilometers leftward from the trench, at z = 1788 kilometers, and is at a total elevation of 5.97 kilometers (Figures 4.31-4.32, Table 4.3).
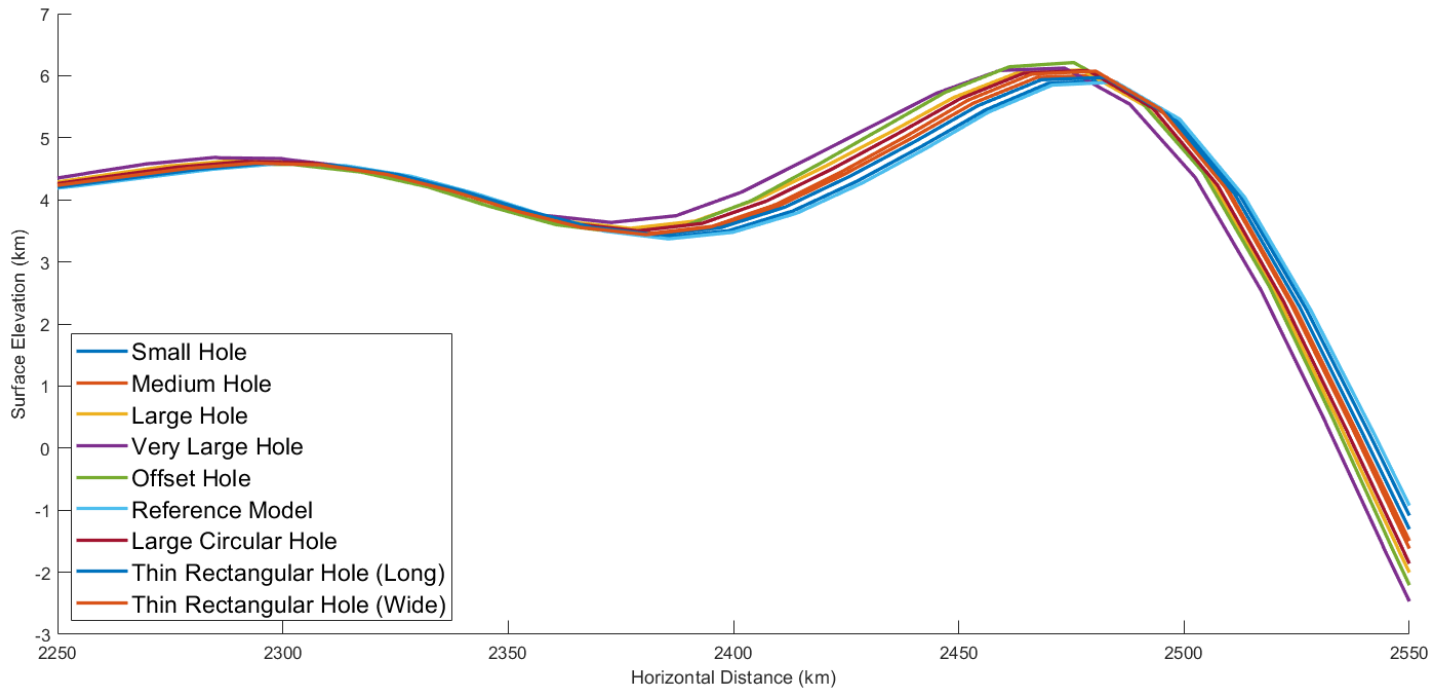
Figure 4.31 Plot of surface topography in all three-dimensional models where only one slab hole is introduced alongside the reference model. The profile for each plot is taken through the point of maximum topography (represented by red stars in map view figures) in the increasing x-direction (perpendicular to the orogen and trench). Thus, the profiles go from 2250 kilometers at the far left to 2550 kilometers at the far right. The z coordinate for all profiles is either 1787 or 1788 kilometers depending on the occurrence of maximum topography in the model (see Table 7 as a reference). Plot includes model versions 34, 35, 36, 37, 46, 47, 56, 57, and 58.

Figure 4.32 Plot of surface topography in all three-dimensional models where only one slab hole is introduced alongside the reference model. The profile for each plot is taken through the point of maximum topography (represented by red stars in map view figures) in the increasing z-direction (parallel to the orogen and trench). Thus, the profiles go from 0 kilometers at the front to 3000 kilometers at the back. The x coordinate for all profiles depends on where the maximum topography occurs (see Table 7 as a reference). Plot includes model versions 34, 35, 36, 37, 46, 47, 56, 57, and 58. The "fit" lines refer to the 10th order polynomial fit used to better identify overall topographic

The subduction arc curvature approximation for the area of the orogen between z = 0 kilometers and z = 995 kilometers is ~ 0 km/km, but then changes to 0.014 km/km between z = 995 kilometers and z = 1720 kilometers (the apex of curvature in the model) which encompasses the lower section of the arc. The apex of the curvature is located a maximum of 10 kilometers from the horizontal location of the orogen unaffected by arc curvature (Table 4.3). On the upper side of the apex from z = 1720 kilometers to z = 2315 kilometers, the curvature is approximately 0.017 km/km, and beyond z = 2315 kilometers the curvature is ~ 0 km/km. The arc in this model is considered symmetrical.

4.2.5.2   Model version 58

Similar to the previous slit model but with the elongation direction reversed so the slit is perpendicular to the trench, the volume of lithosphere missing is calculated to be 1,250,000 km^3, determined from a hole geometry of 50 kilometers length x 250 kilometers width x 100 kilometer slab thickness (Table 3.4). The location of the maximum topography in the model is 70 kilometers leftward/landward of the trench and at z = 1788 kilometers. The elevation at the highest point of topography in the orogen is 6.07 kilometers (Figures 4.31-4.32, Table 4.3).

Curvature from z = 0 kilometers to z = 1030 kilometers is approximately 0 km/km. Between z = 1030 kilometers and z = 1545 kilometers the orogen shifts 20 kilometers leftward, giving an average curvature of 0.039 km/km over this model width (Table 4.3). The extent of the curvature, the apex, of this subduction arc is at z = 1545 kilometers, and from this point until z = 2075 kilometers the arc curves back 20 kilometers oceanward with an average curvature of 0.038 (Table 4.3). From z = 2075

kilometers to the edge of the model domain at $z = 3000$ kilometers the arc has no further

curvature. Because the two areas of curvature on either side of the apex (0.039 km/km

and 0.038 km/km) were within the bounds of what we consistently consider symmetrical,

we assume this is a symmetrical subduction arc as well.

4.2.6 Double hole models (v59-v65)

In the double hole models, the holes never change size, only the distance between

them changes, thus each hole and each model version overall have the same amount of

lithospheric volume missing; 130 kilometers length x 150 kilometers width x 100

kilometer slab thickness multiplied by two because of the presence of two holes, giving a

total LVM of 3,900,000 km^3 (Table 3.4). With the exception of the model versions with

highest separation (800, 1000 and 1200 kilometers between the holes), the point of

maximum topography is essentially the same, a horizontal distance 78-79 kilometers left

of the trench and $z = 1787$ kilometers (Figures 4.33-4.34, Table 4.3). The 100 km, 200

km, 300 km, 600 km hole separation models produce maximum topography of 6.14

kilometers, 6.14 kilometers, 6.13 kilometers, and 6.08 kilometers, respectively. (Figures

4.33-4.34, Table 4.3). Meanwhile, the versions with 800, 1000, and 1200 kilometers of

separation between the two slab holes produce maximum topography of 6.04 kilometers,

6.04 kilometers, and 6.03 kilometers, respectively. The locations of maximum

topography for these versions are all between 1969 kilometers and 1970 kilometers.

All double hole models have a section of the orogen beginning at $z = 0$ that

stretches some distance where the curvature of the arc/orogen is ~ 0 km/km. For the

model with 100 kilometers separation between the two slab holes, this is extends to $z =$

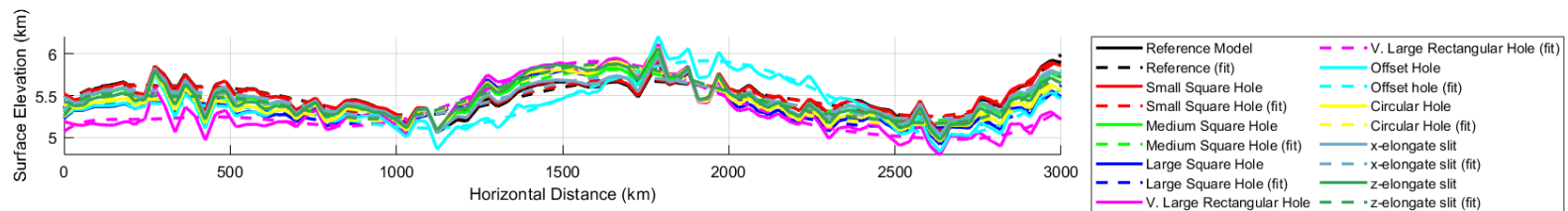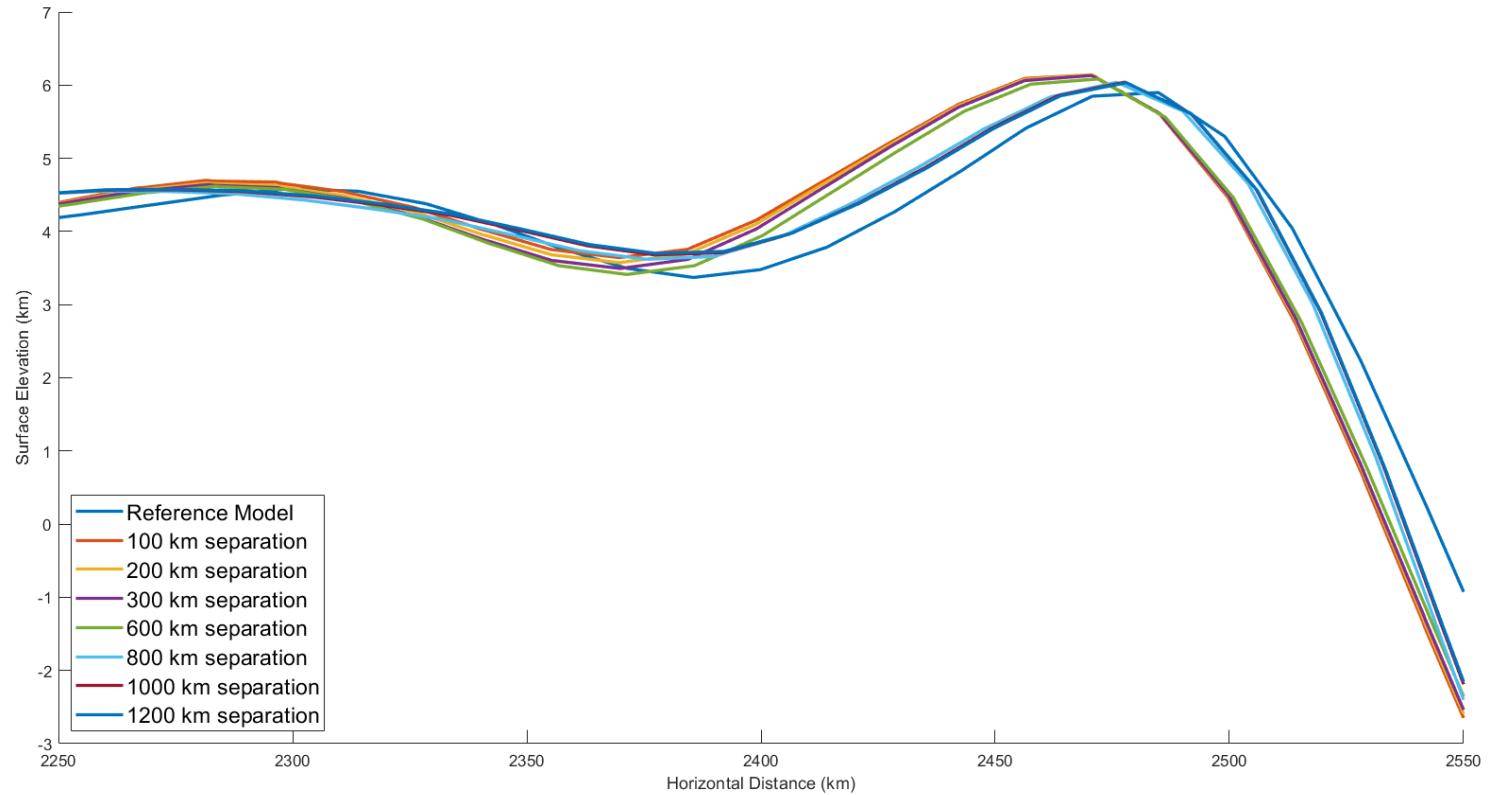**Figure 4.33** Plot of surface topography in all three-dimensional models where two slab holes are introduced and the reference model. The profile for each plot is taken through the point of maximum topography (represented by red stars in map view figures) in the increasing x-direction (perpendicular to the orogen and trench). Thus, the profiles go from 2250 kilometers at the far left to 2550 kilometers at the far right. The z coordinate for all profiles is either 1787 or 1788 kilometers depending on the occurrence of maximum topography in the model (see Table 7 as a reference), except for versions 60, 64, and 65 which occurs at z = 1970 kilometers and z = 1969 kilometers, respectively. Plot includes model versions 47 and 59-65.
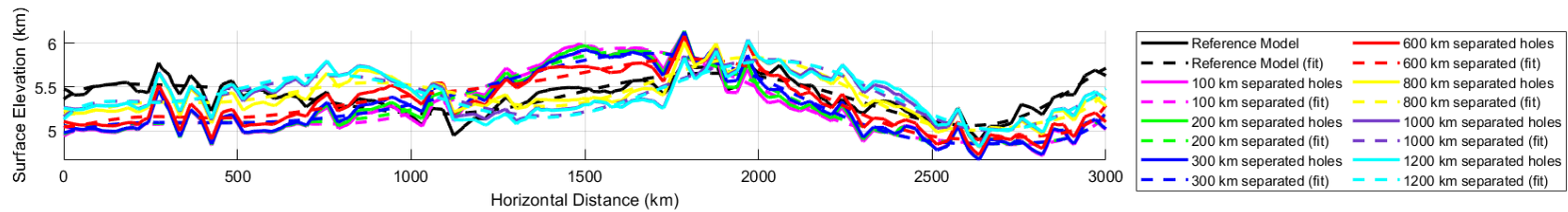
Figure 4.34 Plot of surface topography in all three-dimensional models where two slab holes are introduced and the reference model. The profile for each plot is taken through the point of maximum topography (represented by red stars in map view figures) in the increasing z-direction (parallel to the orogen and trench). Thus, the profiles go from 0 kilometers at the front to 3000 kilometers at the back. The x coordinate for all profiles depends on where the maximum topography occurs (see Table 7 as a reference). Plot includes model versions 47 and 59-65. The "fit" lines refer to the 10th order polynomial fit used to better identify overall topographic trends.

680 kilometers, with 200 kilometers separation this extends to z = 775 kilometers, with

300 kilometers separation extends to z = 685 kilometers, 600 kilometers separation

extends to z = 645 kilometers, 800 kilometers separation extends to z = 535

kilometers,1000 kilometers separation extends to z = 395 kilometers, and 1200

kilometers separation extends to z = 495 kilometers. For double hole models that only

show one curvature apex, there comes to follow, as in previous models, a region where

the subduction arc curves landward to some extent.

For the 100-kilometer separation model, this curvature is approximated to be

0.068 km/km and occurring between z = 680 kilometers and z = 1490 kilometers (the

apex), where the apex is offset 60 kilometers from the original horizontal position of the

orogen (Table 4.3). The curvature on the upper side of the orogen is approximated to be

0.076 km/km and occurring between z = 1490 kilometers and z = 2275 kilometers. The

curvature of the orogen produced in this model is asymmetrical. Similarly to previous

model results, beyond z = 2275 kilometers there is no curvature to the orogen.

For the 200-kilometer separation model, the curvature is approximated to be

0.059 km/km and occurring between z = 775 kilometers and z = 1535 kilometers (the

apex), where the apex is offset 50 kilometers from the original horizontal position of the

orogen (Table 4.3). The curvature on the upper side of the orogen is approximated to be

0.065 km/km and occurs between z = 1535 kilometers and z = 2300 kilometers. The

curvature of the orogen produced in this model is asymmetrical. The remaining region of

the orogen between z = 2300 kilometers and z = 3000 kilometers has curvature that is ~ 0

km/km.

For the 300-kilometer separation model, the curvature is approximately 0.046

km/km and occurs between z = 685 kilometers to z = 1550 kilometers (the apex), where

the apex is offset 45 kilometers from the original horizontal position of the orogen (Table

4.3). The curvature on the upper side of the orogen is approximately 0.058 km/km and

occurs between z = 1550 kilometers and z = 2320 kilometers. The curvature therefore

produced in this model is asymmetrical. The rest of the orogen between z = 2320

kilometers and the end of the model domain has curvature that is ~ 0 km/km.

For the 600-kilometer separation model, the curvature is approximately 0.030

km/km, which occurs between z = 645 kilometers and z = 1635 kilometers (the apex),

where the apex is offset 35 kilometers from the original horizontal position of the orogen

(Table 4.3). The curvature on the upper side of the orogen is approximately 0.050 km/km

and occurs between z = 1635 kilometers and 2325 kilometers. The curvature therefore

produced in this model is asymmetrical. The rest of the orogen in the model between z =

2325 kilometers and the edge of the model domain has curvature ~ 0 km/km.

Finally, for the 1200-kilometer separation model, the curvature is approximately

0.065 km/km, which occurs between z = 495 kilometers and z = 805 kilometers (the first

apex), where this particular apex is offset 20 kilometers from the starting position of the

orogen for the initial beginning 495 kilometers along the orogen. The first amount of

curvature to the subduction arc back in the oceanward direction occurs from z = 805

kilometers to z = 1170 kilometers and is approximately 0.085 km/km (Figure 4.35, Table

4.3). Between z = 1170 kilometers and z = 1710 kilometers there is no curvature in the

orogen. The subduction arc then begins to curve back landward again from z = 1710

kilometers to z = 2005 kilometers (the second apex) with an approximate curvature of
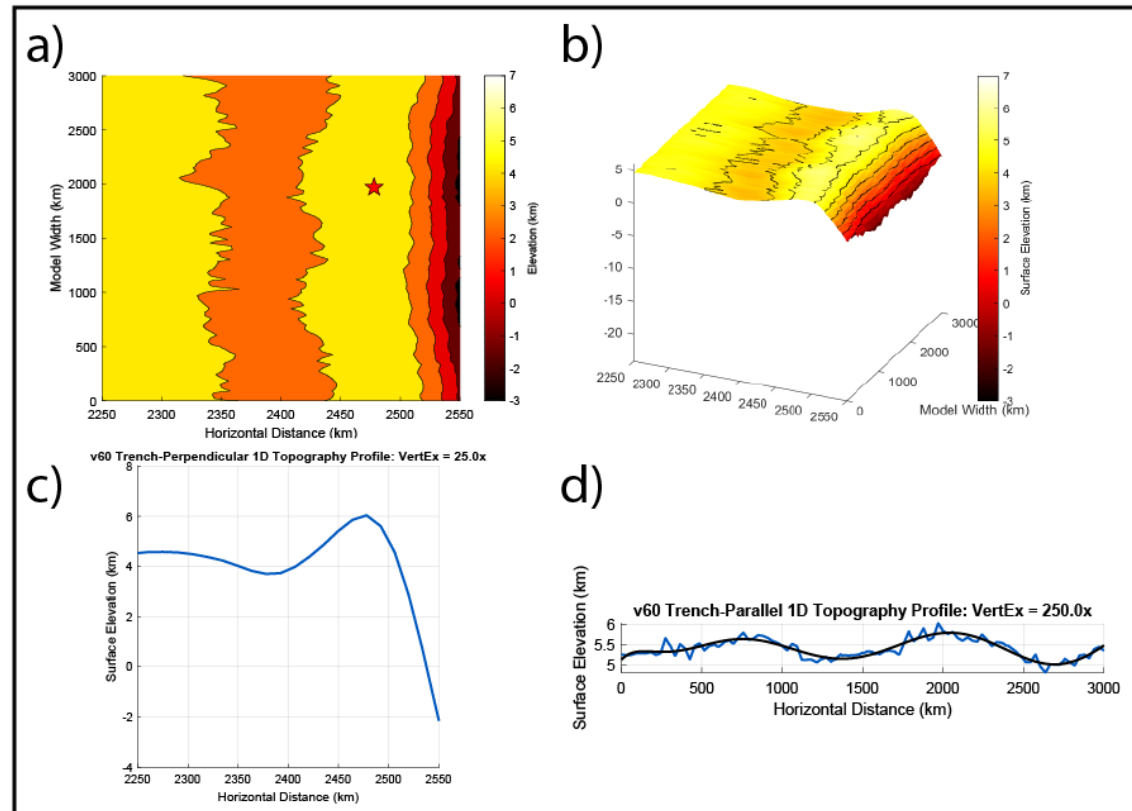
Figure 4.35 All data gathered for the three-dimensional subduction model version 60 consisting of two double slab holes spaced 1200 kilometers apart, including a) Map view/contour plot of the surface topography elevation approximately the first 300 kilometers landward from the trench, with a red star indicating the exact point of highest orogenic topography, b) Oblique view of a surface plot of the same topography in part a, c) 1-D transect of surface topography data along a line that passes through the star and travels exactly horizontal through the figure from 2250 kilometers to 2550 kilometers (perpendicular to the trench and orogen), d) 1-D transect of surface topography data along a line that passes through the star and travels exactly vertical through the figure from 0 kilometers width to 3000 kilometers width (parallel to the trench and orogen).

0.068 km/km (Figure 4.35, Table 4.3). The second apex in this subduction zone is offset 25 kilometers from the starting position of the orogen. Once again, the arc begins to curve oceanward from the second apex location to $z = 2515$ kilometers, with an approximate curvature of 0.039 km/km (Figure 4.35, Table 4.3). The final region of the orogen between $z = 2515$ kilometers and $z = 3000$ kilometers consists of no curvature. Neither region of curvature in this model version are symmetrical.

Additional models ran were the 800-kilometer and 1000-kilometer separation models. These models were specifically ran to further address the distance at which the topographical signature for both holes is present. In the 800-kilometer separation model, the curvature on the lower section of the orogen is 0.067 km/km, while on the upper section of the orogen this becomes 0.055 km/km. In the 1000-kilometer separation model, there are two signatures of curvature present, with the first (closer to $z = 0$ kilometers) lower section being 0.045 km/km and the first upper section being 0.050 km/km (Table 4.3). The second curvature signature (closer to $z = 3000$ kilometers) has a lower section curvature of 0.055 km/km and curvature in the upper section of this signature is 0.027 km/km. The only symmetrical curvature signature about the apex in either model is the first signature in the 1000-kilometer separation model, with the remainder of the signatures being asymmetrical (Table 4.3).

From these 3D models we see an increase in the amount of topography in an orogen given larger volumes of lithosphere missing. The location of maximum topography does not vary greatly, especially parallel to the orogen, but varies slightly with added curvature perpendicular to the orogen/trench. Additionally, the amount of curvature present in the orogen, though varying unpredictably in terms of symmetry,

115

consistently shows an increase when a large slab hole is added to the subducting slab. If

two slab holes are present, there could be two distinct signatures of curvature provided

that the distance between the two holes is >800 kilometers (1000 kilometers being ideal).

CHAPTER 5. DISCUSSION

This section discusses the implications of the results mentioned in the previous chapter (Results). First discussed are the two-dimensional findings, followed by the three-dimensional findings and concluding with a discussion with regards to all models.

5.1   Two-dimensional Mechanical Models

5.1.1   Surface topography overview

The surface topography data shows significant variations across both regular subduction models and flat slab models, all of which remain within reasonable values for convergent margins (Figure 4.1). Values for maximum topography range from over 7 kilometers at the highest (model version 194, the flat slab model with a slab hole), to 5.60 kilometers at minimum (model version 154, regular subduction model with a large slab tear). Despite the many differences that can be observed between each model, all surface topography results appear to follow the same pattern, similar to real-world patterns within convergent tectonic settings. The pattern includes the presence of topography distant from the margin, near the leftmost section of the continental block, followed by a second, usually less prominent peak between 150 and 200 km rightward of the left wall of the model domain. Heading rightward from this point, there is no significant topographical features other than the initial uplift for most models until >700 km from the left wall of the model domain. At this point, many models begin to form what we interpret to be the back arc basin, which ranges in depth and extent depending on the amount of uplift present in the origin. After the back arc basin, the orogen of the subduction system is

present, with uplift much more prominent in models with smaller amounts of missing

lithosphere or no missing lithosphere at all. The extreme slope to the right of the origin,

starting shallower and getting steeper, represents the extreme elevation change present in

the deep ocean trench present in subduction zones. In some models, these trenches are

steeper, while in others they appear more gradual. In addition to this, the horizontal

location of each trench is in three notable clusters (Figure 4.1). All simulations, when

visualized together, as seen in Figure 4.1, show topography data trends that seems to fall

into three categories: One category, being all flat slabs, the second being normal

subduction zones that do not involve slab breakoff, and the final being normal subduction

zones that involve slab breakoff (Figure 4.1). The presence of flat slabs causes the

features observed in two-dimensional subduction models to be exaggerated, including

back-arc basins, orogenic topography, and trench migration. In normal models, where

less slab is present to begin with, slab breakoff more easily restricts the formation of

significant surface topography, which has been shown in previous studies (Crameri et al.,

2012).

5.1.2   Comparisons of surface topography in regular subduction zones

Surface topography behavior in regular subduction zones is visualized by

removing the flat slab cases to focus in on the specific features distinguishable when a

normally subducting slab either breaks off or remains intact throughout the first 10-18

Myrs of subduction (Figure 4.5). Figure 4.5 shows the surface topography for all non-

flat-slab two-dimensional models. It is apparent that modifying the amount of missing

lithosphere, whether enough for a slab hole or only enough such that the slab is torn, can

cause variations in surface topography. Normal subduction cases appear to fall into two clusters in terms of their resulting surface topography. One group includes subducting slabs where breakoff occurs soon after initiation, and the other group includes models where slab breakoff never occurs. This pattern occurs regardless of whether the tear in the subducting slab is located on the bottom or the top of subducting lithosphere (Figures 4.4, 4.7).

The primary differences between the two aforementioned clusters are that in cases where subducting slabs break off, surface topography in the orogen becomes much less pronounced, while the topography near the left wall becomes more pronounced. The most likely explanation for this is that this must be where compression is accommodated in the overriding plate when the subducting slab is short. Because both models with large tears (top and bottom) involved slab breakoff, as well as the model with a complete lithospheric gap, the topography data shows their maximum topographical high in the region <200 km away from the left wall (Figure 4.12). The other main difference between models with and without breakoff is the amount of trench migration in the normal subduction models (Figure 4.5, Table 4.1). The trench appears to migrate more in cases where slab breakoff does not occur, as well as exhibits a steeper topographical signature from the top of the orogen to the depths of the trenches. It is reasonable to deduce that because a longer slab continues to subduct, that subsequently, the trench can continue migrating. The trench advances for the length of model time we are interested in, which is partly because the slab does not roll over on itself during the window of time analyzed in this work, a factor that has been explored in detail in past work (Tagawa et al., 2007).

5.1.3 Comparisons of surface topography in models with flat slabs

In flat slab cases, the surface topography produced some more pronounced features than the corresponding cases in normal subduction models. In all cases explored involving flat slabs, a back-arc basin was produced, the extent and minimum topography of which varied depending on the type of slab gap present. The reference model (v190) suggests the largest back-arc basin, while the smallest basin produced was from the slab hole model (v194). This back-arc basin occurs between 800 and 850 kilometers right of the edge of the model domain, just before the orogenic topography. Similarly to the normal subduction cases, there is varying amounts of topography near the edge of the model domain at the left wall. The largest topographical high near the model edge is generated from the large tear model (v197), likely related to the fact that the lowest topography elevation occurs in the orogen in this version. The smallest edge topography generated is in the reference model, which subsequently shows significantly more topography in the orogen.

The amount of trench migration involved in each model is also explored. In all flat slab models, trench advance is more significant than in any normal subduction case (Table 4.1). The reference model (v190) and slab hole cases (v194) exhibit the most trench migration, and likewise have the highest average trench migration rate of any model (Table 4.1). Additionally, the large tear flat slab model has the next highest amount of trench migration and average trench migration rate. This seems to confirm that flat slab models exhibiting trench advance should be explored separately from normal subduction cases when examining the effects of missing lithosphere. This could indicate

there are other dynamics at play. The increased trench migration rate is likely influencing other factors within flat slab models such as surface topography produced.

5.1.4　Max orogenic topography versus missing lithosphere

Figures 4.18 and 4.19 show graphs of maximum topography versus missing lithosphere for models with bottom tears (Figure 4.18) and top tears (Figure 4.19). The correlation between missing lithosphere and topography change was able to be fit with a linear trend and the trends regarding the two tear types are shown in Figure 5.1. The linear trend predicted by the least squares inversion has a high correlation to the observed values of maximum orogenic topography in models that include bottom slab tears (Figure 4.18). Figures 4.18 and 4.19 show a clear trend that when more lithosphere is missing from a two-dimensional subducting slab, less topography is present in the orogen. The small tear model (version 152) was much more able to represent this trend than the medium and large-sized tears (version 153 and154). The lithospheric gap (version 155) is the closest data point to nearly being an exact prediction by the least squares inversion, implying the likeliness of substantially less topography in such cases.

The trend predicted by the least squares inversion for top-of-slab tears also has a correlation to observations of maximum orogenic topography (Figure 4.19). Arguably, the results presented for top-of-slab tears, despite having what appears to be a non-linear solution, is fit well through least squares inversion methods, as indicated by a higher R^2 than with bottom-of-slab tears (R^2 increase from 0.95776 (bottom tears) to 0.9625 (top tears) (Figure 4.19). In this case, the two most inaccurate predictions by the inversion are the reference model case (v171) and the small tear case (v205). As the size of tears
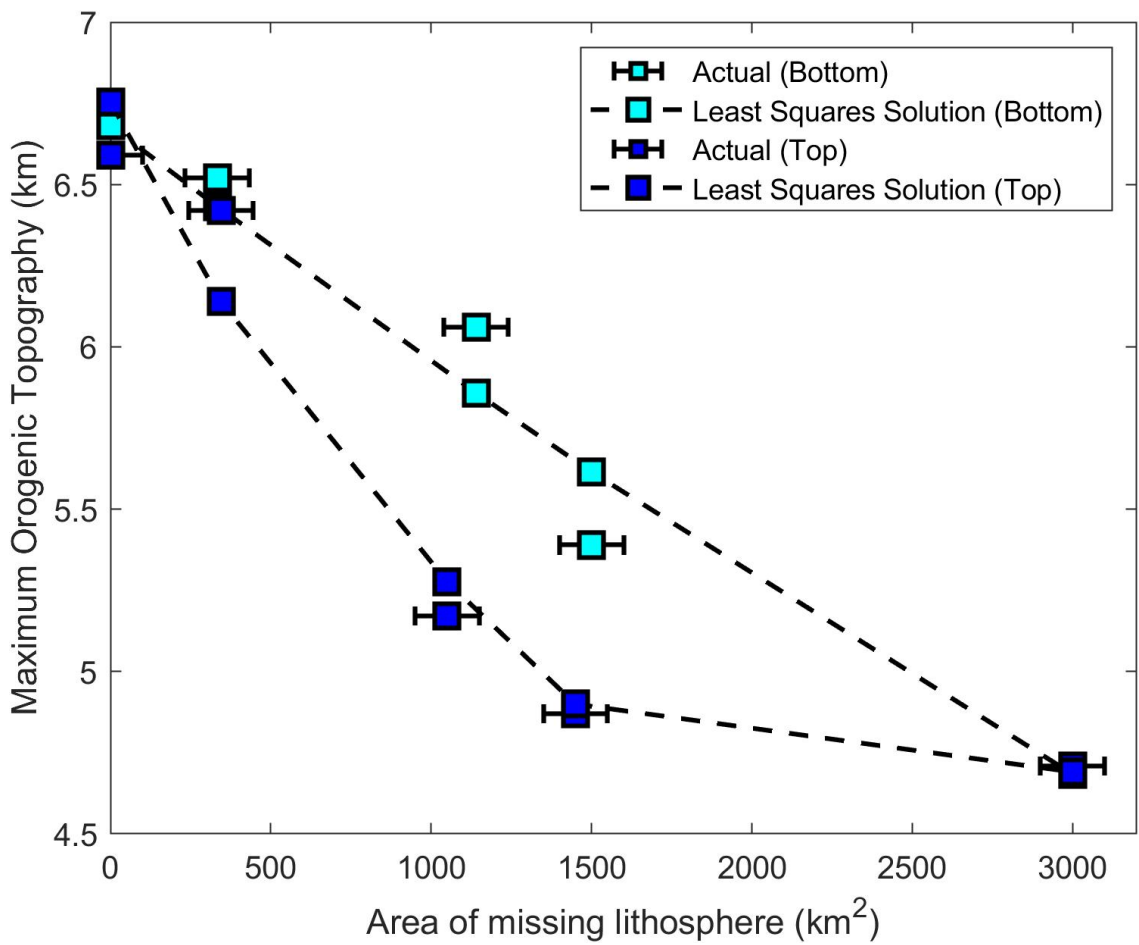
Figure 5.1 Data from figures 32-33 compiled onto one figure for comparison. Refer to Fig 32-33 for more information on the fit of least squares solutions. Darker blue shows the top-of-slab tears while the lighter blue data points represent the bottom-of-slab tears. Dashed lines represent the least squares solutions that were determined for both.

introduced (and eventually the gap) grows, the differences between predictions and observations decreases substantially (Figure 4.19).

Compared to one another, it is evident that different least squares solutions are required when dealing with a slab that is torn on the bottom versus one that is torn from the top (Figure 5.1). Recent research suggests that slabs tear from the top rather than from beneath, as the top of slabs face more resistance upon subduction into the trench from various subducting features (Ferrari, 2004; Gvirtzman and Nur, 2001; Levin et al., 2002; Millen and Hamburger, 1998; Wortel and Spakman, 2000). Given this information, the average slab is most likely to follow the top-tear trend observed in Figure 4.19 and Figure 5.1 more so than the trend observed by bottom tears (Figure 4.18 and Figure 5.1). Thus, the trend likely observed in nature from a two-dimensional perspective is more of an exponential decay or decrease of produced topography in the orogen relative to missing lithosphere amount rather than of a linear decay/decrease.

5.1.5   Comparisons of the velocity profiles in normal subduction cases

Figure 4.2 compares all normal subduction velocity profiles. There is a large amount of variation in horizontal velocity throughout the upper mantle, oceanic lithosphere, mantle wedge, and even continental materials in these velocity profiles (Figure 4.2). The velocity profiles of slabs that are torn on the bottom tend to show a smaller signature of attempted asthenospheric flow into or through the slab tear (Figures 4.6, 4.10, 4.13) compared with slabs that were torn on the top (Figures 4.8, 4.11, 4.14). For models with bottom tears (version 152 through 154) it is hardly apparent in the velocity profile that there is a tear at all if examining only the region where an anomaly is

anticipated. Despite this fact, the flow field in the cases where tears are implemented on the bottom of the slab seems to show irregularities that are not present in the reference model (with no lithospheric gap). The lack of prevalent velocity anomalies from tears along the base of could likely stem from the direction and magnitude of the mantle wind as it approaches the subduction zone (Chen et al., 2016). In cases where tears are on the bottom of the subducting slab, the mantle flow travels in nearly the opposite direction compared to the flow direction necessary to penetrate the lithospheric gaps. This could potentially be thought of by using a constructive interference analogy. In the case of a tear to the bottom of a slab, larger mantle convection forces (due to subduction) are driving flow away from or tangentially to the hole rather than towards the hole. This does not rule out the possibility that flow penetrates into torn lithosphere, but the anomalies are much more difficult to see due to the larger mantle wind convection near the margin (Chen et al., 2016). Nevertheless, the flow field in both the mantle wedge region, the subducting slab, and the sub-lithospheric mantle is clearly perturbed compared to the reference case (albeit often only by small amounts) by the existence of these features.

Furthermore, because the velocity anomalies were small for models featuring bottom tears, calculating the amplitude (difference between average and peak velocity near slab gap) for them proved to be difficult and somewhat inaccurate. Thus, the primary region with the most uncertainty in velocity values is around the tears and into the base of slabs. Calculating these values for tears on the top is less difficult, due in part to the nature of the surrounding velocities in the profile, but also the anomalies are more symmetrical and have higher magnitudes.

The material field is used to confirm the presence of the mantle material within the torn slab, which is visible in bottom tear versions, albeit is not as distinct as in the top tear versions. The material field can appear erroneous due to the averaging scheme used to obtain the material field for an average of data points needed to provide a smooth profile. For instance, the material field in the model with a small tear to the bottom (version 152) is determined to be greater than 6 at the location of the velocity anomaly (due to the slab gap) and so would imply the presence of continental mantle lithosphere, which we know based on the profile location cannot be the material at this depth. Instead, it would hold a theoretical value of 3 if the scheme allowed for hard boundaries between different materials, but since these are smooth boundaries, we get a value of 6.18. This is about average for a region where most materials hold a value of 7-9 (values representing oceanic lithosphere materials) with only a small amount of material holding a value of 3 (upper mantle) until a bit deeper. Using the material field and velocity field together proves to be the most helpful in locating where a velocity anomaly could be, based on the materials present there, and subsequently determining the magnitude of the flow at this point.

The primary distinguishable factor in terms of analyzing the velocity of flow in these subduction models is how the overall flow field is affected upon the introduction of slab gaps and tears to the subducting slab, which is apparent in each model (Figure 4.2). Despite the fact that many models may differ in the velocity magnitudes and directionality throughout the profile, there are consistent, observable perturbances to the flow field in several locations that do not exist in the reference case. The maximum observed velocities in any part of the profile beneath the continental mantle lithosphere

do not reach those of the reference case (Figure 4.2). Top tears exhibit a very sharp change from an increase in velocity with depth to decreasing velocities at approximately 350 kilometers depth, which is not at all the case in the reference model or bottom tear models. This may indicate that tears to the top of the lithosphere can uniquely effect flow at certain ~~times~~ locations beneath the subducting lithosphere. A unique velocity signature is seen in models with tears on top of the slab (versions 206 and 208) that shows small perturbations near the transition zone just beneath 600 kilometers depth (Figure 4.2). There is a similar slight velocity anomaly visible in this region in the slab gap model (version 155).

The most convincing argument for asthenospheric flow into a slab tear can be examined in models with slab tears on the top (version 205, 206, and 208), where the velocity anomalies are clearly visible and line up with the slab gap locations in the model profile snapshots (Figures 4.8, 4.11, 4.14). The values mentioned previously (Table 4.2) reflect the flow magnitudes, depths, and material indexes. The velocity anomalies line up with a decreasing material field anomaly which happens at 177 km, 169 km, and 177 km depth in version 205, 206, and 208, respectively, which also align with the model snapshots showing the location of the slab gap. Just as in the normal subduction cases, a decrease in the material field in this region corresponds to upper mantle material. Any subsequent increase in material index resembles a return to oceanic lithosphere.

5.2   Three-dimensional Mechanical Models

This section discusses the results from the three-dimensional models and their implications. The models discussed feature lithospheric gaps of various sizes, shapes and locations along the slab.

5.2.1   Effect of changing the size of a slab hole (v34-v37, v47, v57, v58)

Contrary to observations with two-dimensional slab holes, the amount of lithospheric volume missing correlates to an increase in surface topography (Figure 5.2, Table 4.3). The maximum observed surface topography in version 34 (the smallest hole) is the lowest topographical peak produced, aside from the reference model (version 47), at 5.92 kilometers elevation. Meanwhile, version 37 (the largest hole in this series) produces the maximum amount of surface topography within these models at 6.12 kilometers (Table 4.3). The locations of these points of maximum topography do not vary greatly from model to model, and in fact only vary by 1 kilometer in the width model dimension (Table 4.3). The locations in the model length dimension vary more, from 65 kilometers leftward of the trench in the reference model, to 76 kilometers from the trench in the model with the largest hole (version 37).

Not only are the values of maximum surface topography increasing with larger amounts of missing lithosphere, but the region of surface topography spanning hundreds of kilometers on either side of the hole is progressively slightly more uplifted as well (Figure 4.32). In addition to this, surface topography values further away from the slab hole on either side tend to be lower with a large hole present (Figure 4.32). These trends are even easier to observe with the addition of the 10th order polynomial fit that is
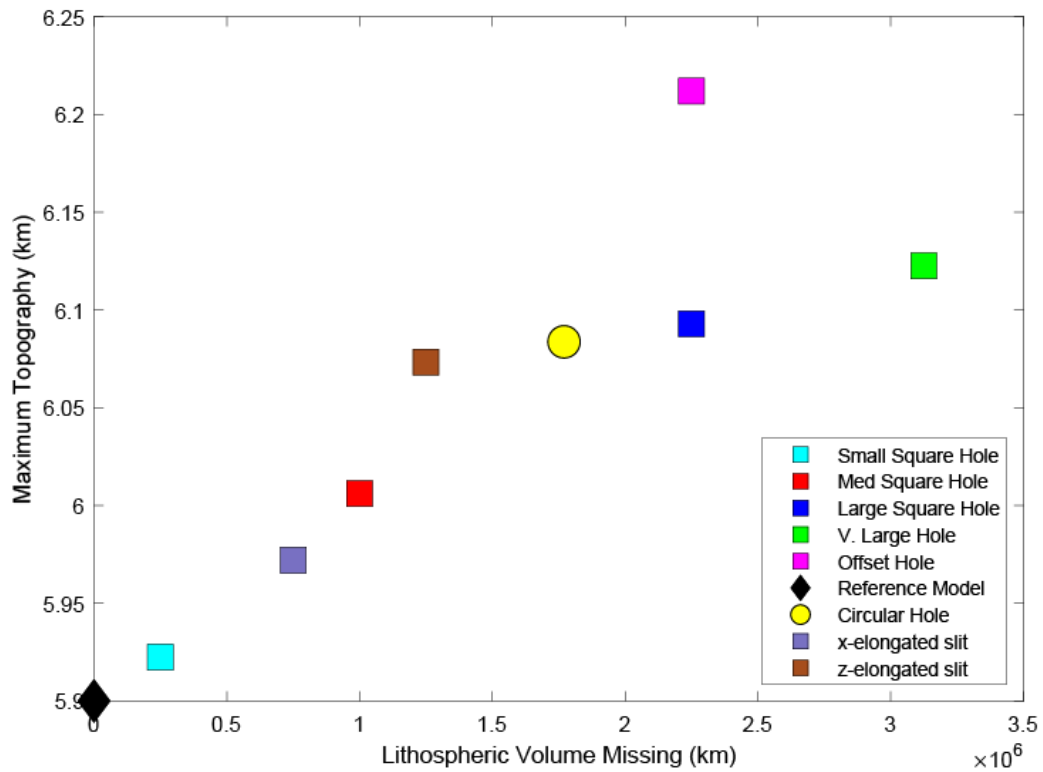
127

Figure 5.2 Plot of maximum surface topography data from all singular hole models in three dimensions versus the amount of volume missing from subducting lithosphere in the slab nose. Squares represent all rectangular or square models, while the circle represents the circular tear model (version 56). The diamond model represents the reference model for comparison (version 47).

showing the general topographical trend the best for each model (Figure 4.32). This suggests that the topography increase around the hole can be attributed to a concentrated lack of a slab pull force (especially in larger holes) to bring the slab down. This is supported by evidence that the slab pull force is one of two primary forces that pull subducting plates down (Conrad and Lithgow-Bertelloni, 2002). Because the slab in the region with missing lithosphere is not as susceptible to the slab pull force, the sinking of the slab in this region becomes unequal. This would cause more compressive resistance in the subduction zone and thus likely produce slightly more uplift in those regions. The models produce the maximum topographical anomaly consistently at $z = 1788$ kilometers, and it seems as though there is no evidence to suggest that adding or removing lithosphere changes the horizontal location of such a topographical feature. Variations in surface topography perpendicular to the trench (along the width of the over-riding plate) also occur, where a back-arc basin is interpreted just to the left of the orogen in each model, and trench migration increases with more missing lithosphere (Figure 4.31). As with the profiles parallel to the trench and orogen, more missing lithosphere results in more surface topography in the trench-perpendicular plots as well (Figure 4.31). Even though this trend is observed in the orogen, beyond this point landward the range of varying topography values is much less than in the orogen itself $< \sim 2400$ kilometers horizontal distance) (Figure 4.31).

Curvature results for these models demonstrate that more curvature tends to be present within subduction zones that contain larger lithospheric gaps (Table 4.3). In addition to this, the curvature of lower sections along the subduction arcs is consistently larger than that of the upper sections of subduction arcs (Table 4.3). The maximum offset

amount of the apex of curvature increases with larger lithospheric gaps (Figure 5.3, Table 4.3). The data suggests that curvature is likely produced in situations with lithospheric gaps because the subducting slab cannot deflect in the same manner it does in regions along its width where all lithosphere is intact and continuous. The modification/deflection of the subduction dip angle beyond the initial 30 ° as the system evolves through time is a process that is occurring at different rates depending on the continuity of the slab as it is subducting. It remains unclear what controls the symmetry of the resulting curvature produced in the subduction orogen are but could be related to various edge effects in the model, even near the middle of the model domain.

5.2.2   Effects of changing the slab hole location along the width axis (v46)

Model version 46 features a slab hole that is shifted from the center of the slab to 2000 km (near the far wall). This model version has the highest expression of surface topography at an individual point, despite no changes being made to the size of the hole when introducing it to the model 500 kilometers offset from the original, centered location, as in the reference model (version 47) (Figure 4.32, Table 4.3). This high surface topography is likely related to edge effects from the boundary of the model domain closest to the hole. Regardless of the offset distance of the hole, the maximum topography occurs at the same width as the other centered hole models of $z = 1788$ kilometers (Table 4.3). The location of maximum topography on the overriding plate is nearly identical to that of version 36, which has the same size slab hole but centered at $z = 1500$ kilometers. Changes in the surface topography in profiles taken parallel and perpendicular to the trench were not substantial from the centered hole models Overall,
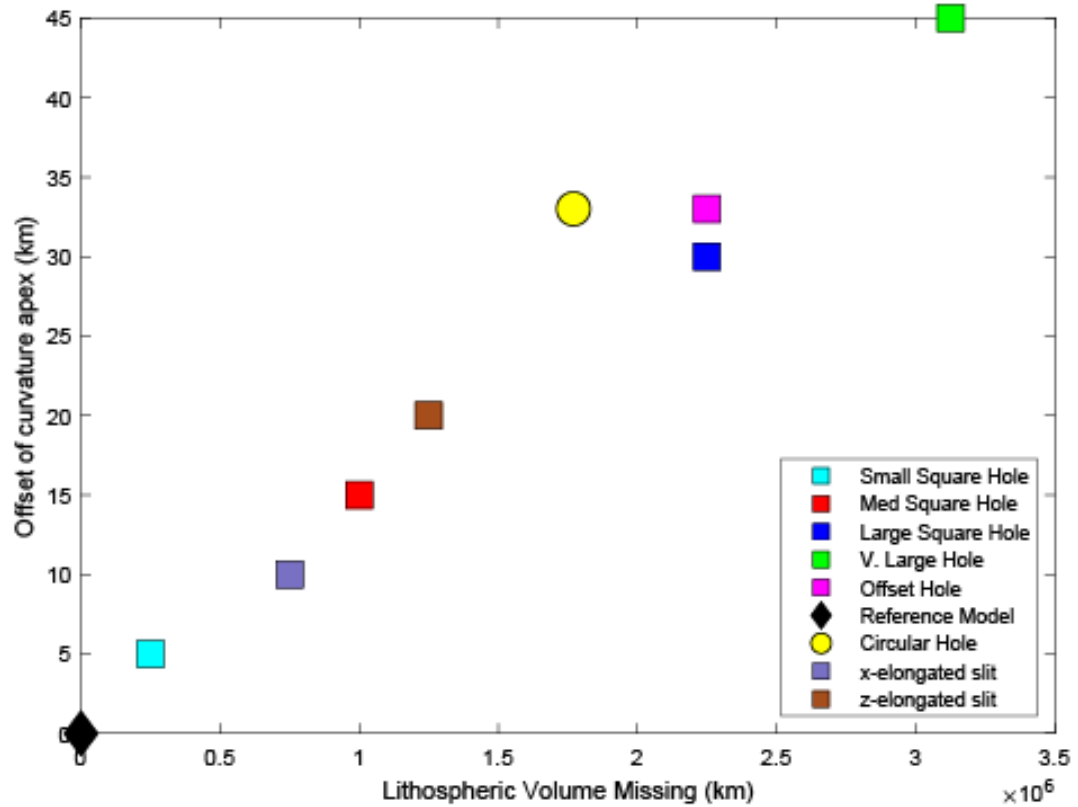
Figure 5.3 Plot of apex offset from the orogen at the initial orogen position versus amount of volume missing from subducting lithosphere in the slab nose. Squares represent all rectangular or square models, while the circle represents the circular tear model (version 56). The diamond model represents the reference model for comparison (version 47).

changing the location of the slab hole along the width of the model domain may have the unintended effect of producing higher topography, but otherwise produces results very similar to centered hole models (Table 4.3). Seeing migration of surface topography following the hole in this manner is another indicator that there is likely a connection between the presence of the gap and the corresponding surface topography signature.

The curvature in the orogen in the offset hole model remains within reason for the location and size of the hole introduced and was symmetrical despite the closer proximity to the back wall of the model domain. Upon comparing the curvature of the orogen as it runs parallel to the trench, the large region before the gap remains largely straight. The curvature, as expected, then begins upon approaching the region of the orogen above the slab gap until the apex of curvature at $z = 1865$ kilometers, and then the orogen curves back to the original horizontal position. This further supports slab curvature being generated by the slab hole and not some other subduction feature.

5.2.3 Circular vs square/rectangular slab holes (v56)

Changing the shape of the slab hole from a square hole of 150 kilometers x 150 kilometers to a circular one with a radius of 75 kilometers decreased the total volume of missing lithosphere in the circular hole model (Table 3.4). Despite this change, the results are very similar to the square model counterpart (version 36). The maximum topography is only 10 meters lower than that in version 36 (Table 4.3). The location of maximum topography does not differ substantially either, only 2 kilometers less of trench migration occurs with the circular hole (Table 4.3). The topography profiles reflect the similarities between the circular model and square one as well. The trench-perpendicular profile

shows that the circular model and square model are almost identical to one another

(Figure 4.31). This implies that the most influential factor on the highest peaks of surface

topography generated is not the shape of the slab hole, but rather its area or volume.

The curvature in the model with a circular hole has one big difference from the

corresponding model with the same size square hole. The curvature on the upper section

of the orogen beyond the apex is far greater than the curvature on the lower section

beneath the apex on the square model, but in the circular model the two curvatures are

nearly symmetrical. Despite this difference, the total offset of the apex from the original

orogen location for both models is very close, meaning that despite unequal curvature

along the orogen, both orogens shifted about the same amount in total at their respective

apexes (Table 4.3). As with topography, the curvature seems minimally impacted by the

shape of the hole, provided the shape of the slab hole itself is symmetrical.

5.2.4   Effects of cases with more than one slab hole (v59 – v65)

Analysis of the double hole models is to determine if there is a minimum size

and/or distance between slab holes which can be resolved by observing differences in

surface topography. The maximum topography produced in these models decreases

relative to increasing distance between slab holes (Table 4.3). This decrease in surface

topography can be explained based on the previous understanding that the more

lithosphere is missing, the larger the topographical peak produced. In the case of two

holes that remain close together, such as the 100-km separation model (version 63), 200-

km separation model (version 61), and 300-km separation model (version 62), the

topographical signature behaves as if there is one large slab hole beneath the orogen at

this location producing it. This also remains true for the 600-km and 800 km separated

slab holes. However, by the 1000-km separated slab hole model, the slab holes are far

enough apart that they produce two regions of curvature, one from each slab hole, and

they produce two topographical peaks at the surface (Figure 5.4). The 1000-km and

1200-km separated hole models are also the only ones to show a topography peak outside

of the typical $z = 1787$ kilometer to $z = 1788$ kilometer range, likely due to the presence

of two vastly separated slab holes. The models with two holes closer than 800 km apart

act like models with one giant slab gap equal in size to the sum of the two slab holes.

Visualization of the desired trend of initially one large topography signature, followed by

the first visualizations of two signatures at 800 km and 1000 km separation, are once

again made easier using the 10th order polynomial fit in the trench-parallel profiles

(Figure 4.34).

Comparing the curvature within the double hole models provides insight into

potential mechanisms for shaping subduction arcs and whether one or more slab hole can

be interpreted in subducting lithosphere from the curvature/shape of the slab. These

models show that two slab holes occurring along the same subducting slab will need to be

more than 800 kilometers apart to produce unique signatures of curvature along the

orogen, and for visibility of the two anomalies distinctly at least 1000 km apart. In the

double hole cases examined, none produced curvature that was symmetrical. Thus, one

could argue that two holes may exist there but not produce enough of a topographical

signature to be observed uniquely. The model with 1200-km slab hole separation (version

60) produces values of curvature for the two unique curvature signatures which vary

significantly, and the maximum apex distance from the original orogen location is only
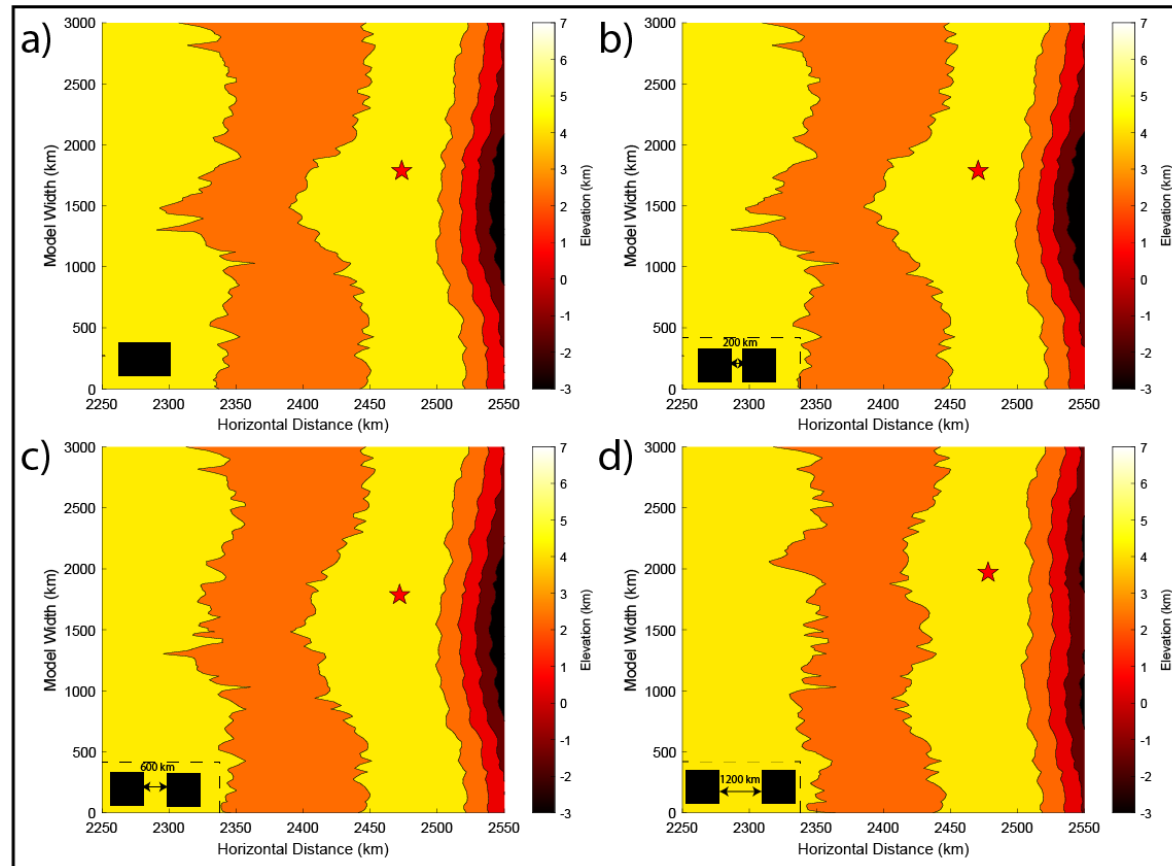
Figure 5.4 Map view comparison of surface topography produced from four three-dimensional subduction models, a) Model version 37 consisting of a rectangular hole, b) Model version 61 consisting of two slab holes separated by 200 kilometers of intact oceanic lithosphere, c) Model version 59 consisting of two slab holes separated by 600 kilometers of intact oceanic lithosphere, d) Model version 60 consisting of two slab holes separated by 1200 kilometers of intact oceanic lithosphere. Stars represent the location of the maximum surface topography in the orogen, while black shapes are another representation of slab hole configuration for clarification.

25 kilometers (Table 4.3). This implies that although the orogen has substantial curvature occurring in more than one location, the apex of curvature migrates substantially less landward than all other double hole models and a few singular hole models as well.

5.3   All subduction models taken into consideration

The results of two- and three-dimensional models are vastly different, and thus so are the resulting implications. The increased surface topography relative to missing lithosphere in three dimensions is the opposite of the results seen from two-dimensional subduction models. Our two-dimensional subduction models were preliminary results which were useful to give a better understanding of how subduction dynamics can play out where no lateral flow or differing subduction rates along a slab are allowed. Because of this, they may often still prove useful in determining flow patterns around the slab and into the mantle wedge. Two-dimensional subduction zone models are still widely used, and these results might be useful to future studies. To truly examine the effect of lithospheric slab gaps in subduction zones on surface topography or evolution of the orogen with slab holes present, a three-dimensional model is necessary. Slab holes cannot truly exist in two-dimensions, as two-dimensional slab holes are slabs that have already experienced slab breakoff (Duretz et al., 2011). The correlations noted in two-dimensions involving increasing surface topography with less missing lithosphere are more likely related to subducting slabs breaking off. Shorter slabs produce less topography which is exactly the effect we were seeing in our model results (Crameri et al., 2012). This does not dismiss the results of two-dimensional models but is to say that the larger scale geodynamics of these subduction models may play more of a role than lithospheric tears

136

and holes in creating the surface topography based on the scale of these models. Similarly, finding signatures of flow through slab holes in three-dimensions proved difficult because of the magnitude of mantle flow around the slab. All these velocity signatures were overprinted by mantle flow entering the mantle wedge and the resulting downward force on the slab, as well as the larger mantle flow around the base of the subducting lithosphere.

Many of the same trends exist across both two- and three-dimensional model types. The trench migration becomes visibly obvious in map view and surface plots of three-dimensional models and is likely playing a role in the subduction orogen curvature. In both model types, trench migration is greater when there is more missing lithosphere, meaning that a region corresponding to a slab hole should have a trench that migrates inward alongside the curvature, which is observed in all models. Additionally, both two- and three-dimensional models show the anticipated mantle flow patterns around the subducting slab including flow into the mantle wedge above the slab and flow beneath the subducting slab.

Finally, these results are all based on mechanical models of subduction zones. A key feature missing in these models is a thermal component, which may assist in visualizing flow through the slab holes (by looking for temperature differences), as well as exploring a subduction system in which the slabs are able to melt and follow laws of thermodynamics. Models presented in this work do not involve a thermal component, meaning the slabs cannot melt or deform based on the temperature in the system. Despite the exclusion of this component to these models, it is not expected that the trends observed in three-dimensions will change significantly, only expanded upon with

potential for more localized flow variations. This is because buoyancy forces and the slab

pull force are related to parameters already included in the models discussed in this work.

CHAPTER 6. CONCLUSIONS

This study has shown that gaps in the lithosphere are observable from velocity profiles through the slab gaps as well as topographic changes at the surface. The 2D results showed velocity perturbations to the slab and upper mantle when tears and gaps are introduced to the model, as well as a decrease in surface topography with missing lithosphere due to slab breakoff. The 3D results showed the surface topography along the orogen increases in the case that larger slab holes are present in the subsurface along the subducting slab. Also evident is that slab hole shapes and exact morphology matter less than the area of missing lithosphere itself. Finally, the presence of more than one slab hole in the subducting lithosphere can only be indicated from surface topography in the case that two slab holes are at least 800 kilometers apart.

In two-dimensional models of subduction, where flow and topography cannot be tracked parallel to the trench, anomalous flow through slab holes is often, but not always, visible. The visibility comes through a series of vertical velocity profiles taken through various tears which show flow/velocity moving through the hole/tear in the slab. The velocity profiles show anomalous velocity values/directions near the slab tears when they are located on the top of subducting slabs. Variations in velocity that could be attributed to asthenospheric flow into a slab tear are not as clear in cases with tears on the bottom of subducting slabs. In the cases with lithospheric tears on the top of subducting slabs, velocity values near the hole are larger than background particle velocity values, thus showing an anomaly in those regions. The two-dimensional topography data suggests that less topography is generated with a larger tear or slab gap in the subducting slab. However, this decrease in topography is likely a result of slab breakoff leaving a shorter

slab to generate topography near the trench, as has been seen in previous studies (Crameri et al., 2012). This suggestion of slab breakoff as a cause for decreasing surface topography is further supported by the results obtained in three dimensional mechanical models which showed the opposite trend. Additionally, two-dimensional flat slab models did not show an observable trend in maximum topography, however there are likely too few data points to draw significant conclusions regarding the impact of flat slabs specifically. Despite the lack of a trend in topography, observing the flat slab models alongside normal subduction cases revealed particularly exaggerated features such as larger back-arc basins and substantially more trench migration in flat slab subduction cases.

In three-dimensional models of subduction, topography and flow are trackable parallel and perpendicular to the trench, but anomalous flow that may be associated with asthenospheric flow through the slab holes is less clear. Large scale geodynamic processes tend to dominate the velocity field in such models and thus overprint the signatures of smaller-scale flow through slab holes. In three-dimensional models, more realistic slab holes can be parameterized, and many more trends can be observed regarding the surface topography. As the size of a slab hole increases, the elevation of surface topography increases across the width of the orogen. Some variations in the amount of topography generated are present perpendicular to the orogen as well but converge with increasing distance from the orogen. In addition to an increase in surface elevation, increasing the size of a slab hole seems to create more curvature within the orogen, particularly in the region above the slab hole. Moving the slab hole location within a model domain will shift the curvature accordingly as well. In cases where

multiple slab holes are present along the width of orogens, the distance between the two holes in the slab seems to be the primary control on the visibility of multiple topography signatures at the surface. If the distance between the edges of two slab holes in the same subducting slab is at least 800+ kilometers, the likelihood of seeing two regions of subduction arc curvature related to each of the two holes is greatest. Thus, a minimum distance of 800 km between slab holes would be necessary to observe them as separate holes and not as a (falsely) single anomaly.

Modifications to the continuity of subducting lithosphere can drastically change the shape, location, and trend of topography produced at the surface in subduction-related arcs. In addition to this, flow within the mantle is perturbed or altered due to the presence of a lithospheric gap, whether this be large scale geodynamics processes or smaller scale flow variations near certain regions of subducting slabs. Overall, subduction is a three-dimensional problem, and thus the three-dimensional models are most likely to replicate the mechanical conditions typical of the observable upper mantle and lithosphere. Slab holes are best represented in this manner and thus their influence at depth and at the surface are as well. Despite the vast amounts of data produced from mechanical subducting slabs, a thermal component could give insight into many of the questions that remain regarding the behavior of mantle-lithosphere interactions that can add to the discoveries from mechanical models. These mechanical models have shown a new way to track lithospheric gaps at depth by observing variations in surface topography near slab holes. This is another observable which can help future researchers find and/or confirm the presence of slab gaps in subduction zones.

APPENDICES

APPENDIX 1. PLOTTING SCRIPTS

Includes all scripts used after the model run for plotting and data analysis (MATLAB scripts).

Calculation of the least squares solutions and their associated plots in the two-dimensional models – maxTopoVSarea.m

Plots of the two-dimensional topography profiles used – topoPlots_2D_NEW.m

Plots of the three-dimensional topography profiles, map view contour plots, surface plots, and other three-dimensional plots from data analyses performed – topoPlots_3D.m

Plots of the vertical velocity profiles of two-dimensional models – velPlots_2D.m

Scripts located in Google Drive at the following link:

https://drive.google.com/drive/folders/1zkGqRgz3XE69mezQSnBswCk9D50Qt2eo?usp=sharing

APPENDIX 2. MODEL SCRIPTS

Includes some example scripts from various two-dimensional and three-dimensional models (Jupyter notebooks / Python scripts).

TWDS0171.py – Model script for two-dimensional reference case, version 171

TWDS0208.py – Model script for two-dimensional top tear case, version 208

TWDS0190.py – Model script for two-dimensional flat slab reference case, version 190

TWDS0194.py – Model script for two-dimensional flat slab slab gap case, version 194

THDS0047.py – Model script for three-dimensional reference case, version 47

THDS0037.py – Model script for three-dimensional large slab hole case, version 37

THDS0056.py – Model script for three-dimensional circular slab hole case, version 56

THDS0060.py – Model script for three-dimensional double hole case, version 60

Scripts located in Google Drive at the following link:

https://drive.google.com/drive/folders/1zkGqRgz3XE69mezQSnBswCk9D50Qt2eo?usp=sharing

REFERENCES

Amaru, M., 2007, Global travel time tomography with 3-D reference models, Utrecht University.

Anderson, M., Alvarado, P., Zandt, G., and Beck, S., 2007, Geometry and brittle deformation of the subducting Nazca Plate, Central Chile and Argentina: Geophysical Journal International, v. 171, no. 1, p. 419-434.

Antonijevic, S. K., Wagner, L. S., Kumar, A., Beck, S. L., Long, M. D., Zandt, G., Tavera, H., and Condori, C., 2015, The role of ridges in the formation and longevity of flat slabs: Nature, v. 524, no. 7564, p. 212-215.

Barazangi, M., and Isacks, B. L., 1976, Spatial distribution of earthquakes and subduction of the Nazca plate beneath South America: Geology, v. 4, no. 11, p. 686-692.

Berk Biryol, C., Beck, S. L., Zandt, G., and Özacar, A. A., 2011, Segmented African lithosphere beneath the Anatolian region inferred from teleseismic P-wave tomography: Geophysical Journal International, v. 184, no. 3, p. 1037-1057.

Billen, M. I., 2008, Modeling the dynamics of subducting slabs: Annu. Rev. Earth Planet. Sci., v. 36, p. 325-356.

Chen, Z., Schellart, W. P., Strak, V., and Duarte, J. C., 2016, Does subduction-induced mantle flow drive backarc extension?: Earth and Planetary Science Letters, v. 441, p. 200-210.

Christensen, N. I., and Mooney, W. D., 1995, Seismic velocity structure and composition of the continental crust: A global view, v. 100, no. B6, p. 9761-9788.

Conrad, C. P., and Lithgow-Bertelloni, C., 2002, How Mantle Slabs Drive Plate Tectonics: Science, v. 298, no. 5591, p. 207.

Crameri, F., Schmeling, H., Golabek, G. J., Duretz, T., Orendt, R., Buiter, S. J. H., May, D. A., Kaus, B. J. P., Gerya, T. V., and Tackley, P. J., 2012, A comparison of numerical surface topography calculations in geodynamic modelling: an evaluation of the 'sticky air' method: Geophysical Journal International, v. 189, no. 1, p. 38-54.

Delph, J. R., Biryol, C. B., Beck, S. L., Zandt, G., and Ward, K. M., 2015, Shear wave velocity structure of the Anatolian Plate: anomalously slow crust in southwestern Turkey: Geophysical Journal International, v. 202, no. 1, p. 261-276.

Duretz, T., Gerya, T. V., and May, D. A., 2011, Numerical modelling of spontaneous slab breakoff and subsequent topographic response: Tectonophysics, v. 502, no. 1, p. 244-256.

English, J. M., Johnston, S. T., and Wang, K., 2003, Thermal modelling of the Laramide orogeny: testing the flat-slab subduction hypothesis: Earth and Planetary Science Letters, v. 214, no. 3-4, p. 619-632.

Faccenna, C., Becker, T. W., Auer, L., Billi, A., Boschi, L., Brun, J. P., Capitanio, F. A., Funiciello, F., Horvàth, F., Jolivet, L., Piromallo, C., Royden, L., Rossetti, F., and Serpelloni, E., 2014a, Mantle dynamics in the Mediterranean: Reviews of Geophysics, v. 52, no. 3, p. 283-332.

Faccenna, C., Becker, T. W., Miller, M. S., Serpelloni, E., and Willett, S. D., 2014b, Isostasy, dynamic topography, and the elevation of the Apennines of Italy: Earth and Planetary Science Letters, v. 407, p. 163-174.

Ferrari, L., 2004, Slab detachment control on mafic volcanic pulse and mantle heterogeneity in central Mexico: Geology, v. 32, no. 1, p. 77-80.

Gutscher, M.-A., Maury, R., Eissen, J.-P., and Bourdon, E., 2000, Can slab melting be caused by flat subduction?: Geology, v. 28, no. 6, p. 535-538.

Gvirtzman, Z., and Nur, A., 2001, Residual topography, lithospheric structure and sunken slabs in the central Mediterranean: Earth and Planetary Science Letters, v. 187, no. 1, p. 117-130.

Hall, R., 2012, Late Jurassic–Cenozoic reconstructions of the Indonesian region and the Indian Ocean: Tectonophysics, v. 570-571, p. 1-41.

Hall, R., and Spakman, W., 2015, Mantle structure and tectonic history of SE Asia: Tectonophysics, v. 658, p. 14-45.

Handy, M. R., Ustaszewski, K., and Kissling, E., 2015, Reconstructing the Alps–Carpathians–Dinarides as a key to understanding switches in subduction polarity, slab gaps and surface motion: International Journal of Earth Sciences, v. 104, no. 1, p. 1-26.

Hu, J., and Liu, L., 2016, Abnormal seismological and magmatic processes controlled by the tearing South American flat slabs: Earth and Planetary Science Letters, v. 450, p. 40-51.

Keskin, M., 2003, Magma generation by slab steepening and breakoff beneath a subduction-accretion complex: An alternative model for collision-related volcanism in Eastern Anatolia, Turkey: Geophysical Research Letters, v. 30, no. 24.

Király, Á., Portner, D. E., Haynie, K. L., Chilson-Parks, B. H., Ghosh, T., Jadamec, M., Makushkina, A., Manga, M., Moresi, L., and O'Farrell, K. A., 2020, The effect of slab gaps on subduction dynamics and mantle upwelling: Tectonophysics, v. 785, p. 228458.

Levin, V., Shapiro, N., Park, J., and Ritzwoller, M., 2002, Seismic evidence for catastrophic slab loss beneath Kamchatka: Nature, v. 418, no. 6899, p. 763-767.

Lynner, C., Anderson, M. L., Portner, D. E., Beck, S. L., and Gilbert, H., 2017, Mantle flow through a tear in the Nazca slab inferred from shear wave splitting: Geophysical Research Letters, v. 44, no. 13, p. 6735-6742.

Manea, V. C., Pérez-Gussinyé, M., and Manea, M., 2012, Chilean flat slab subduction controlled by overriding plate thickness and trench rollback: Geology, v. 40, no. 1, p. 35-38.

Menke, W., and Menke, J., 2016, Environmental data analysis with MatLab, Academic Press.

Millen, D. W., and Hamburger, M. W., 1998, Seismological evidence for tearing of the Pacific plate at the northern termination of the Tonga subduction zone: Geology, v. 26, no. 7, p. 659-662.

Moresi, L., Betts, P. G., Miller, M. S., and Cayley, R. A., 2014, Dynamics of continental accretion: Nature, v. 508, no. 7495, p. 245-248.

Moresi, L., Dufour, F., and Mühlhaus, H. B., 2003, A Lagrangian integration point finite element method for large deformation modeling of viscoelastic geomaterials: Journal of Computational Physics, v. 184, no. 2, p. 476-497.

Nolet, G., 2009, Slabs Do Not Go Gently: Science, v. 324, no. 5931, p. 1152-1153.

Pearce, J. A., Bender, J., De Long, S., Kidd, W., Low, P., Güner, Y., Saroglu, F., Yilmaz, Y., Moorbath, S., and Mitchell, J., 1990, Genesis of collision volcanism in Eastern Anatolia, Turkey: Journal of Volcanology and Geothermal Research, v. 44, no. 1-2, p. 189-229.

Piromallo, C., and Morelli, A., 2003, P wave tomography of the mantle under the Alpine-Mediterranean area: Journal of Geophysical Research: Solid Earth, v. 108, no. B2.

Plomerová, J., Kouba, D., and Babuška, V., 2002, Mapping the lithosphere–asthenosphere boundary through changes in surface-wave anisotropy: Tectonophysics, v. 358, no. 1, p. 175-185.

Portner, D. E., Beck, S., Zandt, G., and Scire, A., 2017, The nature of subslab slow velocity anomalies beneath South America: Geophysical Research Letters, v. 44, no. 10, p. 4747-4755.

Portner, D. E., Delph, J. R., Biryol, C. B., Beck, S. L., Zandt, G., Özacar, A. A., Sandvol, E., and Türkelli, N., 2018, Subduction termination through progressive slab deformation across Eastern Mediterranean subduction zones from updated P-wave tomography beneath Anatolia: Geosphere, v. 14, no. 3, p. 907-925.

Ramos, V. A., and Folguera, A., 2009, Andean flat-slab subduction through time: Geological Society, London, Special Publications, v. 327, no. 1, p. 31-54.

Rudolph, M. L., Lekić, V., and Lithgow-Bertelloni, C., 2015, Viscosity jump in Earth's mid-mantle: Science, v. 350, no. 6266, p. 1349.

Schellart, W., and Moresi, L., 2013, A new driving mechanism for backarc extension and backarc shortening through slab sinking induced toroidal and poloidal mantle flow: Results from dynamic subduction models with an overriding plate: MANTLE FLOW DRIVES BACKARC DEFORMATION: Journal of Geophysical Research: Solid Earth, v. 118, p. 3221-3248.

Şengör, A. C., and Yilmaz, Y., 1981, Tethyan evolution of Turkey: a plate tectonic approach: Tectonophysics, v. 75, no. 3-4, p. 181-241.

Smyth, H. R., Hall, R., and Nichols, G. J., 2008, Cenozoic volcanic arc history of East Java, Indonesia: The stratigraphic record of eruptions on an active continental margin: Special Papers-Geological Society of America, v. 436, p. 199.

Stern, R. J., 2002, SUBDUCTION ZONES, v. 40, no. 4, p. 3-1-3-38.

Tagawa, M., Nakakuki, T., and Tajima, F., 2007, Dynamical modeling of trench retreat driven by the slab interaction with the mantle transition zone: Earth, Planets and Space, v. 59, no. 2, p. 65-74.

Thorkelson, D. J., 1996, Subduction of diverging plates and the principles of slab window formation: Tectonophysics, v. 255, no. 1, p. 47-63.

Trampert, J., 1998, Global seismic tomography: the inverse problem and beyond: Inverse Problems, v. 14, no. 3, p. 371.

Widiyantoro, S., Pesicek, J. D., and Thurber, C. H., 2011, Subducting slab structure below the eastern Sunda arc inferred from non-linear seismic tomographic imaging: Geological Society, London, Special Publications, v. 355, no. 1, p. 139.

Wilson, J. T., 1965, A new class of faults and their bearing on continental drift: Nature, v. 207, no. 4995, p. 343-347.

Wortel, M. J. R., and Spakman, W., 2000, Subduction and Slab Detachment in the Mediterranean-Carpathian Region: Science, v. 290, no. 5498, p. 1910-1917.

Zor, E., Sandvol, E., Gürbüz, C., Türkelli, N., Seber, D., and Barazangi, M., 2003, The crustal structure of the East Anatolian plateau (Turkey) from receiver functions: Geophysical Research Letters, v. 30, no. 24.

VITA

My educational background begins in my hometown of Marion, North Carolina at McDowell Technical Community College, where I began by acquiring two years of college credits and an Associate of Science degree that provided me the opportunity to transfer to Appalachian State University in Boone, North Carolina. I spent the next three years at Appalachian State University and acquired my Bachelor of Science degree in Geology with a concentration in Quantitative Geoscience. This concentration provided me with a minor in Mathematics. Additionally, at Appalachian State, I held the position of Undergraduate Research Assistant, where I aided my undergraduate advisor in a research project involving near surface geophysics for my last year. During my final year at Appalachian State, I received an award for honorary students attending field camp for completion of a geology degree. At the University of Kentucky, I held the position of Graduate Teaching Assistant for nearly two years.

Taylor Murphy Arrowood